Numerical Analysis of Transport in Dynamical Systems

Von der Fakultät für Elektrotechnik,
Informatik und Mathematik
der Universität Paderborn
zur Erlangung des akademischen Grades
Doktor der Naturwissenschaften

– Dr. rer. nat. –

genehmigte Dissertation

von

Kathrin Padberg

Paderborn, 2005

Gutachter: Prof. Dr. Michael Dellnitz
Prof. Dr. Jerrold E. Marsden
Prof. Dr. Björn Schmalfuß

Tag der mündlichen Prüfung: 1.6.2005

I may not have gone where I intended to go,
but I think I have ended up where I needed to be.
Douglas Adams (1952-2001)

Acknowledgements

I must begin by thanking my advisor Prof. Dr. Michael Dellnitz for his guidance, support, and motivation, but, in particular, for the great freedom he has allowed me. His working group has always provided a very pleasant research environment to me.

I would like to thank Professor Jerrold E. Marsden from the *California Institute of Technology* for introducing me to interesting applications and ideas. Mutual visits and discussions contributed to the progress in my research as well.

I also want to thank Prof. Dr. Björn Schmalfuß for helpful comments and for serving as a reviewer for this thesis.

Moreover, I am indebted to Dr. Oliver Junge, Dr. Robert Preis, and especially to Bianca Thiere for many interesting and enlightening discussions, exciting joint work, and their constant support.

Thanks also to Professor George Haller, Mirko Hessel-von Molo, Dr. Wang Sang Koon, Dr. Francois Lekien, Dr. Martin Lo, Sina Ober-Blöbaum, Dr. Shane Ross, Prof. Dr. Christof Schütte, and Shawn Shadden for fruitful discussions, comments, and support of all kinds. Furthermore, I would like to thank Dr. Pat Haley and Dr. Pierre Lermusiaux for providing the three-dimensional HOPS data.

A special thank you goes to Katalin Grubits for her careful proof-reading of the manuscript and for many helpful comments.

I gratefully acknowledge support under two different grants: the BMBF-project *math-kit* as well as the DFG-sponsored research project *SFB 376* on *Massively Parallel Computation*.

I thank my colleagues in Paderborn for discussions on scientific and non-scientific topics and for technical and administrative support, including Alessandro Dell'Aere, Helene Derksen-Riesen, Birgit Duddeck, Marianne Kalle, Arvind Krishnamurthy, Anne Möhle, Dr. Gudrun Oevel, Marcus Post, *Rechnerbetreuung Mathematik*, Uwe Schubert, Dr. Oliver Schütze, Stefan Sertl, Fang Wang, and Katrin Witting.

However, this list would not be complete without a special thanks to all my friends and my family. In particular, the constant support and encouragement of my parents, Heinz-Josef and Helene Padberg, has accompanied me over many years of studies.

Finally, I thank Dietmar Gehle - for a number of things.

Contents

1 Introduction **1**

2 Basic Concepts and Definitions **11**
2.1 Autonomous Dynamical Systems 12
2.1.1 Hyperbolic Sets and Invariant Manifolds 13
2.1.2 Attractor 14
2.1.3 Ergodic Theory 16
2.1.4 Lyapunov Exponents 16
2.2 Non-Autonomous Dynamical Systems 20
2.2.1 Hyperbolic Trajectories and Invariant Manifolds 20
2.2.2 Pullback Attractor 25
2.2.3 Lyapunov Exponents 26
2.3 Finite-Time Velocity Fields 27

3 The Set Oriented Approach **30**
3.1 The Subdivision Algorithm 30
3.2 The Continuation Algorithm 32
3.3 Extensions to Non-Autonomous Systems 34

4 Expansion Rate Approach for Autonomous Systems **37**
4.1 Introduction 37
4.2 Theoretical Results 39
4.2.1 Expansion Rates 39
4.2.2 Expansion Rates and Stable Manifolds 39
4.2.3 Direct Expansion Rates 43
4.2.4 Error Estimates 44
4.3 Approximation of Expansion Rates 47
4.3.1 Set Wise Expansion Rates 47
4.3.2 Test Point Strategies 47
4.3.3 Choice of Number of Iterations N 50
4.3.4 Parallel Computing 53

4.3.5 Examples 54
4.4 Extraction of Invariant Manifolds 60
4.4.1 The Subdivision Algorithm 60
4.4.2 Examples 62
4.5 Expansion in Graphs 68
4.5.1 Dynamical Systems and Graphs 68
4.5.2 Graph Based Expansion 69
4.5.3 Examples 70
4.5.4 Discussion 73

5 Analyzing Transport in Non-Autonomous Systems 76
5.1 Introduction 76
5.2 Time-Dependent Invariant Manifolds 77
5.2.1 Theoretical Results 79
5.2.2 Numerical Methods 83
5.2.3 The Continuation Algorithm 83
5.2.4 Examples 85
5.3 Computation of Transport Rates 92
5.3.1 A Transfer Operator Approach 93
5.3.2 Examples 100

6 Application to Ocean Flows 108
6.1 Introduction 108
6.2 Two-Dimensional Ocean Flows 110
6.3 Transport in Monterey Bay 115
6.4 Three-Dimensional Ocean Flows 116

7 Conclusion 120

Chapter 1

Introduction

In this thesis numerical techniques for the analysis of transport phenomena in non-autonomous dynamical systems are developed. This introduction will establish the context: it addresses the dynamical systems approach to transport and discusses how these concepts can be used for the analysis of time-dependent velocity fields. This provides the scientific background for a detailed description of the results in this thesis.

Transport and dynamical systems Transport processes play an important role in many natural phenomena. Prominent examples are the chaotic advection of fluid particles in geophysical flows or the transport of asteroids and comets in the solar system. Similar transport mechanisms are also at work in chemical physics explaining for example the transition between different conformations of molecules or the kinematics of chemical reactions.

Suppose one is interested in the motion of a passive particle, that is a passive quantity driven by a fluid flow. Then, neglecting molecular diffusion [11, 74], the particle follows trajectories which are solutions of

$$\dot{x} = f(x,t),$$

where $f(x,t)$ is the velocity field, $x \in \mathbb{R}^n$ the particle position, and $t \in \mathbb{R}$ the time. From a dynamical systems point of view the motion of the passive quantity is governed by those structures that form the skeleton of the dynamics, such as attractors, invariant manifolds, or, in the case of Hamiltonian systems, KAM tori. Over the past twenty years this analogy between the global, geometrical study of nonlinear dynamical systems and transport and mixing studies in classical and fluid mechanics has been used to obtain a deeper understanding of transport issues in a variety of systems, notably in geophysical models, see for example Aref [3], Jones [60], or Wiggins [112] for recent reviews.

Hence, most of the work has been done in the context of two-dimensional, time-periodic or quasi-periodic velocity fields where the study of the equations for fluid particle trajectories can be reduced to the study of a two-dimensional area-preserving Poincaré map. Once the problem has been cast in this setting, a variety of well-known techniques and ideas from dynamical systems theory can be applied for the purpose of studying fluid transport and mixing issues. For example, KAM tori represent barriers to fluid transport and mixing whereas chaotic dynamics should act to enhance mixing. In particular, invariant manifolds, such as the stable and unstable manifolds of hyperbolic periodic points, manifest themselves as organizing structures in the fluid flow [86]. In that setting, the stable and unstable manifolds generically intersect transversally, producing an infinite number of homoclinic or heteroclinic tangles, so-called lobes - little areas formed by the manifold intersections (see e.g. [76, 91, 110]). These lobes provide a natural gate way between dynamically distinct regions; hence, lobe dynamics is seen as the main transport mechanism in this context. Transport can be quantified in terms of lobe volumes, which can be estimated for example by a Melnikov approach [78, 110]. This transport mechanism based on the geometrical template of stable and unstable manifolds is known as *chaotic transport*.

Time-dependent dynamical systems Recent progress in nonlinear dynamics has extended the above picture to velocity fields with general aperiodic time dependence. Here hyperbolic trajectories and their stable and unstable manifolds continue to manifest themselves as the organizing structures in the flows. However, often the structures under consideration exist only on a finite-time interval. This is the case in turbulent flows or, in particular, when the velocity field $f(x,t)$ is given as data obtained from measurements or as the numerical solution of a partial differential equation such as the Navier-Stokes equation. For example, modern sensing techniques have been developed to the point where geophysical data such as velocity fields or temperature fields can now be obtained at a fairly high resolution in space and time. In particular, the Office for Naval Research sponsored Autonomous Ocean Sampling Network II project (AOSN II) [2] as well as its successor Adaptive Sampling and Prediction (ASAP) [4] have the objective to integrate sophisticated platforms and techniques to better observe and predict the ocean. Within the AOSN II field experiment in Monterey Bay (California) geophysical data has been obtained through different sensing devices such as autonomous underwater vehicles or high frequency radar arrays. One scientific goal is to analyze the velocity data in order to detect so-called Lagrangian coherent structures [102]. Without being precise about their definition for now these can be seen as finite-time analogues to stable and unstable manifolds, still mediating transport in the fluid flow, see Figure 1.1. These structures are of

great oceanographic interest. For example, numerical evidence shows that they often correspond to temperature fronts [74]. Moreover, the knowledge of these structures is useful when optimizing the trajectories or distribution of underwater gliders [57, 105].

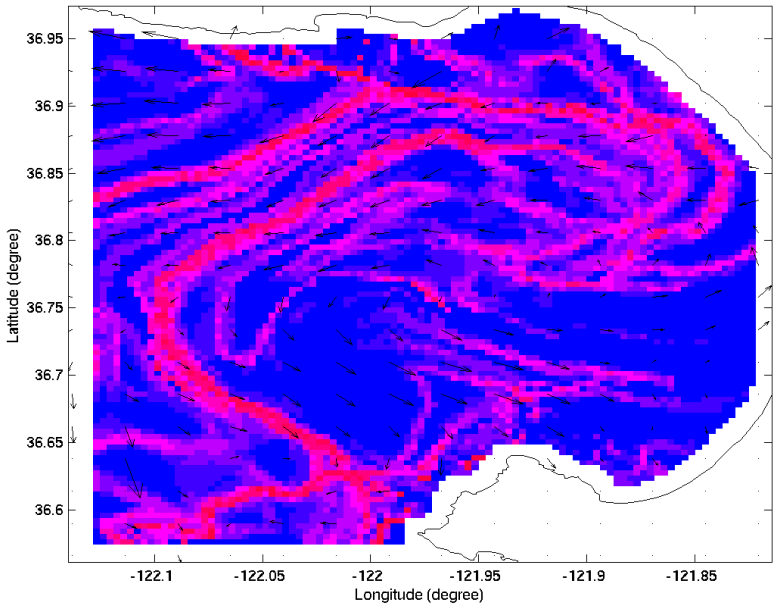

Figure 1.1: Illustration of the discrete velocity field measured in Monterey Bay in summer 2003 within the AOSN II project [2]. Also shown is an approximation of Lagrangian coherent structures (red), which mediate transport and mixing (see Chapter 6).

However, in this context several mathematical and practical problems arise: first of all, most of the fundamental concepts and results from dynamical systems theory have at best questionable validity when the evolution describing the dynamics is based on a time series. For instance, chaos, hyperbolicity and invariant manifolds are asymptotic notions and the general time dependence of the data rules out an extrapolation of the dynamical system to infinity. So, finite-time concepts for the classical notions need to be established.

The development of mathematically consistent concepts for dynamical systems with aperiodic time dependence has been an active research area in the last ten years (see e.g. [112]). This leads to the new idea of a finite-time analysis. Rather than dealing with asymptotic notions of the evolution of the system, one considers the structures of interest on finite-time intervals and makes statements

about notions, such as their stability, only with respect to this time span. This is a natural thing to do as in the numerical analysis of dynamical systems one is always restricted to dealing with finite-time approximations.

Note that in the course of this work the classical terms from dynamical systems will also be used to describe finite-time notions. This may not always be in accordance with classical dynamical systems theory but is widely used in the literature, see Wiggins [112] for a discussion. For example, the term *finite-time hyperbolic trajectory* is completely at odds with classical dynamical systems theory where a trajectory is defined for all times and hyperbolicity is an asymptotic concept. In the finite-time context this term refers to a solution to the differential equation with respect to the time interval under consideration which attracts other solutions from some directions and repels them along others. A precise definition is given in Section 2.3.

Recent work has shown that the presence of a uniformly hyperbolic trajectory defined on a long enough finite-time interval implies the existence of (finite-time) stable and unstable manifolds, so-called hyperbolic material lines or surfaces, which play again a crucial role in transport and mixing as in the classical case [50, 45]. The existence of a uniformly hyperbolic trajectory, however, can only be proven under very restrictive conditions. It is essential to have a hyperbolic stagnation point on frozen time slices of the velocity field which does not move too fast under the dynamics [49]. However, these conditions are difficult to verify in general fluid flows [61, 113].

Approximation of hyperbolic trajectories and their stable/unstable manifolds Only a few algorithms for the detection of (finite-time) hyperbolic trajectories (e.g. [56, 63]) have been proposed. The majority of recent approaches deal with the approximation of (finite-time) stable and unstable manifolds, where the underlying hyperbolic trajectory can be obtained as the intersection of the manifolds. These techniques fall roughly into two classes. The first class of methods uses the fact that a ball of points initialized near the hyperbolic trajectory will align along the unstable manifold or along the stable manifold under time reversal [78, 79, 80, 84], see Figure 1.2. A similar notion is that of pullback attraction [7, 8, 97, 104], where attracting sets in fibers of the extended phase are considered. Under mild assumptions it can be shown that the local unstable manifold of a hyperbolic trajectory is pullback attracting [104].

The second class of approaches makes use of the repelling nature of the stable manifold in a statistical sense. Here the stable manifold of a hyperbolic trajectory typically appears as a local maximizer of the finite-time Lyapunov exponent or direct Lyapunov exponent [46, 47, 74]. Finite-time Lyapunov exponents with

respect to initial conditions $x(t_0) = x_0$ are defined by

$$\Lambda(t; t_0, x_0) := \frac{1}{2t} \log \lambda_{\max}\{(D_x\varphi^{t+t_0,t_0}(x_0))^\top D_x\varphi^{t+t_0,t_0}(x_0)\},$$

where $\lambda_{\max}$ denotes the maximum eigenvalue of the positive semi-definite matrix $(D_x\varphi^{t+t_0,t_0}(x_0))^\top D_x\varphi^{t+t_0,t_0}(x_0)$. This quantity measures how much an infinitesimal perturbation grows under the linearized flow and is expected to be large along repelling objects.

Related concepts are finite-size Lyapunov exponents [9, 10, 62, 70] or relative dispersion [12, 61, 108, 113], which measure how much solutions to neighboring initial conditions of a small but finite distance diverge as time increases. These approaches do not use the Jacobian matrix $D_x\varphi^{t+t_0,t_0}(x_0)$. The hyperbolicity times approach by Haller [45, 46], which takes necessary and sufficient conditions into account, uses the eigenvalue structure of the Jacobian to detect the local stable and unstable manifolds of a (finite-time) hyperbolic trajectory.

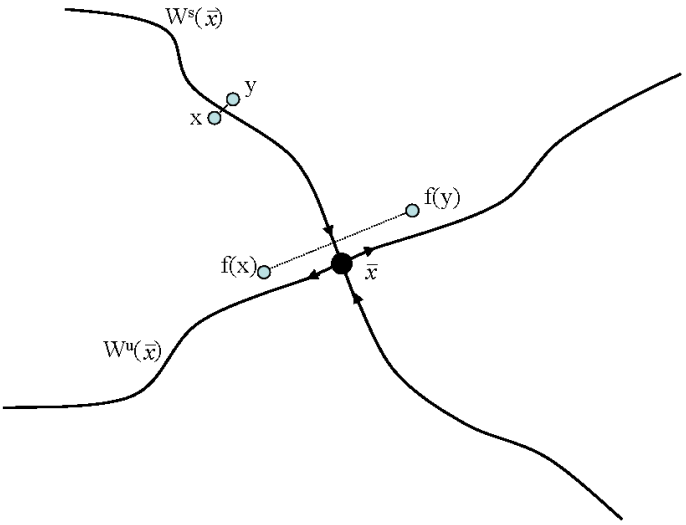

Figure 1.2: Stable and unstable manifold of a hyperbolic saddle point in a time-discrete dynamical system. Points initialized on either sides of the stable manifold move along different branches of the unstable manifold under the dynamics.

The above methods have a number of shortcomings. Most of these techniques are formulated for the two-dimensional setting. Also, in order to be able to approximate the fine scale structures, such as invariant manifolds or even lobes, from which to deduce the transport quantities, a dense enough grid representation of the data is required, which is often not available. Furthermore, especially in

methods that make use of the finite-time Lyapunov exponent or hyperbolicity times, a reliable approximation of the total derivative $D_x f(x,t)$ is needed.

Without using the Jacobian, the stable manifolds can be approximated by those initial conditions that determine solutions which remain in a certain initial box for the longest time [98, 106]. These methods are independent of the dimension of phase space or the accuracy of the underlying data but they appear to be experimental with theoretical results largely missing.

A common feature of the majority of these approaches is that they seek to provide an accurate approximation of the invariant manifolds in order to be able to discover the underlying transport mechanism. However, while invariant manifolds in periodic or quasi-periodic velocity fields generically intersect infinitely often, this is not true for aperiodic flows and finite-time systems [78, 87]. Here, there are usually only a finite number of lobes or none at all, ruling out the application of lobe dynamics. Furthermore, in the fluid dynamics context, often some version of Melnikov's method is used for transport calculations. This requires the flow to be very close to an integrable steady limit, a condition which is usually not fulfilled in arbitrary flows [49]. Finally, lobe dynamics may not even be able to provide a template for all transport mechanisms at work [62]. This is reason enough to develop manifold independent methods for the calculation of transport rates.

Other techniques for analyzing transport Apart from attempting to extract invariant manifolds as the *boundaries* between regions, one can also think of directly approximating the regions of interest, such as in the patchiness approach [77, 82, 83]. In this context dynamically distinct regions are identified using time averages, yielding an ergodic partition of the set under consideration.

Another concept is that of almost invariant sets, see e.g. [26, 28, 30, 31, 32, 38]. These are regions in phase space that are almost invariant in the sense that, with high probability, a trajectory starting in a particular set will stay in this set for a long time.

To identify and approximate almost invariant sets, one considers a transfer operator (the Frobenius-Perron operator) on the set of probability measures whose fixed points are invariant measures. The set oriented approach first proposed by Dellnitz and Hohmann [23, 24] provides a natural basis for the numerical approximation of this operator. Here the phase space is discretized by small sets (boxes). Then the transfer operator with respect to this discretization can be approximated in terms of a transition matrix which contains the transition probabilities between these boxes [64], an idea which goes back to Ulam [107]. By this one obtains a Markov chain. The eigenvector of the transition matrix corresponding to the eigenvalue 1 is an approximation of the natural invariant measure, whereas

eigenvectors corresponding to eigenvalues of modulus near 1 approximate signed measures. Then boxes corresponding to negative entries in the eigenvector and boxes corresponding to positive entries form two almost invariant sets [26, 32].

Apart from such a spectral approach one can view the Markov process as a directed graph. Then standard graph algorithmic techniques can be employed to obtain a partition of phase space into almost invariant sets [28, 30, 31, 38]. Once a partition of phase space has been obtained, transport rates between the regions obtained can be easily computed using the transfer operator [28]. Moreover, in Dellnitz, Junge, Koon et al. [28] it was demonstrated in an example that the boundaries between almost invariant sets correspond to invariant manifolds of hyperbolic periodic points.

However, this methodology is restricted to autonomous systems and furthermore, because of its global nature, provides a coarse picture of the phase space structure. Although some recent effort has been made by Froyland [37], typically the boundaries between the almost invariant sets are not resolved at a sufficiently high accuracy to analyze transport at smaller scales.

What is achieved in this thesis This thesis contributes to the current research on the detection of invariant manifolds in dynamical systems with general time dependencies and the approximation of transport rates by making use of the advantages of different techniques. To be more precise, we extend the well-established methods related to finite-time Lyapunov exponents and relative dispersion described above, and embed them in the set oriented approach first proposed by Dellnitz and Hohmann [23, 24]. This new multilevel technique, the *expansion rate approach*, allows for the efficient detection, approximation, and continuation of stable and unstable manifolds to hyperbolic objects. It is largely independent of the resolution of the data and its formulation is independent of the dimension of phase space.

Moreover, we present a set oriented technique for the computation of transport rates in dynamical systems with general time dependencies which is independent of invariant manifolds. The method relies on a discretization of the Perron-Frobenius operator of the underlying non-autonomous dynamical system and extends and improves the results in Dellnitz, Junge, Koon et al. [28], where the autonomous case has been treated. Hence, this approach can also be applied to dynamical systems where the invariant manifold cannot be obtained accurately enough to consider lobe dynamics or where the underlying transport mechanism remains obscure.

Altogether this thesis makes four major contributions to the current research in the numerical analysis of chaotic transport:

1. Detection and extraction of invariant manifolds in autonomous dynamical

systems,

2. Extraction and continuation of invariant manifolds in non-autonomous dynamical systems,

3. Manifold independent approach for the computation of transport rates between regions of interest in non-autonomous dynamical systems, and

4. Application of these methods to geophysical fluid data obtained from high frequency radar measurements in Monterey Bay in summer 2003.

The outline of this thesis is as follows:

In **Chapter 2** we briefly introduce the relevant concepts from classical dynamical systems theory: hyperbolicity, invariant manifolds and attractors as well as Lyapunov exponents for a diffeomorphism. We also address how these notions translate into the setting of non-autonomous ordinary differential equations and the analysis of velocity fields only given for finite time.

In **Chapter 3** we review the basic set oriented methods for the approximation of relative global attractors and invariant manifolds of autonomous dynamical systems as introduced in Dellnitz and Hohmann [23, 24]. The extensions of these results to non-autonomous systems by Aulbach, Rasmussen, and Siegmund [7], and Siegmund [104] are briefly summarized.

Chapter 4 contains all the theoretical and numerical results related to the detection and extraction of invariant manifolds in autonomous dynamical systems, as well as a brief section discussing heuristics for detecting relevant structures in graphs.

We define the *expansion rate* as the dominant finite-time Lyapunov exponent with respect to some initial condition and analyze the relation between expansion rates and geometrical structures in the underlying dynamical system. We note that in typical cases the stable manifold of hyperbolic periodic points can be identified as being a local maximizer of the expansion rate. For special cases this relation is not only necessary but also sufficient. The *direct expansion rate* is then defined as a finite approximation of the expansion rate via a difference quotient. This formulation does not require smoothness of the map.

The numerical approximation of expansion rates and direct expansion rates in a set oriented context is then introduced and relevant test point strategies are discussed. We also address the problem of choosing an appropriate number of iterates of the map to uncover the desired structures.

The set oriented methods provide a natural basis for a subdivision scheme for the extraction of candidates for stable manifolds of hyperbolic periodic points, that is regions that are characterized by large expansion rates. We prove convergence of this algorithm and demonstrate it by the example of a steady ABC-flow [36, 46]. This three-dimensional differential equation is notable for being an

exact solution of Euler's equation, exhibiting a nontrivial streamline geometry. We extract two-dimensional stable manifolds of hyperbolic periodic orbits. To the best of our knowledge this has been the first time that these two-dimensional structures have been fully extracted and visualized.

In Dellnitz, Junge, Koon et al. [28] it has been shown that standard graph partitioning methods can be used to detect almost invariant sets. In the example considered, the boundaries between these sets coincide with the stable and unstable manifold of a hyperbolic fixed point of the underlying dynamical system. This relation is not surprising as invariant manifolds are known to bound dynamically distinct regions. Therefore, we derive heuristics based on the expansion idea in order to detect these relevant manifold structures already in the graphs and we test our approach with two examples. We note that such methods may provide a first step in the analysis of time series.

In the first part of **Chapter 5** set oriented methods for the numerical analysis of non-autonomous systems are developed. We show how the results from the autonomous case can be adapted to systems with general time dependence. The numerical methods developed before are immediately applicable if one computes the scalar expansion rate field with respect to a fixed initial time. However, as the expansion and direct expansion rates here are not only dependent on the integration interval but also on the initial time, one typically needs to carry out these computations for a large number of initial times to analyze the temporal behavior of the stable manifolds of hyperbolic trajectories. To avoid this we propose a set oriented continuation scheme, which makes use of the fact that fibers of the stable manifold of a uniformly hyperbolic trajectory can be continued in backward time. The combination of a set oriented subdivision and continuation scheme based on the expansion rate technique provides a new approach for the efficient extraction of (finite-time) invariant manifold candidates.

The second part of the chapter addresses the approximation of transport rates. Velocity fields defined as data sets typically do not provide an accurate enough template for the computation of transport rates in terms of lobe dynamics. Therefore we derive a set oriented approach for the approximation of transport rates which is independent of any specific transport mechanism. The method relies on a discretization of the Perron-Frobenius operator of the underlying non-autonomous dynamical system and extends and improves the results in [28], where the set-up for the autonomous case has been introduced. Notably, our method does not require volume-preservation of the underlying dynamical system. Moreover, unlike in Monte Carlo approaches, such as used in [39], we can derive an error estimate yielding an upper and lower bound on the transport rate between arbitrary sets of interest. In addition, an adaptive approach is described which has been designed to reduce the discretization error, generalizing the approach presented in [28]. We test our method by two examples, a Rossby Wave Flow as well as an autonomous

problem from chemical physics, where ionization rates for the Rydberg atom in crossed fields are computed.

In **Chapter 6** we discuss applications of our methods to geophysical fluid flows. To be more precise, we apply our techniques to time-dependent two-dimensional data sets, obtained within the AOSN II project from high frequency radar measurements in Monterey Bay in summer 2003 [2]. We identify Lagrangian coherent structures [102] that mediate transport in ocean dynamics. For the integration and interpolation of the two-dimensional time-dependent data we use MANGEN [74], which also takes the different boundary conditions into account. However, as the accurate trajectory integration is computationally very expensive we are restricted in the number of test points. We therefore propose a different direct expansion rate approach that only considers the box centers. This alternative method is very efficient but nevertheless gives a good indication of the location of areas of high stretching.

Additionally, we compute transport rates from near-shore regions to regions in the open sea west of Monterey Bay. The results demonstrate the strong time-dependence of the transport processes, having serious implications for such things as pollution timing as discussed in [74, 75]. We note that, due to the open boundary allowing particles to leave the area under consideration, previous methods that take advantage of volume-preservation are difficult to apply.

Moreover, the first set of experiments indicate that our methods allow the consideration of three-dimensional oceanic flows. Also, three-dimensional geophysical data has been collected within the AOSN II project in Monterey Bay [2], with the goal being to learn more about genuinely three-dimensional events such as the upwelling event. Here cool, nutrient-rich depth water rises to the surface and influences the currents and temperature distribution in Monterey Bay dramatically. This event is of great interest to oceanographers. For example, future field experiments in Monterey Bay, such as planned within the ASAP project [4] for summer 2006, will even concentrate on the observation of the upwelling center. For our analysis we use data provided by the Harvard Ocean Prediction System (HOPS) [1, 54].

The thesis closes with a summary of the results and a discussion about open problems and possible future directions.

Chapter 2

Basic Concepts and Definitions

The classical theory of dynamical systems is devoted to the analysis of their qualitative and asymptotic behavior.

In the following section we briefly introduce the relevant concepts such as hyperbolicity, invariant manifolds and attractors, as well as Lyapunov exponents in the context of discrete autonomous systems. Notably, the analysis of continuous autonomous systems can be reduced to investigating an appropriate flow map. Therefore, only distinct characteristics for this class of systems are discussed.

In the second section we show how these notions translate into the context of non-autonomous dynamical systems. Here we define hyperbolic trajectories, show the existence of invariant manifolds, and briefly review the concept of pullback attractors as used, for example, in [7, 8, 15, 69, 97, 104]. Attractors for random dynamical systems are considered in [67, 68]. Motivated by applications in fluid dynamics and following the relevant literature, all concepts are introduced in the framework of ordinary differential equations, that is, non-autonomous time-continuous dynamical systems.

The theoretical concepts for dealing with finite-time notions are addressed in the third section. Sometimes, the velocity field is given as a set of data and thus only defined on a finite time interval. In this context, the classical notions of stable and unstable manifolds or Lyapunov exponents become problematic as they are asymptotic concepts. The development of a mathematically consistent theory for the finite-time setting has been an active research area for the last ten years. Here we give some relevant definitions and results by Haller and Poje [49], Sandstede et al. [96], as well as Ide et al. [56].

Before we proceed, we introduce the norms and distances that will be used throughout this thesis.

Norms, metrics and distances Let $X \subset \mathbb{R}^l$ be a compact set. We introduce the following norms and metrics on $\mathbb{R}^l$ or $\mathbb{R}^{l,l}$:

- $\|\cdot\|$ is used as a general notation for vector norms on $\mathbb{R}^l$ or matrix norms on $\mathbb{R}^{l,l}$;
- $\|x\|_\infty = \max\{|x_i|,\, i = 1, \ldots, l\}$ denotes the maximum-norm on $\mathbb{R}^l$;
- $|\!|\cdot|\!| := \|\cdot\|_2$ denotes the 2-norm, that is, the Euclidean vector norm

$$|\!|x|\!| = \sqrt{\sum_{i=1}^{l} x_i^2}, \qquad x \in \mathbb{R}^l$$

and the spectral norm for matrices $A \in \mathbb{R}^{l,l}$, respectively,

$$|\!|A|\!| = \max_{|\!|x|\!|=1} |\!|Ax|\!| = \max_{|\!|x|\!|=|\!|y|\!|=1} |y^\top A x| = \sqrt{\lambda_{\max}\{A^\top A\}},$$

where $\lambda_{\max}\{A^\top A\}$ refers to the largest eigenvalue of the symmetric positive-semidefinite matrix $A^\top A \in \mathbb{R}^{l,l}$.

Let $A, B \subset X \subset \mathbb{R}^l$ be two non-empty sets. The Euclidean vector norm on $\mathbb{R}^l$ defines a metric d on X

$$d(x, y) := |\!|x - y|\!|, \qquad x, y \in X.$$

We can then define three kinds of distances:

$$\begin{aligned} d(x, A) &:= \inf\{d(x, y) : y \in A\}, \\ d(A, B) &:= \sup\{d(x, B) : x \in A\} \text{ (Hausdorff semi-distance)}, \\ d_H(A, B) &:= \max\{d(A, B), d(B, A)\} \text{ (Hausdorff distance)}. \end{aligned}$$

2.1 Autonomous Dynamical Systems

Let $f : X \to X$ be a diffeomorphism defining a **discrete dynamical system**

$$x_{k+1} = f(x_k),\ k \in \mathbb{Z}.$$

on some compact subset $X \subset \mathbb{R}^l$. f may be given as an analytical map or as a time-T map $x_{n+1} = \phi^T(x_n)$ of the flow ϕ^t of an autonomous ordinary differential equation

$$\dot{x} = f(x)$$

with $x \in \mathbb{R}^l$ and $f : \mathbb{R}^l \to \mathbb{R}^l$ sufficiently smooth. We denote by $Df(x) := D_x f(x)$ the total derivative of f at x.

2.1.1 Hyperbolic Sets and Invariant Manifolds

A set $A \subset X$ is called **invariant** if $f(A) = A$. Simple examples of invariant sets are fixed points or periodic points. A fixed point $\bar{x}$ satisfies $f(\bar{x}) = \bar{x}$. For a periodic point x_p we have $f^p(x_p) = x_p$ for some finite $p > 1$ and $f^k(x_p) \neq x_p$ for $1 \leq k < p$. The dynamics of f in a neighborhood of a fixed point x is well studied in the case where x is **hyperbolic**, that is, $Df(x)$ does not possess an eigenvalue on the unit circle. Then the theorem of Hartman and Grobman (cf. [103]) says that f and Df are locally topologically conjugated. Moreover, the tangent space of X in x can be split into the direct sum of two $Df(x)$-invariant subspaces E^u and E^s, such that vectors in E^u are expanded by $Df(x)$ and vectors in E^s are contracted. E^u is called the unstable eigenspace, E^s the stable eigenspace.

The concept of hyperbolicity can be extended to general invariant sets:

Definition 2.1.1 (Hyperbolic invariant set) A closed invariant set $\Lambda \subset X$ is called **hyperbolic** if the tangent space T_xX for $x \in \Lambda$ can be written as the direct sum

$$T_xX = E^u_x \oplus E^s_x$$

such that

(i) $Df(x)(E^s_x) = E^s_{f(x)}$ and $Df(x)(E^u_x) = E^u_{f(x)}$;

(ii) there are constants $C > 0$ and $\lambda \in (0, 1)$ such that

$$\begin{aligned} \|Df^j(x)v\| &\leq C\lambda^j\|v\| \qquad \text{for } v \in E^s_x, j \geq 0, \\ \|Df^j(x)v\| &\leq C\lambda^{-j}\|v\| \qquad \text{for } v \in E^u_x, j \geq 0; \end{aligned}$$

(iii) E^s_x and E^u_x depend continuously on x.

Now we introduce the notion of stable and unstable manifolds for hyperbolic sets. Consider $A \subset X$ and let

$$\begin{aligned} W^s(A) &= \{y \in X |\, d(f^j(y), f^j(A)) \to 0 \text{ for } j \to \infty\} \\ W^u(A) &= \{y \in X |\, d(f^{-j}(y), f^{-j}(A)) \to 0 \text{ for } j \to \infty\} \end{aligned}$$

denote the **stable** and **unstable set** of A, respectively.

If Λ is a hyperbolic invariant set then $W^s(\Lambda)$ and $W^u(\Lambda)$ are immersed submanifolds of $\mathbb{R}^l$. The following statement gives an explanation:

Theorem 2.1.2 (Local stable and unstable manifold) *Let $\Lambda \subset X$ be a hyperbolic invariant set, $x \in \Lambda$ and $\varepsilon > 0$ sufficiently small. For*

$$\begin{aligned} W^s_\varepsilon(x) &= \{y \in X |\, d(f^j(y), f^j(x)) \leq \varepsilon \text{ for all } j \geq 0\} \\ W^u_\varepsilon(x) &= \{y \in X |\, d(f^{-j}(y), f^{-j}(x)) \leq \varepsilon \text{ for all } j \geq 0\} \end{aligned}$$

it follows that

(i) $W^s_\varepsilon(x)$ *and* $W^u_\varepsilon(x)$ *are differentiable submanifolds;*

(ii) $T_x W^s_\varepsilon(x) = E^s_x$ *and* $T_x W^u_\varepsilon(x) = E^u_x$*;*

(iii) there are constants $C > 0$ *and* $\lambda \in (0,1)$ *such that*

$$\begin{aligned} d(f^j(y), f^j(x)) &\leq C\lambda^j d(x,y) \text{ for } y \in W^s_\varepsilon(x), j \geq 0, \\ d(f^{-j}(y), f^{-j}(x)) &\leq C\lambda^j d(x,y) \text{ for } y \in W^u_\varepsilon(x), j \geq 0; \end{aligned}$$

(iv) $W^s_\varepsilon(x)$ *and* $W^u_\varepsilon(x)$ *are continuously dependent on* x*.*

$W^s_\varepsilon(x)$ *and* $W^u_\varepsilon(x)$ *are called the* **local stable** *and* **unstable manifolds of** x*.*

The existence of these invariant manifolds is guaranteed by the Stable Manifold Theorem, see, for example, Katok and Hasselblatt [66] for a collection of all relevant results in this context. The **global stable** and **unstable manifolds** of x are given by

$$\begin{aligned} W^s(x) &= \bigcup_{j\geq 0} f^{-j}(W^s_\varepsilon(f^j(x))) \text{ and} \\ W^u(x) &= \bigcup_{j\geq 0} f^j(W^u_\varepsilon(f^{-j}(x))). \end{aligned}$$

The following result by Palis (1969) (see e.g. [43], p.247, Thm. 5.2.10) states that the unstable manifold of a hyperbolic fixed point can be approximated by mapping forward a small disk initialized transverse to the stable manifold.

Theorem 2.1.3 (The Lambda Lemma) *Let* f *be a* C^1*-diffeomorphism of* $\mathbb{R}^l$ *with a hyperbolic fixed or periodic point* p *having* s *and* u *dimensional stable and unstable manifolds* ($s+u=l$)*, and let* D *be a* u*-disk in* $W^u(p)$*. Let* Δ *be a* u*-disk meeting* $W^s(p)$ *transversely at some point* q*. Then* $\bigcup_{n\geq 0} f^n(\Delta)$ *contains* u*-disks arbitrarily* C^1 *close to* D*.*

By a u-disk we mean a u-dimensional embedded ball in the l-dimensional phase space. In a two-dimensional dynamical system, Δ can be thought of as a curve intersecting $W^s(p)$ transversely at some point; see Figure 2.1 for an illustration of the theorem.

2.1.2 Attractor

The asymptotic behavior of dynamical systems is captured in the notion of attracting sets or attractors. First we need to briefly review some fundamental concepts.

The asymptotic states of an orbit through a point $x \in X$ are defined in terms of limit sets:

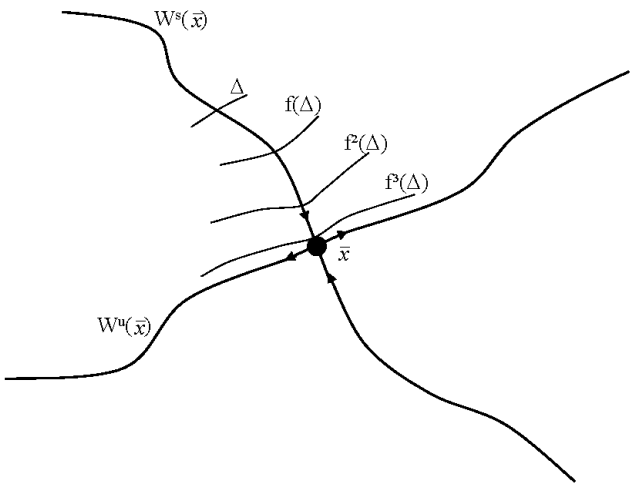

Figure 2.1: A disk transversely intersecting the stable manifold converges to the unstable manifold.

Definition 2.1.4 (ω- and α-limit sets) Let $f : X \to X$ be a continuous map and $x \in X$. The **ω-limit set** of x is defined by

$$\omega(x) = \{y \in X | \exists \text{ a sequence } n_i \to \infty \text{ such that } f^{n_i}(x) \to y\}.$$

If f is a homeomorphism, we define the **α-limit set** of x similarly:

$$\alpha(x) = \{y \in X | \exists \text{ a sequence } n_i \to -\infty \text{ such that } f^{n_i}(x) \to y\}.$$

So limit sets contain the limit points of f^i, $i \in \mathbb{Z}$.

Definition 2.1.5 (Attracting set) An invariant set $A \subset X$ is called an **attracting set with fundamental domain** $U \subset X$, if for every open neighborhood $V \supset A$ there is $J \in \mathbb{N}$ such that $f^j(U) \subset V$ for all $j \geq J$.

The closure of an invariant set is invariant. For a closed attracting set A with fundamental domain U it follows that

$$A = \bigcap_{j \in \mathbb{N}} f^j(U).$$

Now we define the relative global attractor as the attracting set with respect to some bounded set $Q \subset \mathbb{R}^l$:

Definition 2.1.6 (Relative global attractor) Let $Q \subset \mathbb{R}^l$ be a bounded set. We define the **global attractor relative to** Q by

$$A_Q = \bigcap_{j \geq 0} f^j(Q).$$

Remark 2.1.7 Let Q be a neighborhood of a hyperbolic fixed point p. Then it is easily seen that the connected component of $W^u \cap Q$ which contains p is part of A_Q. Moreover, provided Q is small enough, A_Q coincides with this part of the unstable manifold of p, see [24].

Note that the classical definition of an attractor requires an additional minimality condition.

Definition 2.1.8 (Attractor) A closed attracting set A is called an **attractor** if it is indecomposable, that is, for every $x, y \in A$ there is a finite sequence $\{x = x_0, \ldots, x_n = y\}$ such that $d(f(x_{j-1}), x_j) < \varepsilon$.

2.1.3 Ergodic Theory

We briefly introduce some notions from ergodic theory.

Let $\mathcal{B}$ be the Borel-σ-algebra on X. Let m denote the Lebesgue measure and $\mathcal{M}$ the set of probability measures on $(X, \mathcal{B})$. A measure $\mu \in \mathcal{M}$ is called **f-invariant** if

$$\mu(A) = \mu(f^{-1}(A))$$

for all $A \in \mathcal{B}$.

An invariant measure μ is called **ergodic** if $\mu(A) \in \{0, 1\}$ for all invariant sets A.

Definition 2.1.9 An ergodic measure μ is an **SRB-measure** if there exists a subset $U \subset X$ with $m(U) > 0$ such that for each continuous function Ψ

$$\lim_{N\to\infty} \frac{1}{N} \sum_{j=0}^{N-1} \Psi(f^j(x)) = \int \Psi \, d\mu$$

for all $x \in U$. An SRB-measure is also often called the natural or physically relevant measure.

2.1.4 Lyapunov Exponents

Let $f : X \to X$ be a diffeomorphism on a compact subset $X \subset \mathbb{R}^l$. Consider a small (infinitesimal) perturbation ε_0 in the initial condition x_0. With $y_0 = x_0 + \varepsilon_0$ we obtain

$$y_1 = x_1 + \varepsilon_1 = f(y_0) = f(x_0) + Df(x_0) \cdot \varepsilon_0 + \text{ higher order terms.}$$

Thus, ignoring higher order terms, we can write

$$\varepsilon_1 = Df(x_0) \cdot \varepsilon_0.$$

For $k \in \mathbb{N}$ it follows inductively that

$$\varepsilon_{k+1} = Df(x_k) \cdot \varepsilon_k = \prod_{i=0}^{k} Df(x_i) \cdot \varepsilon_0 = Df^k(x_0) \cdot \varepsilon_0.$$

So the evolution of a small displacement ε_0 is governed by the linearized dynamical system. Using these ideas, the average rate of convergence or divergence of neighboring orbits can be measured by Lyapunov exponents. The Multiplicative Ergodic Theorem by Oseledec [85] (see also Ruelle [93]) provides conditions under which these characteristic exponents exist.

We state the version used in Aston and Dellnitz [6]:

Theorem 2.1.10 (Multiplicative Ergodic Theorem) *Let $f : X \to X$ be a diffeomorphism on a compact subset $X \subset \mathbb{R}^l$ and let μ be an ergodic measure. Then there exist real numbers $\lambda_1 > \lambda_2 > \cdots > \lambda_k$ ($k \leq l$), positive integers $l_1, \ldots, l_k$ which satisfy $\sum_{i=1}^{k} l_i = l$ and a measurable decomposition $T_xM = W^{(1)}(x) \oplus \cdots \oplus W^{(k)}(x)$ with $\dim(W^{(i)}(x)) = l_i$ and $Df(W^{(i)}(x)) = W^{(i)}(f(x))$ such that for μ-almost all x*

$$\lim_{n\to\infty} \frac{1}{n} \log \left| Df^n(x)v \right| = \lambda_j,$$

provided that $v \in (W^{(j)}(x) \oplus \cdots \oplus W^{(k)}(x))$ and $v \notin (W^{(j+1)}(x) \oplus \cdots \oplus W^{(k)}(x))$. The numbers $\lambda_1 > \lambda_2 > \cdots > \lambda_k$ are called Lyapunov characteristic exponents with respect to the ergodic measure μ.

Remarks 2.1.11

1. Note that

$$\lim_{n\to\infty} \frac{1}{n} \log \left| Df^n(x)v \right| = \lambda_1,$$

   for almost any choice of v (see e.g. [100], Theorem 9.7, p.349).

2. The dominant Lyapunov exponent λ_1 is a measure of the chaoticity of an attractor. If $\lambda_1 > 0$ then the attractor is chaotic, if $\lambda_1 \leq 0$ we have regular dynamics.

3. A dissipative system is characterized by $\sum_{i=1}^{k} \lambda_i < 0$, a conservative system by $\sum_{i=1}^{k} \lambda_i = 0$.

The Multiplicative Ergodic Theorem guarantees the existence of Lyapunov exponents only for μ-almost all x. This definition is not very useful in our context because we are especially interested in regions of measure zero. Therefore, we give the following alternative definition of (local) Lyapunov exponents, which will be used in the remainder of this thesis:

Definition 2.1.12 Let $f : X \to X$ be a diffeomorphism on a compact subset $X \subset \mathbb{R}^l$. Then for $N \in \mathbb{N}$ the **expansion rate** or finite-time Lyapunov exponent is defined as

$$\Lambda(N, x_0) = \frac{1}{N} \log |Df^n(x_0)| = \frac{1}{N} \log |\prod_{i=0}^{N-1} Df(x_i)|.$$

The (dominant local) **Lyapunov exponent** is given by

$$\lambda(x_0) = \limsup_{N \to \infty} \Lambda(N, x_0).$$

Note that $\lambda(x)$ is guaranteed to exist for all $x \in X$. Moreover, for fixed $N \in \mathbb{N}$ the expansion rate $\Lambda(N, x)$ is continuous in x and one has point-wise convergence to the dominant local Lyapunov exponents. $\lambda(x)$ is typically not continuous in phase space but a singular function of the phase space coordinates [20]. For the sake of simplicity, $\lambda(x)$ will be referred to as *the* Lyapunov exponent with respect to the initial condition x.

It is a simple task to check that Lyapunov exponents are f-invariant and hence constant along orbits. Therefore, the Lyapunov exponents defined this way are related to orbits and hence, can be seen as local Lyapunov exponents. In contrast, the exponents obtained by the Multiplicative Ergodic Theorem are given with respect to an ergodic measure, which means, that they characterize the dynamical system rather than a single orbit.

In the following paragraphs we derive some characteristics of the (local) Lyapunov exponent for special classes of orbits.

Proposition 2.1.13 *Let $x_{n+1} = f(x_n)$ be a dynamical system defined by the diffeomorphism $f : X \to X$, $X \subset \mathbb{R}^l$.*

1. *Let $\bar{x}$ be a fixed point, that is, $\bar{x} = f(\bar{x})$. Then $\lambda(\bar{x}) = \log \rho(Df(\bar{x}))$. Here ρ denotes the spectral radius of a matrix.*

2. *Let $\{\bar{x}_0, \bar{x}_1, ..., \bar{x}_{p-1}\}$ be a periodic orbit of period $p > 1$, that is, $f^p(\bar{x}_i) = \bar{x}_i$. Then $\lambda(\bar{x}_i) = \frac{1}{p} \log \rho(Df^p(\bar{x}_0))$ for $i = 0, ..., p-1$.*

The continuous dependence of the expansion rate on x is used to prove the following result on limit sets:

Proposition 2.1.14 *Let $x \in X$ and $\omega(x) = \{\bar{x}\}$ with $\bar{x} = f(\bar{x})$, that is,*

$$\lim_{n \to \infty} f^n(x) = \bar{x}.$$

Then $\lambda(x) = \lambda(\bar{x})$.

Proof: $\limsup_{N\to\infty}\Lambda(N,x)=\lambda(x)$ exists point-wise for all x and $\lambda(x)$ is constant along orbits. Moreover, we have $\lim_{n\to\infty} f^n(x)=\bar{x}$ and, as the factors in the matrix product $\prod_{i=0}^{N-1} Df(x_i)$ converge to constant matrices, it follows that $\lim_{N\to\infty}\Lambda(N,x)=\limsup_{N\to\infty}\Lambda(N,x)$. Using a result from elementary calculus we can conclude that the two limits

$$\begin{aligned}\lim_{N\to\infty}\lim_{k\to\infty}\Lambda(N,f^k(x)) &= \lim_{N\to\infty}\Lambda(N,\bar{x})=\lambda(\bar{x})\\ \lim_{k\to\infty}\lim_{N\to\infty}\Lambda(N,f^k(x)) &= \lim_{k\to\infty}\lambda(f^k(x))=\lambda(x)\end{aligned}$$

exist and are equal. □

We can use f^p to obtain an analogous result if $\omega(x)=\{x_0,\ldots,x_{p-1}\}$ is a periodic orbit.

The following remarks sum up a few results for the special case of autonomous continuous systems:

Remarks 2.1.15 Let $\dot{x}=f(x)$ be an autonomous dynamical system, $x\in\mathbb{R}^l$ and $f:\mathbb{R}^l\to\mathbb{R}^l$ C^r with $r\geq 1$. Let ϕ^t be the flow. The Multiplicative Ergodic Theorem gives conditions under which Lyapunov exponents λ_i exist. Similarly, we define

$$\lambda(x_0)=\limsup_{t\to\infty}\frac{1}{t}\log\left|D\phi^t(x_0)\right|.$$

Then the following holds

- Let $\bar{x}$ be a hyperbolic fixed point of $\dot{x}=f(x)$, that is, $\phi^t\bar{x}=\bar{x}$ and $Df(\bar{x})$ has no eigenvalues on the imaginary axis. Note that in this case the Hartman-Grobman theorem for flows ([94], p.22, Theorem 5.4) applies. Then

$$\lambda(\bar{x})=\max_{\lambda}\{\mathrm{Re}(\lambda):\lambda \text{ eigenvalue of } Df(\bar{x})\}.$$

- If x is a state on a periodic orbit, then $\lambda(x)$ is related to the maximum eigenvalue of the monodromy matrix.

- Let $x\in X$. Unless $\omega(x)$ contains a stationary solution, there is a j such that $\lambda_j=0$. This is related to the direction tangential to the trajectory.

- A time-continuous dynamical system must be at least three-dimensional to exhibit a chaotic attractor: with $\lambda_1>0$, $\lambda_2=0$, and requiring $\sum_i\lambda_i<0$, it follows that $\lambda_3<0$.

- For Hamiltonian systems, the Lyapunov exponents exist in additive inverse pairs, so if $\lambda>0$ is a characteristic exponent, then so is $-\lambda$, ensuring that $\sum_i\lambda_i=0$.

The following example illustrates these ideas.

Example 2.1.16 (The Duffing oscillator) Let $Q \subset \mathbb{R}^2$ be a compact set. The Duffing oscillator is a non-autonomous second order differential equation:

$$\ddot{x} + \delta\dot{x} - x + x^3 = \gamma \cos \omega t. \tag{2.1}$$

For a detailed analytical analysis see for example [43].

We consider the dynamical system without periodic forcing, so it can be written as a first order system:

$$\begin{aligned} \dot{x_1} &= x_2 \\ \dot{x_2} &= -\delta x_2 + x_1 - x_1^3. \end{aligned}$$

For $\delta = 0.25$, the system exhibits a saddle point at the origin and two sinks at $(\pm 1, 0)$, see Figure 2.2 a). Using the results derived in this section, it follows that $\lambda(x) = -0.1250$ for all $x \in Q \setminus W^s([0,0])$, and $\lambda(x) = 0.8828$ for all $x \in Q \cap W^s([0,0])$, which are the dominant Lyapunov exponents of the two sinks and the saddle, respectively. Consequently, in this example, the value of the Lyapunov exponent can be used to identify the separatrix between two basins of attraction.

Choosing $\delta = 0$, there is a saddle at $(0,0)$ with dominant Lyapunov exponent 1 and two centers at $(\pm 1, 0)$ with zero Lyapunov exponent. Apart from the three fixed points and the homoclinic connections formed by the stable and unstable manifold of the saddle, the system exhibits families of periodic orbits, see Figure 2.2 b). As the system is conservative, it follows that $\lambda(x) = 0$ for all x that are not asymptotic to the saddle point. So again, the stable manifold of the saddle point is characterized by a positive Lyapunov exponent, while all other points have a zero Lyapunov exponent.

In Chapter 4 we will see that such a maximizing property of the stable manifold of hyperbolic points does not only apply to this special simple case but is a general characteristics of the Lyapunov exponent. Moreover, we will see that, even for a relatively small number of iterations, stable manifolds serve as local maximizers of the expansion rate. This feature will be exploited for the numerical detection and extraction of these relevant dynamical objects.

2.2 Non-Autonomous Dynamical Systems

2.2.1 Hyperbolic Trajectories and Invariant Manifolds

We now consider systems of ordinary differential equations of the form

$$\dot{x} = f(x,t), \tag{2.2}$$

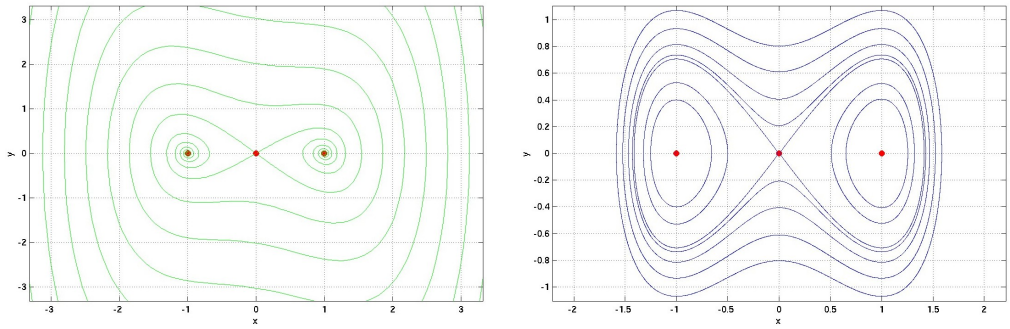

a) b)

Figure 2.2: Duffing oscillator for $\gamma = 0$. a) $\delta = 0.25$: Saddle at the origin and two sinks at $(\pm 1, 0)$. The unstable manifold of the saddle spirals into the sinks, the stable manifold forms a separatrix between the two basins of attraction of the sinks. b) $\delta = 0$: Saddle at the origin and two centers at $(\pm 1, 0)$. Stable and unstable manifolds of the saddle form two homoclinic orbits.

with states $x \in \mathbb{R}^l$, time $t \in \mathbb{R}$ and we assume the vector field (or velocity field) $f : \mathbb{R}^l \times \mathbb{R} \to \mathbb{R}^l$ to be C^r, $r \geq 1$, in x and continuous in t.

The smoothness assumptions above permit linearization and ensure that the initial value problem

$$\dot{x} = f(x, t), \; x(t_0) = x_0 \tag{2.3}$$

has a unique solution, which we denote by

$$\varphi^{t,t_0}(x_0) := x(x_0, t_0; t).$$

If not otherwise stated, we assume that this unique solution exists for all $t \in \mathbb{R}$.

The family of mappings $\{\varphi^{t,s}\}_{t \geq s}$, for $t, s \in \mathbb{R}$, satisfies the properties

1. $\varphi^{t,t} = id$;

2. $\varphi^{t,s} = \varphi^{t,r} \circ \varphi^{r,s}$, for $r, s, t \in \mathbb{R}$,

and therefore fulfills in particular the definition of a **cocycle** (see e.g. [97]).

We now give a formal definition of a non-autonomous dynamical system; see for example [68]:

Definition 2.2.1 (Non-autonomous dynamical system) With state space $\mathbb{R}^l$ and a time set $\mathbb{T}$, a **non-autonomous dynamical system** consists of a pair of mappings (θ, Φ), where

(i) θ is an autonomous dynamical system on a nonempty parameter set P, satisfying

$$\theta_t : P \to P,\ \theta_t \circ \theta_s = \theta_{t+s},\ \theta_0 = \mathrm{id}_P,$$

for all, $s, t \in \mathbb{T}$;

(ii) Φ is a cocycle mapping on $\mathbb{R}^l$, with $\Phi : \mathbb{T}^+ \times P \times \mathbb{R}^l \to \mathbb{R}^l$ and

$$\Phi(0, p, x_0) = x_0,\ \Phi(t + s, p, x_0) = \Phi(t, \theta_s p, \Phi(s, p, x_0)),$$

for all $s, t \in \mathbb{T}^+$, $p \in P$ and $x_0 \in \mathbb{R}^l$.

Obviously, $\Phi : \mathbb{R} \times \mathbb{R} \times \mathbb{R}^l \to \mathbb{R}^l$ with $\Phi(T, t_0, x) = \varphi^{T+t_0,t_0}x$ satisfies the definition of a non-autonomous system. Therefore, when in the course of this thesis we refer to a non-autonomous dynamical system we mean this system induced by the cocycle $\{\varphi^{t,s}\}$.

Notably, this cocycle and consequently the solution to the initial value problem are usually not given analytically but need to be approximated using an integration scheme, such as an explicit Runge-Kutta integration scheme.

In the case where the differential equation has periodic time dependence, we can reduce the analysis of the dynamics to the general autonomous discrete case by considering an appropriate Poincaré map, see for example the book by Guckenheimer and Holmes [43] for a detailed introduction.

Hyperbolic trajectories serve as the time-dependent generalization of hyperbolic fixed points. A trajectory γ is given by the continuous map $\gamma : \mathbb{R} \to \mathbb{R}^l$ with $\varphi^{t,s}(\gamma(s)) = \gamma(t)$. For the definition of a hyperbolic trajectory we need to introduce the concept of exponential dichotomies, see Coppel [16] for a classical reference.

Definition 2.2.2 (Exponential dichotomy) Consider the linear ordinary differential equation with time-dependent coefficients:

$$\dot{\xi} = A(t)\xi, \qquad \xi \in \mathbb{R}^l, \tag{2.4}$$

where $A(t) \in \mathbb{R}^{l,l}$ is a continuous function of t. Let $X(t) \in \mathbb{R}^{l,l}$ be the fundamental matrix solution of (2.4) with $\xi(t) = X(t)\xi_0$ a solution passing through ξ_0 at $t = 0$ and $X(0) = I$. Then (2.4) is said to possess an **exponential dichotomy** if there exists a projection operator $P \in \mathbb{R}^{l,l}$, $P^2 = P$ and constants $K_1, K_2 \geq 1$, $\lambda_1, \lambda_2 > 0$ such that

$$||X(t)PX^{-1}(\tau)|| \leq K_1 \exp(-\lambda_1(t - \tau)), t \geq \tau, \tag{2.5}$$

$$||X(t)(I - P)X^{-1}(\tau)|| \leq K_2 \exp(\lambda_2(t - \tau)), t \leq \tau. \tag{2.6}$$

Definition 2.2.3 (Hyperbolic trajectory) Let $\gamma(t)$ denote a trajectory of the vector field $\dot{x} = f(x,t)$. Then $\gamma(t)$ is said to be a **hyperbolic trajectory** if the associated linearized system

$$\dot{\xi} = Df(\gamma(t),t)\xi$$

has an exponential dichotomy.

See Katok and Hasselblatt [66], Def. 6.2.6, for a definition in the discrete time case. As the constants are chosen independently of τ and t, often the term **uniformly hyperbolic** is used. Uniformly hyperbolic solutions attract initial conditions along certain directions and repel them along other directions; the operator P allows a projection onto the stable and unstable subspaces.

The geometrical picture of the notion of exponential dichotomy is more easily understood in the extended phase space:

$$\mathcal{E} := \{(x,t) \in \mathbb{R}^l \times \mathbb{R}\},$$

that is, we append the variable t to the phase space. Now we can consider the velocity field defined on the extended phase space as follows

$$\dot{x} = f(x,t), \tag{2.7}$$
$$\dot{t} = 1, \tag{2.8}$$

and the hyperbolic trajectory in $\mathcal{E}$ is denoted by

$$\Gamma(t) = (\gamma(t),t).$$

Strictly speaking, the hyperbolicity is lost when we consider the respective trajectories in the extended phase space. This is due to the additional direction tangent to the trajectory. Therefore, we will call $\Gamma(t) = (\gamma(t),t)$ a hyperbolic trajectory in the extended phase space if $\gamma(t)$ is hyperbolic.

The extended phase space is foliated by time-slices: We define a **time-slice** or **τ-fiber** of the extended phase space $\mathcal{E}$ by

$$\Sigma(\tau) := \{x \in \mathbb{R}^l | (x,\tau) \in \mathcal{E}\}.$$

Figure 2.3 illustrates this notion. Note that $\Gamma(t)$ intersects $(\Sigma(\tau),\tau)$ in the unique point $\gamma(\tau)$.

Remark 2.2.4 Note that in Chapter 5 τ-fibers $\Sigma(\tau)$ will be used for two different purposes. Usually, we will consider τ-fibers to identify a set of initial conditions with respect to a fixed time. Solutions with respect to these initial values will then be computed in *phase space*. On the other hand, we will can choose initial conditions on a τ-fiber to compute trajectories in the *extended phase space* $\mathcal{E}$.

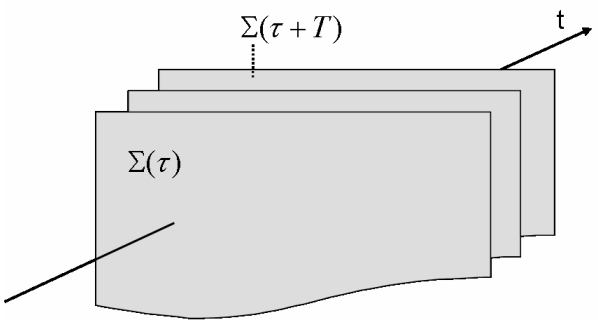

Figure 2.3: The extended phase space of a non-autonomous system is foliated by time slices or fibers.

Definition 2.2.5 (Non-autonomous set [7]) We call a set $\Sigma \subset \mathcal{E}$ a **non-autonomous set** if for all $\tau \in \mathbb{R}$ the τ-fibers are non-empty. Σ is closed or compact, if all τ-fibers are closed or compact. Finally Σ is forward invariant if $\varphi^{t,\tau}(\Sigma(\tau)) \subset \Sigma(t)$ for $t \geq \tau$ and invariant if $\varphi^{t,\tau}(\Sigma(\tau)) = \Sigma(t)$ for all $t, \tau \in \mathbb{R}$.

The following theorem establishes the existence of stable and unstable manifolds for hyperbolic trajectories.

Theorem 2.2.6 (Stable and unstable manifolds [78]) *Let the set-up be as described above, and suppose that the projection operator P has rank k. Let $\mathcal{D}_\rho(\tau) \in (\Sigma(\tau), \tau)$ denote the ball of radius ρ centered at $\gamma(\tau)$ and define the tubular neighborhood of $\Gamma(t)$ in $\mathcal{E}$ as*

$$\mathcal{N}(\Gamma(t)) := \bigcup_{\tau \in \mathbb{R}} (\mathcal{D}_\rho(\tau), \tau).$$

Then in the extended phase space $\mathcal{E}$ there exists a $(k+1)$-dimensional C^r manifold $W^s_{loc}(\Gamma(t)) \subset \mathcal{E}$, and an $(l-k+1)$-dimensional C^r manifold $W^u_{loc}(\Gamma(t)) \subset \mathcal{E}$, and ρ_0 sufficiently small such that for $\rho \in (0, \rho_0)$:

1. *$W^s_{loc}(\Gamma(t))$, the local stable manifold of $\Gamma(t)$, is invariant under the forward time evolution generated by (2.2).*
   $W^u_{loc}(\Gamma(t))$, the local unstable manifold of $\Gamma(t)$, is invariant under the backward time evolution generated by (2.2).

2. *$W^s_{loc}(\Gamma(t))$ and $W^u_{loc}(\Gamma(t))$ intersect along $\Gamma(t)$, and the angle between the manifolds is bounded away from zero uniformly for all $t \in \mathbb{R}$.*

3. *Every trajectory on $W^s_{loc}(\Gamma(t))$ can be continued to the boundary of $\mathcal{N}(\Gamma(t))$ in backward time, and every trajectory on $W^u_{loc}(\Gamma(t))$ can be continued to the boundary of $\mathcal{N}(\Gamma(t))$ in forward time.*

4. *Trajectories starting on $W^s_{loc}(\Gamma(t))$ at a time $t = \tau$ approach $\Gamma(t)$ at an exponential rate $e^{-\lambda^s(t-\tau)}$ as $t \to \infty$, for some constant $\lambda^s > 0$. Similarly, trajectories starting on $W^u_{loc}(\Gamma(t))$ at a time $t = \tau$ approach $\Gamma(t)$ at an exponential rate $e^{-\lambda^u|t-\tau|}$ as $t \to -\infty$, for some constant $\lambda^u > 0$.*

5. *Any trajectory in $\mathcal{N}(\Gamma(t))$ not on either $W^s_{loc}(\Gamma(t))$ or $W^u_{loc}(\Gamma(t))$ will leave $\mathcal{N}(\Gamma(t))$ in both forward and backward time.*

Comments and references to the proof and related results are given in [78, 80]. Notably, the above theorem is a consequence of the Hadamard-Perron theorem, see for example Katok and Hasselblatt [66], Thm. 6.2.8, who also give a detailed proof for the discrete time setting. Also [19, 58] state stable manifold theorems for the discrete time-dependent case.

Finally, hyperbolic trajectories and their invariant manifolds persist under small perturbations; see for example Malhotra et al. [78] and references therein.

2.2.2 Pullback Attractor

Similar to the autonomous case, there is also a concept of attracting sets in the non-autonomous setting. The notions of the pullback attraction idea for non-autonomous and random dynamical systems are discussed and used for example in Aulbach et al. [7, 8], Cheban et al. [15], Keller and Ochs [67], Kloeden et al. [69, 68], Schmalfuss [97], and Siegmund [104].

Definition 2.2.7 (Cocycle absorbing set [69]) A compact non-autonomous set B is called a **cocycle absorbing set** for the cocycle $\{\varphi^{t,s}\}$ on $\mathbb{R}^l$ if for each $\tau \in \mathbb{R}$ and every bounded subset $D \subset \mathbb{R}^l$ there exists a $t_D(\tau) \geq 0$ such that

$$\varphi^{\tau,\tau-t}(D) \subseteq B(\tau) \text{ for all } t \geq t_D(\tau).$$

It is said to be **uniformly absorbing** if $t_D(\tau)$ is independent of τ.

Definition 2.2.8 (Global pullback attractor) An invariant compact non-autonomous set Σ is called a **global pullback attractor** if for any compact set $C \in \mathbb{R}^l$ we have

$$\lim_{t\to\infty} d(\varphi^{\tau,\tau-t}(C), \Sigma(\tau)) = 0 \text{ for all } \tau \in \mathbb{R},$$

where d denotes the Hausdorff semi-distance.

This concept of attraction considers a fixed final time and moves the initial time to $-\infty$. This does not mean that we are going backwards in time but rather that we consider the asymptotic state of the system on a τ-fiber arising from the initial conditions starting at time $-\infty$. The following statement gives an existence and uniqueness result for pullback attractors.

Theorem 2.2.9 ([69]) *Let B be a cocycle absorbing set for the cocycle $\{\varphi^{t,s}\}$. Then there exists a pullback attractor Σ uniquely determined by*

$$\Sigma(\tau) = \bigcap_{s\geq 0} \overline{\bigcup_{t\geq s} \varphi^{\tau,\tau-t}(B(\tau-t))}.$$

Under conditions on the spectral gap in the dichotomy spectrum, as well as on the nonlinearity, Aulbach et al. [8] show that the unstable manifold of a hyperbolic trajectory in a non-autonomous dynamical system is a global pullback attractor. Similarly, the stable manifold is pullback attracting in such systems under time reversal. Siegmund [104] considers a non-autonomous difference equation and restricts the analysis to a cylinder around a hyperbolic orbit. Under these conditions, he proves that the (local) unstable manifold coincides with the global pullback attractor.

2.2.3 Lyapunov Exponents

In analogy to the Multiplicative Ergodic Theorem in the discrete time case, we obtain the existence of Lyapunov exponents. Let $\varphi^{t+t_0,t_0}(x_0)$ denote a solution which exists for all $t \geq 0$. We are interested in describing the dynamics near that trajectory. For this we study the linear vector field

$$\dot{\xi} = Df(\varphi^{t+t_0,t_0}(x_0))\xi, \qquad \xi \in \mathbb{R}^l$$

Let $X(t+t_0, \varphi^{t+t_0,t_0}(x_0)) \equiv X(t)$ denote a fundamental matrix solution. Note that $X(t) = D\varphi^{t+t_0,t_0}x_0$ solves the variational equation, and clearly $X(0) = I$. In analogy to the autonomous case, the **expansion rates** are given as

$$\Lambda(T; t_0, x_0) := \frac{1}{t} \log |D\varphi^{t+t_0,t_0}(x_0)|,$$

and we denote the dominant **Lyapunov exponent** by

$$\lambda(t_0, x_0) := \limsup_{t\to\infty} \frac{1}{t} \log |D\varphi^{t+t_0,t_0}(x_0)|.$$

The Multiplicative Ergodic Theorem [85] gives again conditions under which even the limit as $t \to \infty$ exists, see also Hahn [44] (Theorem 64.4, p.318) for the necessary regularity conditions on $Df(x(t), t)$. Note that Lyapunov exponents and exponential dichotomy are related in the following way: the size of the Lyapunov exponents is determined by the Sacker-Sell spectrum [95], that is those values of $\lambda \in \mathbb{R}$ for which the shifted system $\dot{\xi} = (A(t) - \lambda I)\xi$, with $A(t) := D\varphi^{t+t_0,t_0}(x_0)$, does not satisfy an exponential dichotomy; see for example [33, 34] for a discussion.

Again, Lyapunov exponents are constant along trajectories and unaffected by what happens on a finite time interval.

2.3 Finite-Time Velocity Fields

In the previous paragraphs we have stated definitions for time-dependent dynamical systems. We now address the case that the velocity field is only defined on a finite time interval $[t_-, t_+]$ with $-\infty < t_- < t_+ < \infty$. Two common examples for this case are that the time-dependent vector field is not given analytically but obtained as the numerical solution of a partial differential equation such as the Navier-Stokes equation, or from experimental measurement data. In both cases the velocity field is, by construction, discrete in space and time and only defined for finite times.

In this setting, notions from dynamical systems such as hyperbolicity, stable and unstable manifolds, or Lyapunov exponents become problematic as they are based on asymptotic quantities. In the last few years mathematically consistent concepts that deal with **finite-time velocity fields** [56] have been developed. However, these attempts are far from providing a uniform theory. We briefly introduce some characteristics of finite-time velocity fields.

Following Ide et al. [56] we start by defining finite-time hyperbolicity:

Definition 2.3.1 (Finite-time hyperbolic trajectory) Let $\gamma(t)$ denote a trajectory of the vector field $\dot{x} = f(x,t)$ on $[t_-, t_+]$. Then $\gamma(t)$ is said to be a **(uniformly) hyperbolic trajectory** on $[t_-, t_+]$ if the associated linearized system

$$\dot{\xi} = Df(\gamma(t), t)\xi$$

has an exponential dichotomy on $[t_-, t_+]$ (see Definition 2.2.2).

There are two different contexts in which the existence of finite-time invariant manifolds has been analyzed, see Jones and Winkler [61] for a detailed discussion.

The first is due to Haller and Poje [49]. They derive conditions on $f(x,t)$ under which the dynamical system admits finite-time hyperbolic trajectories, relying on the existence of a hyperbolic fixed point for each τ-fiber on the interval of existence. Hence, their approach is tailored to situations where the time dependence is relatively weak. For the construction of the manifolds, a contraction mapping argument is used, for which the original vector field is modified outside the interval $[t_-, t_+]$. As this extension can be chosen differently, the resulting manifolds are not unique. However, if the interval under consideration is long enough, the manifolds are determined up to exponentially small errors, that is, they are exponentially close to the manifolds that would be obtained if the system was available for infinite times.

The second approach is due to Sandstede et al. [96] in the context of an application to Melnikov theory. There the authors smoothly extend the vector field outside of its time range of definition. They assume $t_- = t_-(\varepsilon)$, $t_+ = t_+(\varepsilon)$

with $t_- \to -\infty$ for $\varepsilon \to 0$ and $t_+ \to \infty$ and require that the perturbed vector field coincides with the unperturbed field on the finite time span. Standard theory provides them with invariant manifolds for a hyperbolic trajectory. As in Haller and Poje [49], these manifolds depend upon the way the extension is constructed, and again, the larger the time range of definition of the original vector field, the closer are the invariant manifolds for different extensions.

The actual definitions of the manifolds are similar in Haller and Poje [49] and Sandstede et al. [96]. Both postulate that all solutions which, while in $[t_-, t_+]$, stay close to the hyperbolic trajectory - for example, in a box or tube around the trajectory in the extended phase space - in forward time form the stable manifold. The unstable manifold is defined by considering the solutions in backward time. The definition by Haller and Poje [49] summarizes this description:

Definition 2.3.2 (Finite-time invariant manifolds) Let $\Gamma(t)$, $t \in [t_-, t_+]$, be a finite-time hyperbolic trajectory in the extended phase space. Then we define **finite-time invariant manifolds** in the following way:

$$\begin{aligned} W^s_{loc}(t_-, t_+) &= \{(z(t), t) : |z(t; z_0) - \Gamma(t)| \leq |z(t_-; z_0) - \Gamma(t_-)|, t \in (t_-, t+]\}, \\ W^u_{loc}(t_-, t_+) &= \{(z(t), t) : |z(t; z_0) - \Gamma(t)| \leq |z(t_+; z_0) - \Gamma(t_+)|, t \in [t_-, t+)\}. \end{aligned}$$

Note that by the smoothness of the flow with respect to the initial condition, these sets are closed, their boundaries are piecewise smooth, and they have non-zero volume in the extended phase space [49]. However, the manifolds constructed this way may contain solutions that would not stay within the prescribed neighborhood of the hyperbolic trajectory if longer time spans would be considered. Hence, this again shows their nonuniqueness, which, as discussed above, will not be resolved numerically if long enough time intervals are available. Note that the nature of this concept is local and therefore the existence of global stable and unstable manifolds is not immediately included.

The definition of Lyapunov exponents as before is not possible as this notion is based on asymptotic quantities. Instead we define finite-time exponents:

Definition 2.3.3 (Finite-time Lyapunov exponents) Let $\dot{x} = f(x, t)$ be a time-dependent differential equation. Let $x(t)$ be a solution on $[t_-, t_+]$ with respect to the initial value $x(t_0) = x_0$. Then the dominant **finite-time Lyapunov exponent** or **expansion rate** is defined as

$$\lambda(t; t_0, x_0) := \frac{1}{t} \log |D\varphi^{t+t_0, t_0}(x_0)|,$$

where $t_0, t + t_0 \in [t_-, t_+]$.

Notably, $\lambda(t; t_0, x_0)$ depends on the initial condition and the initial time as well as the integration time.

In Malhotra et al. [78] and Wiggins [112] an alternative definition for a finite-time hyperbolic trajectory is used. In their setting, a trajectory is finite-time hyperbolic on $[t_-, t_+]$ if none of its finite-time Lyapunov exponents are zero on this interval. They show that this definition is equivalent to the dichotomy based concept. In Chapter 5 we briefly address the relation between these two different notions and also discuss that finite-time invariant manifolds are typically characterized by large finite-time Lyapunov exponents.

Following the fundamental work by Haller [45, 46, 47], in a recent manuscript, Shadden, Lekien, and Marsden [102] define Lagrangian coherent structures as ridges in the scalar finite-time Lyapunov exponent field. They derive an analytical formula for the flux across these structures and show that is it nearly zero. Hence, Lagrangian coherent structures are nearly invariant and, therefore, candidates of finite-time invariant manifolds.

Chapter 3

The Set Oriented Approach

We briefly review the set oriented algorithms for the numerical approximation of (relative) global attractors and invariant manifolds as introduced by Dellnitz and Hohmann [23, 24]. Extensions and applications of this set oriented approach can be found, for example, in [13, 21, 25, 26, 27, 32, 65]. In a short section we show how these methods can be used in the non-autonomous case [8, 7, 104]. All these algorithms can be efficiently carried out using the software package GAIO (*Global Analysis of Invariant Objects*) [21] and its extensions. The set oriented approach provides a basis for the numerical methods established in the following chapters.

It is worth mentioning that set oriented methods also provide a natural basis for the approximation of invariant measures, as discussed for example in [21, 25, 26, 64], or the computation of Lyapunov exponents as suggested by Aston and Dellnitz [5, 6].

3.1 The Subdivision Algorithm

The set oriented subdivision algorithm computes relative global attractors as defined in the previous chapter. Recall that the global attractor relative to the compact set Q is defined as

$$A_Q = \bigcap_{j \geq 0} f^j(Q),$$

and that it contains all unstable manifolds in Q. The subdivision algorithm generates a sequence $\mathcal{B}_0, \mathcal{B}_1, \mathcal{B}_2, \ldots$ of finite collections of compact subsets (boxes) of $\mathbb{R}^n$ such that for all $k \in \mathbb{N}$,

$$Q_k = \bigcup_{B \in \mathcal{B}_k} B, \text{ with } B \cap B' = \emptyset \text{ for } B \neq B' \in \mathcal{B}_k$$

is a covering of A_Q. Moreover, the diameter of the boxes

$$\operatorname{diam}(\mathcal{B}_k) = \max_{B \in \mathcal{B}_k} \operatorname{diam}(B)$$

converges to zero as $k \to \infty$. The algorithm works in two steps, the subdivision and the selection step:

Algorithm 3.1.1 Given an initial collection $\mathcal{B}_0$, one inductively obtains $\mathcal{B}_k$ from $\mathcal{B}_{k-1}$ for $k = 1, 2, \ldots$ in two steps.

1. *Subdivision*: Construct a new collection $\hat{\mathcal{B}}_k$ such that

$$\bigcup_{B \in \hat{\mathcal{B}}_k} B = \bigcup_{B \in \mathcal{B}_{k-1}} B \qquad \text{and } \operatorname{diam}(\hat{\mathcal{B}}_k) \leq \theta \operatorname{diam}(\mathcal{B}_{k-1})$$

   for some $0 < \theta < 1$.

2. *Selection*: Define the new collection $\mathcal{B}_k$ by

$$\mathcal{B}_k = \{B \in \hat{\mathcal{B}}_k \,:\, f^{-1}(B) \cap \hat{B} \neq \emptyset \text{ for some } \hat{B} \in \hat{\mathcal{B}}_k\}.$$

The selection criterion can be efficiently tested using a set of test points in each box B. These test points are mapped forward and B is discarded unless it contains an image point of some box. This procedure can be made rigorous in the case where local Lipschitz constants for f are available [64]. Moreover, the boxes are stored in a binary tree, where the children of a box at depth k are constructed by bisecting the box in alternating coordinate directions; see Figure 3.1 for an illustration. This does not only allow for rapid searching of which box contains images of test points, but also for handling large numbers of boxes within reasonable memory requirements.

Note that it is possible to impose other selection criteria in order to deal with constraints or approximate, for example, the chain recurrent set of f [27]. Without selection however, one obtains an efficient discretization or **partition** of the phase space.

We end this section with the following proposition, which states a convergence property of the subdivision algorithm 3.1.1:

Proposition 3.1.2 ([24]) *Let A_Q be the global attractor relative to the compact set Q, and let $\mathcal{B}_0$ be a finite collection of closed subsets with $Q_0 = Q$. Then*

$$\lim_{k \to \infty} d_H(A_Q, Q_k) = 0.$$

See Dellnitz and Hohmann [24] for a detailed proof of this statement.

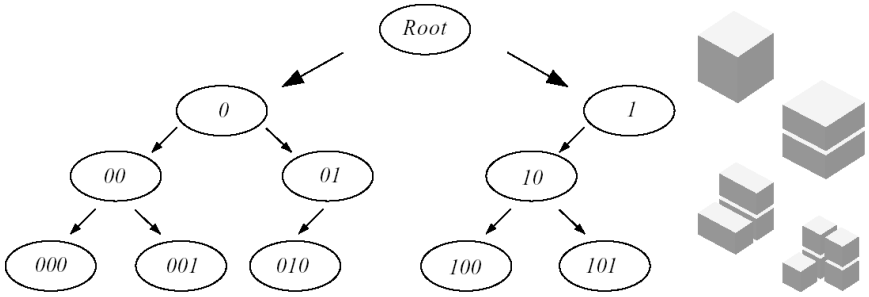

Figure 3.1: Hierarchical storage of the box collections in the software package GAIO. Illustration taken from [27].

Example 3.1.3 (The Hénon attractor) For illustration we apply the subdivision algorithm to the Hénon map [51]

$$h(x, y) = (1 + y - ax^2, bx),$$

with $a = 1.4$ and $b = 0.3$. Figure 3.2 shows a nested sequence of box coverings of the relative global attractor in the Hénon system with respect to $Q = [-1.35, 1.35] \times [-0.5, 0.5]$. The results after 2, 6, 10, and 14 steps in the subdivision algorithm are shown and demonstrate the convergence of the covering towards the Hénon attractor.

3.2 The Continuation Algorithm

The continuation algorithm supplements the subdivision algorithm introduced above. It is used to, roughly speaking, globalize the local unstable manifold of a hyperbolic fixed point or periodic point $p \in \mathbb{R}^n$. Let $Q \subset \mathbb{R}^n$ and for $l = 0, 1, \ldots$ let

$$\mathcal{P}_l = \bigcup_{B \in \mathcal{B}_l} B, \text{ with } B \cap B' = \emptyset \text{ for B } \neq B' \in \mathcal{B}_l$$

be a partition of Q on level (depth) l, obtained by applying the subdivision step (1.) in Algorithm 3.1.1 l times with respect to the initial box $\mathcal{B}_0 := Q$. Obviously, the $\mathcal{P}_l$, $l \in \mathbb{N}$, form a nested sequence of successively finer partitions of Q. For $x \in Q$, let $\mathcal{P}_l(x) \in \mathcal{P}_l$ denote the element or box of $\mathcal{P}$ containing x. Then we obtain for any point $x \in Q$ a unique sequence $\{\mathcal{P}_l(x)\}$. Now assume that $C = \mathcal{P}_l(p)$ is a neighborhood of the hyperbolic fixed point p such that the global

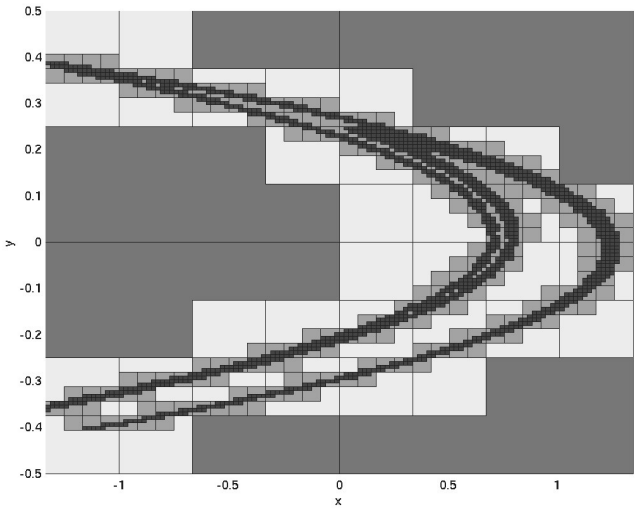

Figure 3.2: Nested sequence of coverings of the Hénon attractor, obtained after 2, 6, 10, and 12 steps in the subdivision algorithm.

attractor relative to C satisfies

$$A_C = W^u_\varepsilon(p) \cap C.$$

Applying the subdivision algorithm with k subdivision steps to $\mathcal{B}_0 = \{C\}$, we obtain a covering $\mathcal{B}_k \subset \mathcal{P}_{k+l}$ of the local unstable manifold $W^u_\varepsilon(p) \cap C$, that is

$$A_C = W^u_\varepsilon(p) \cap C \subset \bigcup_{B \in \mathcal{B}_k} B.$$

As shown in the previous section, the covering converges to A_C for $k \to \infty$. We can now a apply a continuation scheme for the approximation of the global unstable manifold.

Algorithm 3.2.1 For a fixed k we define a sequence $\mathcal{C}^{(k)}_0, \mathcal{C}^{(k)}_1, \ldots$ of subsets $\mathcal{C}^{(k)}_j \subset \mathcal{P}_{l+k}$ by

1. *Initialization:*
$$\mathcal{C}^{(k)}_0 = \mathcal{B}_k.$$
2. *Continuation:* For $j = 0, 1, \ldots$ compute
$$\mathcal{C}^{(k)}_{j+1} = \{B \in \mathcal{P}_{l+k} \,:\, B \cap f(B') \neq \emptyset \text{ for some } B' \in \mathcal{C}^{(k)}_j\}.$$

The algorithm stops if no more boxes are added to the current collection. Observe that the unions

$$C_j^{(k)} = \bigcup_{B \in \mathcal{C}_j^{(k)}} B$$

form nested sequences in k, that is, $C_j^{(0)} \supset C_j^{(1)} \ldots$. Let $W_0 = W_\varepsilon^u(p) \cap C$ and define inductively for $j = 0, 1, \ldots$

$$W_{j+1} = f(W_j) \cap Q.$$

This allows us to state the convergence result for the continuation method, Algorithm 3.2.1:

Proposition 3.2.2 ([23]) *The sets $C_j^{(k)}$ are coverings of W_j for all $j, k = 0, 1, \ldots$. Moreover, for fixed j, $C_j^{(k)}$ converges to W_j in Hausdorff distance if the number k of subdivision steps in the initialization goes to infinity.*

We close this section by remarking that the convergence result does not require the existence of a hyperbolic structure along the unstable manifold. However, if hyperbolicity can be assumed we additionally obtain results on the speed of convergence [24, 64].

Example 3.2.3 (The Hénon map) We come back to the Hénon map (Example 3.1.3) and illustrate the continuation method (Algorithm 3.2.1). We approximate the unstable manifold of the saddle point at $(0.6314, 0.1894)$. For this we insert a box on depth 14 containing the fixed point. Figure 3.3 shows this box (black) as well as the result after 4, 8, and 13 steps of the continuation algorithm on depth 14. After 13 steps no more boxes are added.

3.3 Extensions to Non-Autonomous Systems

Continuation Algorithm We briefly review the results of a set oriented approach for the computation of pullback attractors. For details we refer, in particular, to [8, 7, 67, 104] and references therein. Let $\dot{x} = f(t, x)$, $x \in \mathbb{R}^l$, $t \in \mathbb{R}$, with evolution $\varphi^{t,s}$ given for all $s, t \in \mathbb{R}$. Let the cocycle $\{\varphi^{t,s}\}$ define a non-autonomous dynamical system on $\mathbb{R}^l$. Then we obtain the corresponding box-valued non-autonomous dynamical system:

Definition 3.3.1 (Box - NDS) Let $Q \subset \mathbb{R}^l$ be a compact set and suppose that $\mathcal{B} = \{B_1, \ldots, B_n\}$ is a partition of Q. Choosing a positive step-size $T \in \mathbb{R}$ we

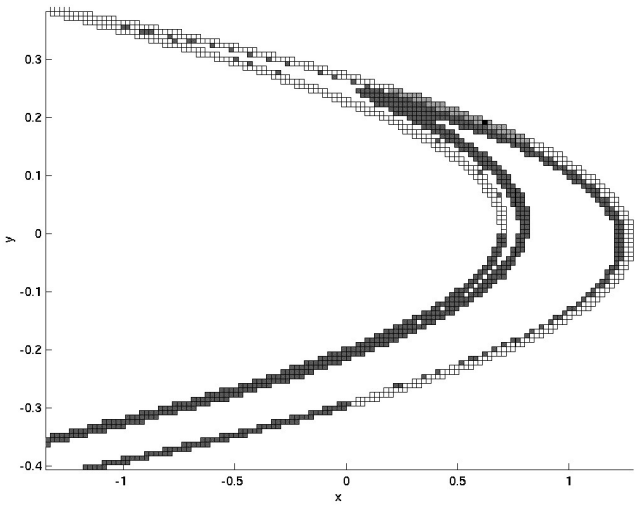

Figure 3.3: Coverings of the unstable manifold of the saddle point at $(0.6314, 0.1894)$ for the Hénon map. Shown are the initial box containing the fixed point (black) and box collections obtained after 4, 8, and 13 steps in the continuation algorithm.

define

$$\begin{aligned}\hat{\varphi}(0,\tau)B_I &= B_I,\ I \subset \{1,\dots,n\} \text{ for all } \tau,\\ \hat{\varphi}(1,\tau)B_I &= B_J,\ \text{where } J := \{j \in \{1,\dots,n\} : \varphi^{\tau+T,\tau}B_I \cap B_j \neq \emptyset\},\end{aligned}$$

and then continue recursively for all $k \geq 2$

$$\hat{\varphi}(k,\tau)B_I := \hat{\varphi}(1,\tau+(k-1)\cdot T)(\hat{\varphi}(k-1,\tau)B_I).$$

This is called the **box-valued non-autonomous dynamical system (box-NDS)** associated with the evolution $\varphi^{t,s}$ and $Q, \mathcal{B}, T$.

Lemma 3.3.2 *The box-NDS has the following characteristics:*

$$Q \cap \varphi^{\tau+T,\tau}B_I \subset \hat{\varphi}(1,\tau)B_I$$

and

$$d(\hat{\varphi}(1,\tau)B_I, Q \cap \varphi^{\tau+T,\tau}B_I) \leq \operatorname{diam}\mathcal{B},$$

where d denotes the Hausdorff semi-distance.

We now want to state a continuation algorithm for the approximation of the pullback attractor A.

Algorithm 3.3.3 In order to calculate the fiber $A(\tau + k \cdot T) \cap Q$ for some $\tau \in \mathbb{R}$ and $k \in \{0, \dots k_1\}$ choose an initial value $k_0 < 0$ in $\mathbb{Z}$. We start with a partition $\mathcal{B}$ of Q and denote the set of boxes by $B_{I_{k_0}}$ with $\cup_{B \in B_{I_{k_0}}} B = Q$. The approximation of the sets $A(\tau + k \cdot T) \cap Q$ by means of box coverings B_{I_k} is as follows:

1. Starting steps: For $k = k_0, ..., -1$ calculate

$$B_{I_{k+1}} = \hat{\varphi}(1, \tau + k \cdot T) B_{I_k} = \hat{\varphi}(k - k_0 + 1, \tau + k_0 \cdot T) B_{I_{k_0}}.$$

2. Continuation steps: For $k = 0, ..., k_1 - 1$ calculate

$$B_{I_{k+1}} = \hat{\varphi}(1, \tau + k \cdot T) B_{I_k} = \hat{\varphi}(k - k_0 + 1, \tau + k_0 \cdot T) B_{I_{k_0}}.$$

Aulbach et al. [7] (see also [104]) show that for any accuracy $\varepsilon > 0$ there is $\kappa \in \mathbb{N}$ and a box size $\operatorname{diam} \mathcal{B} = \delta > 0$, such that for all $k \geq \kappa$

$$d(\hat{\varphi}(k, \tau - k \cdot T) Q, Q \cap A(\tau)) < \varepsilon.$$

If the main box Q and step size T are chosen sufficiently large, then this convergence is even true in the Hausdorff distance [7, 104]. Aulbach et al. [7] also propose a subdivision algorithm generalizing the continuation algorithm. Here, in the first few starting steps the box covering is successively refined and continued. Convergence for this algorithm is also shown in [7].

Note that the numerical scheme for the approximation of the evolution can be interpreted as a non-autonomous difference equation. Cheban, Kloeden, and Schmalfuß [15] analyzed a non-autonomous quasilinear differential equation and the respective difference equation generated by a one-step explicit numerical scheme. They showed that the difference equation had a numerical pullback attractor close to that of the original system. This result is important as we are usually restricted to the consideration of the numerical pullback attractor.

Remark 3.3.4 The continuation algorithm above can be altered in cases where a covering of a fiber $A(\tau)$ of the pullback attractor is given. Then one can approximate $A(\tau + k \cdot T)$ for all $k > 0$ by just employing the continuation step in the algorithm. The convergence follows from the invariance of the pullback attractor A and from the results above.

The continuation of non-autonomous invariant manifolds will be addressed in Chapter 5.

Chapter 4

Expansion Rate Approach for Autonomous Systems

4.1 Introduction

In classical dynamical systems theory invariant manifolds are known to form the geometrical skeleton of the dynamics. In the context of transport theory they serve as boundaries between regions of interest and can explain transport phenomena in terms of lobe dynamics [91, 110]. Also, almost invariant sets can be bounded by stable and unstable manifolds of hyperbolic periodic points of the underlying dynamical system [28].

In the last two decades many different numerical methods for the approximation of invariant manifolds of hyperbolic fixed points of diffeomorphisms $f : X \to X$ or vector fields have been developed. Most of the methods start with a linear approximation of the local stable or unstable manifold and evolve the global manifold via a continuation scheme. In order to carry out the computation, the fixed point as well as its stable and unstable eigenspaces need to be known. However, especially in view of applications in non-autonomous dynamical systems, there is an increasing need for the development of methods for the numerical detection and extraction of invariant manifold candidates when we have little or even no *a priori* knowledge of the geometry of the dynamical system $f : X \to X$.

In Example 2.1.16 on the Duffing System, we have seen that the stable manifold of the hyperbolic saddle point at the origin is characterized by a positive dominant Lyapunov exponent. All other trajectories have a negative, or, in the undamped case, zero dominant Lyapunov exponent. This is the motivation for investigating the relationship between the stable manifold of hyperbolic periodic points and the associated Lyapunov exponent.

In numerical analysis one is restricted to dealing with finite approximations of

these asymptotic quantities. Therefore, we use the expansion rate - a finite-time Lyapunov exponent - as already stated in Definition 2.1.12. We will see that in a typical setting, even for a relatively small number of iterations of the map f, parts of the stable manifold of hyperbolic fixed or periodic points appear as relative local maxima (ridges) of the scalar field induced by the expansion rate distribution. This relationship has already been observed and used in [35, 46, 47, 74]. Additionally, we define the direct expansion rate, which does not need the Jacobian but approximates the dominant finite-time Lyapunov exponent via a finite difference quotient. This method is similar in spirit to the different relative dispersion approaches [12, 61, 108, 113] in the context of the numerical analysis of geophysical fluid flows.

In the following section we will investigate the relationship between stable manifolds, which are geometric structures, and the finite-time Lyapunov exponent, which is a statistic quantity, in the necessary theoretical depth. We then propose a set oriented numerical algorithm in order to obtain a robust approximation of the scalar expansion rate field in two or more dimensions. Strategies for the choice of test points are addressed as well as the optimal number of iterations, which is necessary to make the structures under consideration visible.

The theoretical and numerical results provide the natural framework for a subdivision scheme to numerically extract those objects characterized by large (direct) expansion rates. We state different algorithms and prove convergence. The numerical tools are applied to some test problems. Notably we extract two-dimensional stable manifolds of hyperbolic periodic orbits as well as elliptic regions in the ABC flow. This shows the capability of our methods to deal with higher dimensional systems. Most of the results and methods introduced in this chapter will also be used for the analysis of non-autonomous dynamical systems in Chapter 5. Relevant applications in the context of ocean dynamics are then investigated in Chapter 6.

We close this chapter by developing a few heuristic measures for the analysis of graphs obtained by an appropriate discretization of a dynamical system. In Dellnitz, Junge, Koon et al. [28] almost invariant sets have been approximated using graph algorithms. Moreover, in the example considered, the boundaries between these sets have striking similarities with the invariant manifolds of hyperbolic periodic points. Motivated by the expansion rate approach we derive several heuristics for expansion in graphs and test them in two examples.

4.2 Theoretical Results

4.2.1 Expansion Rates

As described above we want to use the concept of Lyapunov exponents in order to identify certain structures of interest in our dynamical system. In practice, we usually cannot - and do not want to - compute the limit for $n \to \infty$.

Therefore, we use the **expansion rates** of the form

$$\Lambda(N, x_0) = \frac{1}{N} \log |\prod_{n=0}^{N-1} Df(x_n)|, \qquad N \in \mathbb{N}.$$

Unlike Lyapunov exponents, these finite-time Lyapunov exponents have the nice property that they are continuous in phase space for fixed N. Hence for $\varepsilon > 0$ there is $\delta > 0$ such that $|\Lambda(N, x_0) - \Lambda(N, x_1)| < \varepsilon$ for all $|x_0 - x_1| < \delta$.

However, here are no general results for the size of δ in terms of N. If $\lambda(x) = \lambda(y)$ for all x, y in a bounded region (i.e. x, y belong to the same basin of attraction), then the permissable value of δ increases for larger N. If x lies on the stable manifold of some hyperbolic fixed point then for increasing N, δ is decreasing because initial conditions slightly off the manifold tend to another limiting value. However, in this case, for values restricted to the manifold the δ-interval is increasing. That is, for every $\varepsilon > 0$ one finds a not only some $\delta > 0$ such that for all $y \in X$ with $|x - y| < \delta$ it follows that $|\Lambda(N, x) - \Lambda(N, y)| < \varepsilon$. Further, for some non-uniform neighborhood $V(x)$ with $U_\delta(x) \subset V(x)$ it follows that $|\Lambda(N, x) - \Lambda(N, y)| < \varepsilon$ for all $y \in V(x)$. Here $U_\delta(x)$ denotes a ball around x with radius δ.

4.2.2 Expansion Rates and Stable Manifolds

We now derive some results on the relation between local maxima in the scalar expansion rate field and the stable manifolds of hyperbolic periodic points. The following lemma sums up the results presented in Chapter 2:

Lemma 4.2.1 *Let $\bar{x}$ be a hyperbolic fixed point of the dynamical system $f : X \to X$ and let $Q \subset X$ be a compact subset containing $\bar{x}$. Then for every $\varepsilon > 0$ there is $N \in \mathbb{N}$ such that $|\Lambda(n, x) - \lambda(\bar{x})| < \varepsilon$ for all $n > N$ and all $x \in W^s(\bar{x}) \cap Q$.*

Proof: The lemma follows from the fact that the Lyapunov exponent of an orbit is determined by its ω-limit set and the convergence of the expansion rate to the dominant Lyapunov exponent for $N \to \infty$. □

This means that for sufficiently large N, the stable manifold of a hyperbolic fixed point $\bar{x}$ is characterized by a positive expansion rate in the order of magnitude of $\lambda(\bar{x})$.

To have a positive expansion rate for all $N \in \mathbb{N}$ is characteristic for the local stable manifold. To show this let us first define the concept of λ-expansion:

Definition 4.2.2 (λ-expansive set) Let $f : X \to X$ be a diffeomorphism on a compact subset $X \subset \mathbb{R}^l$. We call $x \in X$ **λ-expansive** if there is a constant $\lambda > 0$ such that

$$\Lambda(n, x) = \frac{1}{n} \log |Df^n(x)| \geq \lambda \qquad \forall n \in \mathbb{N}.$$

A set $A_\lambda \subset X$ is called λ-expansive if all points $x \in A_\lambda$ are λ-expansive. We call $x \in X$ **(λ, N)-expansive** if $\Lambda(n, x) \geq \lambda$ for all $n \geq N \in \mathbb{N}$. A (λ, N)-expansive set is denoted by $A_{(\lambda,N)}$. Let

$$C_{(\lambda,n)} := \{x \in X : \Lambda(n, x) \geq \lambda\}.$$

Then

$$A_\lambda = \bigcap_{n \in \mathbb{N}} C_{(\lambda,n)}$$

and

$$A_{(\lambda,N)} = \bigcap_{n \geq N} C_{(\lambda,n)}.$$

Observe that, for some arbitrary $N \in \mathbb{N}$, $C_{(\lambda,N)}$ is a superset of $A_{(\lambda,N)}$. We will need this in the numerical discussion. Notably all sets defined above are compact.

We now prove the following lemma on the local stable manifold of $\bar{x}$:

Lemma 4.2.3 *Let $\bar{x} = f(\bar{x})$ be a hyperbolic fixed point. Then for every $\delta > 0$ and $\lambda = \lambda(\bar{x}) - \delta$, there is $\varepsilon > 0$ such that $W^s_\varepsilon(\bar{x})$ is λ-expansive.*

Proof: Show that $\bar{x}$ is λ-expansive:

$$\frac{1}{n} \log |Df^n(\bar{x})| \geq \lambda(\bar{x}) \qquad \forall n \in \mathbb{N}$$

$$\Rightarrow \frac{1}{n} \log |Df^n(\bar{x})| > \lambda(\bar{x}) - \delta = \lambda \qquad \forall n$$

and

$$\lim_{n \to \infty} \frac{1}{n} \log |Df^n(\bar{x})| = \lambda(x).$$

As $\frac{1}{n} \log |Df^n(\bar{x})| > \lambda \; \forall n$ and $\frac{1}{n} \log |Df^n(x)|$ depends continuously on x for fixed n, for each n we find a (possibly non-uniform) neighborhood $V_n(\bar{x})$ of $\bar{x}$ such that

$$\frac{1}{n} \log |Df^n(x)| > \lambda \qquad \forall x \in V_n(\bar{x}).$$

Consider

$$U_\infty = \bigcap_{n\geq 0} V_n(\bar{x}),$$

which is a λ-expansive set of points. It is non-empty as $\bar{x} \in U_\infty$. From the continuous dependence of $\frac{1}{n}\log|Df^n(x)|$ on x on the one hand, and from

$$\lim_{n\to\infty} \frac{1}{n}\log|Df^n(x)| = \lambda(x) > \lambda, \quad \forall\, x \in W^s(\bar{x})$$

on the other hand, we find $\varepsilon > 0$ such that $W^s_\varepsilon \subset U_\infty$. This concludes the proof. □

We can also re-formulate Lemma 4.2.1 in the context of λ-expansion:

Lemma 4.2.4 *Let $Q \subset \mathbb{R}^l$ be a compact set and $\bar{x} \in Q$ be a hyperbolic fixed point with $\lambda(\bar{x})$. Then for every $\delta > 0$ there is $N > 0$ such that $W^s(\bar{x}) \cap Q$ is (λ, N)-expansive with $\lambda := \lambda(\bar{x}) - \delta$.*

We remark that all these properties are necessary but not sufficient to characterize the stable manifold of a saddle point. However, in some simple cases one can show that λ-expansion or (λ, N)-expansion is also sufficient.

Theorem 4.2.5 *Let $\dot{x} = f(x)$, $x \in X \subset \mathbb{R}^2$, be structurally stable, $f(x_0) \neq 0$ and $\gamma := \phi^t(x_0)$ a bounded, non-periodic orbit. If x_0 is λ-expansive or (λ, N)-expansive, then it belongs to the stable manifold of a hyperbolic fixed point.*

Proof: This follows from a combination of the statements in the Poincaré-Bendixson Theorem and Peixoto's Theorem ([111], Thms. 9.0.6 and 12.1.4). Peixoto's Theorem says that the dynamical system $\dot{x} = f(x)$, $x \in X \subset \mathbb{R}^2$ is structurally stable if and only if (1) the number of fixed points and periodic orbits is finite, (2) they are all hyperbolic, (3) there are no orbits that connect saddle points, and (4) the nonwandering set consists of fixed points and periodic orbits. The Poincaré-Bendixson Theorem says that the ω-limit set of a point x_0 on a bounded orbit is either a fixed point, a periodic orbit or a finite number of saddle points and their connecting orbits. As the system is structurally stable, there are no such connections. Stable and asymptotically stable periodic orbits, as well as stable or asymptotically stable fixed points and orbits converging to them, are also ruled out, because they cannot be (λ, N)-expansive. Unstable periodic orbits are not permitted as we require x_0 not to be on a periodic orbit. So the above statement follows. □

On the other hand, if we look at systems that are not structurally stable at all, namely two-dimensional (or one-degree of freedom) Hamiltonian systems, the concept of λ-expansion is also sufficient:

Theorem 4.2.6 *Let $\dot{x} = f(x)$, $x \in X \subset \mathbb{R}^2$, be a Hamiltonian dynamical system with a hyperbolic fixed point $\bar{x}$ with Lyapunov exponent $\lambda(\bar{x})$. Then there is $0 < \lambda \leq \lambda(\bar{x})$ such that if x_0 is λ-expansive or (λ, N)-expansive, then $x_0 = \bar{x}$ or it is contained in its stable manifold.*

Proof: In a one-degree of freedom Hamiltonian system the two Lyapunov exponents with respect to an orbit add up to zero. However, for every $x_0 \in X$, unless $\omega(x_0)$ is a hyperbolic fixed point, both Lyapunov exponents have zero real part. So only the stable manifold of a hyperbolic fixed point can contain a λ-expansive set for $\lambda > 0$. □

For general dynamical systems one obtains the following result when the hyperbolic fixed point under consideration is the most unstable hyperbolic orbit:

Lemma 4.2.7 *Suppose that there is a hyperbolic fixed point $\bar{x} \in Q$, where $Q \subset X$ is a compact set, and $\delta > 0$ such that $\lambda(\bar{x}) > \lambda(x) + \delta$ for all $x \in Q \setminus W^s(\bar{x})$. Then there is $\lambda > 0$ such that $A_\lambda \cap Q \subset W^s(\bar{x}) \cap Q$.*

Proof: Choose $\lambda = \lambda(\bar{x}) - \frac{\delta}{2}$. Then $A_\lambda \cap Q \neq \emptyset$ as $\bar{x} \in A_\lambda \cap Q$. Let $x \in Q \setminus W^s(\bar{x})$. Then there is $N_0 \in \mathbb{N}$ such that $\left|\Lambda(n, x) - \lambda(x)\right| < \frac{\delta}{2}$ for all $n \geq N_0$. Hence $\Lambda(n, x) < \lambda$ for all $n \geq N_0$ and, consequently, $x \notin A_\lambda \cap Q$. This gives the desired statement. □

If one considers the (λ, N)-expansive set $A_{(\lambda,N)}$ for some $N > 1$ one typically finds a larger part of $W^s(\bar{x}) \cap Q$.

Another consequence of this lemma is that one can use λ as a filter; analyzing the λ-expansive sets for increasing λ gives a nested sequence of expansive sets often corresponding to a hierarchy of stable manifolds of hyperbolic periodic points.

Remarks 4.2.8

1. The concept of λ-expansion is related to uniform hyperbolicity. Note however, that for this we need exponential growth *normal* to the orbit/manifold under consideration, which we do not restrict ourselves to in our setting. Here all kinds of stretching are detected.

2. The result above also applies to periodic points if one considers f^p for some $p > 1$.

For the sake of completeness we note that unlike in usual optimization problems, we do not just need to look at local or global maxima but strictly speaking at relative local maxima of the expansion rate field in order to detect stable manifolds. These so-called ridges are characterized by demanding that they are strict

maxima of a scalar field only in directions normal to the structure under consideration. This concept is discussed in detail in Shadden, Lekien, and Marsden [102].

However, as noted by Haller [47] the invariant manifolds identified in a finite-time context are not unique but only given up to exponentially small errors. Hence, also a small strip along the stable manifold is characterized by large expansion rates, which complicates the numerical extraction of the manifold. However, in typical examples it is not necessary to look for ridges specifically. Therefore we will not proceed with this concept any further.

4.2.3 Direct Expansion Rates

So far we have only considered infinitesimal perturbations. Often, one is interested in finite perturbations because they are realistic in many applications. Moreover, in some cases $Df(x)$ is not given analytically as we will see in the following chapter in the context of finite-time velocity fields. Here f may be given only in terms of measurement data or a finite set of data points approximating the solution to a partial differential equation. In this case, $Df(x)$ can usually be obtained via local interpolation of the given discrete velocity field. However, as well as interpolation errors, this means additional computational expense. Therefore it is desirable to get an approximation of $\Lambda(N, x)$ on the basis of f.

Definition 4.2.9 (Direct expansion rate) Let $\varepsilon > 0$ and $N \in \mathbb{N}$. The **direct expansion rate** is given by

$$\Lambda_\varepsilon(N, x_0) := \frac{1}{N} \log \left(\max_{\{x : |x_0 - x| = \varepsilon\}} \frac{|f^N(x_0) - f^N(x)|}{\varepsilon} \right).$$

Direct expansion rates are quantities that are similar in spirit to the concept of relative dispersion, see for example [12, 61, 108, 113].

The connection between expansion rates and direct expansion rates is given in the following proposition.

Proposition 4.2.10 *Let $f : X \to X$ be a diffeomorphism on a compact subset $X \subset \mathbb{R}^l$. Then*

$$\lim_{\varepsilon \to 0} \Lambda_\varepsilon(N, x_0) = \Lambda(N, x_0).$$

Proof: Let $N \in \mathbb{N}$ be fixed. As f is a diffeomorphism, $f^N(x_0)$ is continuously differentiable with respect to x_0. Therefore we have

$$\lim_{x \to x_0} \left(\frac{f^N(x_0) - f^N(x)}{|x_0 - x|} - \frac{Df^N(x_0) \cdot (x_0 - x)}{|x_0 - x|} \right) = 0.$$

It follows that

$$\begin{aligned}
\lim_{\varepsilon\to 0}\max_{\{x:|x_0-x|=\varepsilon\}}\frac{|f^N(x_0)-f^N(x)|}{|x_0-x|} &= \lim_{\varepsilon\to 0}\max_{\{x:|x_0-x|=\varepsilon\}}\frac{|Df^N(x_0)\cdot(x_0-x)|}{|x_0-x|}\\
&= \lim_{\varepsilon\to 0}\max_{\{\gamma:|\gamma|=\varepsilon\}}\frac{|Df^N(x_0)\gamma|}{\varepsilon}\\
&= \lim_{\varepsilon\to 0}\max_{\{\xi:|\xi|=1\}}\frac{|Df^N(x_0)\xi\cdot\varepsilon|}{\varepsilon}\\
&= \max_{\{\xi:|\xi|=1\}}|Df^N(x_0)\xi|\\
&= |Df^N(x_0)|.
\end{aligned}$$

Using the definitions of $\Lambda_\varepsilon(N,x_0)$ and $\Lambda(N,x_0)$ we can conclude

$$\lim_{\varepsilon\to 0}\frac{1}{N}\log\left(\max_{\{x:|x_0-x|=\varepsilon\}}\frac{|f^N(x_0)-f^N(x)|}{\varepsilon}\right)=\frac{1}{N}\log|Df^N(x_0)|,$$

thus, $\lim_{\varepsilon\to 0}\Lambda_\varepsilon(N,x_0)=\Lambda(N,x_0)$. □

For ε small enough, the relation between local maxima in the direct expansion rates field and stable manifolds of hyperbolic points can be drawn via the argument for expansion rates. However, even without these arguments, one can demonstrate that the maximization property is typical.

For example, suppose the simple case that the stable manifold of a hyperbolic fixed point is a separatrix serving as the basin boundary between two domains of attraction of two attracting sets. Then two points initialized on different sides of the stable manifold have a totally different fate, see Figure 4.1. On the other hand, two points both initialized on one side belong to the same basin of attraction. In such cases the stable manifold is expected maximize the direct expansion rate.

More generally, we can consider the Lambda-Lemma 2.1.3. This states that a disk or curve segment initialized transverse to the stable manifold of a hyperbolic fixed point will align along the unstable manifold and comes arbitrarily close to it, see also Figure 2.1. Points on or near the (local) unstable manifold are repelled from the fixed point at an exponential rate. If pairs of points are initialized properly, they move along different branches of the manifold. This high stretching is exactly what the direct expansion rate measures.

4.2.4 Error Estimates

We now want to estimate the error that is made when substituting the expansion rate by the direct expansion rate. Let $f : X \to X$, $X \subset \mathbb{R}^l$, be a C^r-diffeomorphism with $r \geq 2$. Suppose we are given a finite initial perturbation ε_0

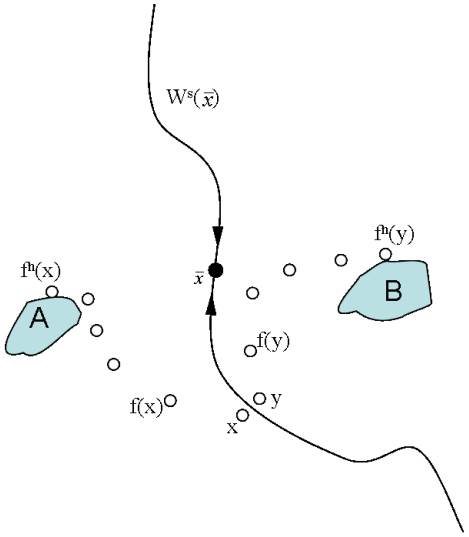

Figure 4.1: In many cases the stable manifold of a hyperbolic fixed point serves as a boundary between dynamically distinct regions or even separates different basins of attraction. Hence two points straddling the manifold have a completely different fate, which causes a large direct expansion rate.

in x_0, with $x_0, x_0 + \varepsilon_0$ as well as their connecting line contained in $\overset{\circ}{X}$, which is the set of inner points in X. After one iteration we have

$$\varepsilon_1 := f(x_0 + \varepsilon_0) - f(x_0) = Df(x_0) \cdot \varepsilon_0 + r_0,$$

with $r_k := r(x_k, \varepsilon_k)$, $k \in \mathbb{N}$, where ([53] p.284, Thm. 168.4)

$$r_0^{(j)} = \sum_{i,k=1}^{l} \left(\int_0^1 \frac{\partial^2 f_j}{\partial x_i \partial x_k}(x_0 + t\varepsilon_0)(1-t)dt \right) \varepsilon_0^{(i)} \varepsilon_0^{(k)}.$$

Here the superscript (j) denotes the j-th component. If the partial derivatives of second order of the components $f_1, \ldots, f_l$ are bounded in X, then

$$\|r_0\|_\infty \leq \frac{1}{2} M \|\varepsilon_0\|_\infty^2 \text{ with } M := \max_j \sum_{i,k=1}^{l} \sup_{x \in Q} \left| \frac{\partial^2 f_j}{\partial x_i \partial x_k}(x) \right|.$$

The error for further iterates evolves according to

$$\begin{aligned} \varepsilon_N &= f(x_{N-1} + \varepsilon_{N-1}) - f(x_{N-1}) \\ &= Df^N(x_0)\varepsilon_0 + \sum_{j=1}^{N-1} Df^{N-j}(f^j(x_0)) r_{j-1} + r_{N-1}. \end{aligned}$$

We assume that $|Df^j(x)| \leq \lambda^j$ for some $\lambda > 0$. This gives

$$\begin{aligned} |\varepsilon_N| &\leq |Df^N(x_0)\varepsilon_0| + \sum_{j=1}^{N-1} |Df^{N-j}(f^j(x_0))| \cdot |r_{j-1}| + |r_{N-1}| \\ &\leq \lambda^N \cdot |\varepsilon_0| + \sum_{j=1}^{N-1} \lambda^{N-j} \cdot |r_{j-1}| + |r_{N-1}|. \end{aligned}$$

With $\|\cdot\|_\infty \leq |\cdot| \leq \sqrt{l}\|\cdot\|_\infty$ we obtain

$$|r_j| \leq \tilde{M}|\varepsilon_j|^2,$$

where $\tilde{M} = \frac{1}{2}\sqrt{l} \cdot M$. Set

$$R := \max_{j\in\{0,\ldots,N-1\}} |r_j|.$$

It follows that

$$\begin{aligned} |\varepsilon_N| &\leq \lambda^N \cdot |\varepsilon_0| + R\sum_{j=1}^{N-1} \lambda^{N-j} + R \\ &= \lambda^N \cdot |\varepsilon_0| + R\sum_{j=0}^{N-1} \lambda^j. \end{aligned}$$

Hence, for $\lambda \neq 1$ we obtain

$$\frac{|\varepsilon_N|}{|\varepsilon_0|} \leq \lambda^N + \frac{R}{|\varepsilon_0|} \cdot \frac{\lambda^N - 1}{\lambda - 1}. \tag{4.1}$$

When $\lambda < 1$, that is, in the case where we have contraction, we can assume that $R = C|\varepsilon_0|^2$, for some $C > 0$. Then Equation (4.1) simplifies to

$$\frac{|\varepsilon_N|}{|\varepsilon_0|} \leq \lambda^N + C|\varepsilon_0| \cdot \frac{\lambda^N - 1}{\lambda - 1} \leq \lambda^N + C|\varepsilon_0| \cdot \frac{1}{1-\lambda}.$$

On the other hand, if $\lambda > 1$, that is, in the expansive case, the error estimate (4.1) can be written as

$$\frac{|\varepsilon_N|}{|\varepsilon_0|} \leq \lambda^N + \mathcal{O}(\lambda^{N-1}),$$

hence, one obtains a very pessimistic result. Therefore, we can conclude that in the case where $\lambda > 1$, for large N, direct expansion rates will typically not approximate finite-time Lyapunov exponents. They must be seen merely as a qualitative indicator of stretching, measuring global effects of the full nonlinear dynamical system, see for example [61]. However, as pointed out in [113], due to the typically rapid alignment of the initial perturbation with the most unstable direction associated with the trajectory, this error growth usually does not affect the qualitative results.

4.3 Approximation of Expansion Rates

In this section, we propose an algorithm for the numerical approximation of expansion and direct expansion rate fields in a set oriented approach. We define the (direct) expansion rate of a box B as the maximum (direct) expansion rate over all $x \in B$, introduce some strategies for its approximation and show convergence properties. Other topics like optimal choice of integration steps, choice of test points, implementation and parallel computing are also addressed. We point out relations and differences to the relative dispersion approach [12, 61, 108, 113] and the direct Lyapunov exponent approach in [46, 47, 74, 102].

4.3.1 Set Wise Expansion Rates

Suppose we are given a box collection $\mathcal{B}_k$ that is a covering of our region of interest (e.g. attractor, chain recurrent set, compact set in phase space). We then define the expansion rate for a box $B \in \mathcal{B}_k$ as

$$\delta(N, B) := \max_{x_0 \in B} \Lambda(N, x_0)$$

and in an analogous way the direct expansion rate for B as

$$\delta_\varepsilon(N, B) := \max_{x_0 \in B} \Lambda_\varepsilon(N, x_0).$$

Proposition 4.3.1 *Let $B \in \mathcal{B}_k$ be given. Then*

$$\Lambda_{(\varepsilon)}(N, x) \leq \delta_{(\varepsilon)}(N, B) \qquad \forall x \in B.$$

Moreover, let B_k be a nested sequence of boxes with $B_k \in \mathcal{B}_k$ such that $x \in B_k$ for all k and $\operatorname{diam} B_k = \theta \cdot \operatorname{diam} B_{k-1}$ for $0 < \theta < 1$. It follows that

$$\lim_{k \to \infty} \delta_{(\varepsilon)}(N, B_k) \to \Lambda_{(\varepsilon)}(N, x).$$

Proof: The properties directly follow from the continuity of $\Lambda(N, x)$ with respect to x and the fact that we consider the maximum (direct) expansion rate in each box. □

In practice we compute an approximation of $\delta(N, B)$ or $\delta_\varepsilon(N, B)$ using test point strategies in each box. This will be discussed in the following section.

4.3.2 Test Point Strategies

Since in practice the maximum over an infinite number of points cannot be computed, one needs to use a test point discretization in each box. In this section, we discuss several choices of test points for the approximation of set wise (direct) expansion rates.

Expansion rates For the computation of the expansion rate of a box in systems of moderate dimension a good choice is to discretize the box by a regular grid, compute the expansion rates with respect to the grid points and assign their maximum to the box. As the expansion rate is continuously dependent on x for fixed N, the error in employing this discretization can be controlled by a dense enough grid or alternatively by a fine enough box covering. However, as we will see later, in typical examples it is often sufficient to consider only the center point of a box. This is especially true for small numbers of iterations or when dealing with a very fine box discretization. In higher dimensions a grid discretization often does not make much sense because the number of points would increase too much. In this case one can take the maximum expansion rate with respect to a set of equally distributed random points, so-called Monte Carlo points.

Direct expansion rates More problematic is the approximation of the direct expansion rate of a box. Theoretically, this does not only mean that an infinite number of points has to be considered but that for each $x \in B$ infinitely many points on the ε-ball around x need to be dealt with too. In a similar context, Bowman [12] uses a staggered grid of initial conditions and measures the stretching associated with segments defined by neighboring pairs of points in the grid and considers the maximum for each grid point. Winkler [113] chooses the four neighbors of a grid point in a two-dimensional grid and considers the squared relative dispersion, whereas von Hardenberg et al. [108] even consider eight satellites of a grid point.

All these approaches have in common that they depend on a grid discretization of phase space and hence they can only be used in systems with moderate dimensions (i.e. two- or three-dimensional space). Moreover, in order to increase the accuracy of the computations by decreasing the initial perturbation ε the complete mesh needs to be refined, which causes additional computational load.

In order to approximate the maximum direct expansion rate of a box B in an arbitrary dynamical system, we seek to have a formulation that is independent of the dimension of the phase space. Therefore, the maximum two-point relative dispersion of pairs of Monte Carlo points seems to be an appropriate approximation of the direct expansion rate of a box. This means that for the approximation of $\delta_\varepsilon(N, B)$ the following approach has been implemented:

In $B \in \mathcal{B}_k$ we choose m equally distributed points x_i. Moreover, we randomly assign to every point a vector $v_i \in \{w \in \mathbb{R}^l : \ ||w|| = \varepsilon\}$ with $\{v_1, ..., v_m\}$ again being equally distributed in such a way that for $m \to \infty$ the v_i lie dense on the boundary of a ball of radius ε about the origin. With $y_i = x_i + v_i$ we get m pairs of points (x_i, y_i), $i = 1, ..., m$, separated by a distance ε. See Figure 4.2 for an illustration.

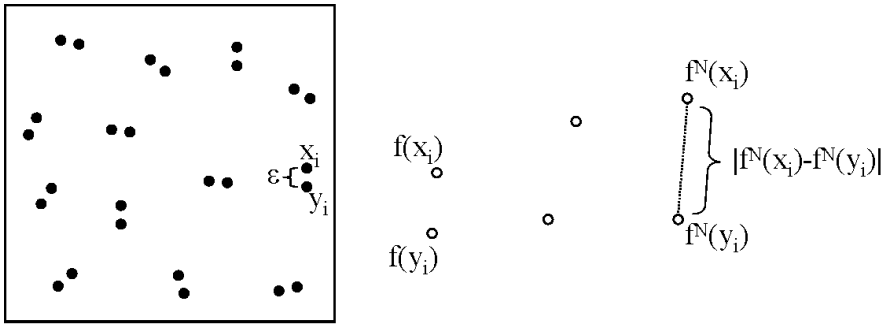

Figure 4.2: Choice of test points in a box and computation of the relative dispersion of a pair of test points.

Let MC be a collection of m point pairs (x_i, y_i) in B constructed as described above. The **approximate direct expansion rate for a set** B with respect to the point pairs MC is given by

$$\delta_{\varepsilon,MC}(N,B) := \frac{1}{N} \log \left(\max_{i\in\{1,\ldots,m\}} \frac{\left|f^N x_i - f^N y_i\right|}{\varepsilon} \right).$$

Proposition 4.3.2 *Let $B \in \mathcal{B}_k$, $x \in B$ and $N \in \mathbb{N}$. Let MC be a collection of m point pairs (x_i, y_i) in B constructed as described above. Then*

$$\delta_{\varepsilon,MC}(N,B) \leq \delta_\varepsilon(N,B).$$

Moreover, let B_k be a nested sequence of boxes with $B_k \in \mathcal{B}_k$ such that $x \in B_k$ for all k and $\operatorname{diam} B_k = \theta \cdot \operatorname{diam} B_{k-1}$ *for $0 < \theta < 1$. It follows that*

$$\lim_{m\to\infty} \lim_{k\to\infty} \delta_{\varepsilon,MC}(N,B_k) \to \Lambda_\varepsilon(N,x),$$

where m is the number of test point pairs.

Note that for almost all initial orientations, the perturbation vector aligns with the most unstable direction [100], so that the method is expected to work satisfactorily even if only a relatively small number of pairs in each box are considered.

Unlike in other approaches we do not need to refine a given grid structure in order to increase the accuracy of the computations. Here one has several independent choices. One possibility is to increase the number of Monte Carlo points in all or only specific boxes, on the other hand the box covering or only certain boxes can be refined. This allows adaptive approaches, where, for example, only boxes with high expansion rates are refined. Furthermore, the accuracy can be increased by decreasing ε. Contrary to the other grid-based approaches described

above, this can be done without increasing the number of points under consideration. Note that using a very small ε is only required if one wants to obtain a good approximation of the expansion rate. Choosing larger values of ε one measures increasingly global stretching rather than local effects.

Before we proceed, we illustrate these methods at the Duffing system introduced in Example 2.1.16 in Chapter 2:

Example 4.3.3 (Duffing system) We choose $\gamma = 0$ and $\delta = 0.25$ in Equation 2.1:

$$\ddot{x} + \delta\dot{x} - x + x^3 = \gamma \cos \omega t.$$

These are the parameter values for which the system is autonomous and has a saddle at the origin and sinks at $(\pm 1, 0)$. We consider a box covering of the rectangle $Q = [-2, 2] \times [-2, 2]$ at depth 12 (4096 boxes). For the direct expansion rate approach we choose 50 pairs of Monte Carlo points per box as described above, with the initial distance being 1% of the box radius, that is $\varepsilon \approx 0.002$. For the computation of expansion rates we use a uniform 5×5 grid per box. We approximate the desired quantities for different numbers of iterations of the time-1 flow map and display the results in Figure 4.3.

As expected, the two approaches give qualitatively consistent results. Moreover, for larger N both methods give increasingly accurate approximations of the stable manifold of the saddle point. Even the quantitative results fit well to the theoretical result of $\lambda = 0.8828$. The absolute differences between the two approaches are shown in Figure 4.4. As discussed above, the errors grow for large N, but nevertheless both methods perform well qualitatively in this example. Note that the direct expansion rates approach gives especially good results for large N. This can be accounted for by the fact that for large N the direct expansion rate tends to measure global effects of the dynamics. Trajectories with respect to points straddling the stable manifold will diverge at the saddle point along different branches of the unstable manifold as indicated by the Lambda-Lemma 2.1.3, and this stretching is what the direct expansion rate takes into account. The expansion rate, on the other hand, depicts local effects, namely the stability of the trajectory.

4.3.3 Choice of Number of Iterations N

As the results of the expansion rates and direct expansion rates computations are dependent on the number of iterations N, a crucial question is how to choose N in order to capture the desired structures. For small N, large regions of the phase space may exhibit similar stretching characteristics, and the invariant manifolds are not discernible, see Figure 4.6 ($N = 1$). If N is allowed to grow too large, however, the final positions of initially neighboring trajectories are generally

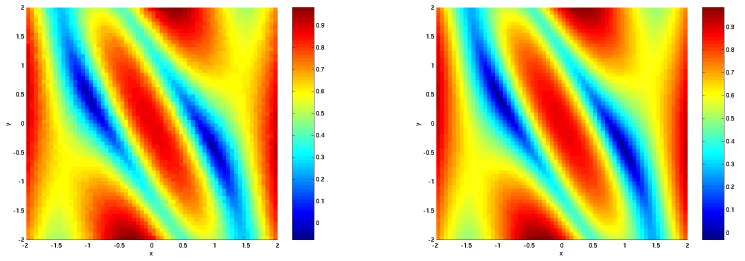

$N = 1$ $N = 1$

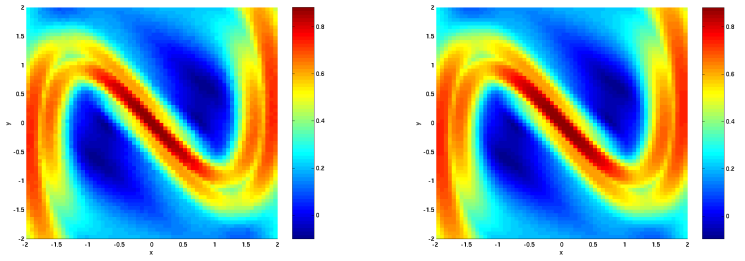

$N = 3$ $N = 3$

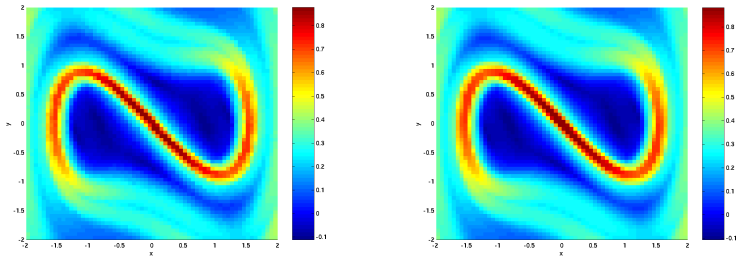

$N = 5$ $N = 5$

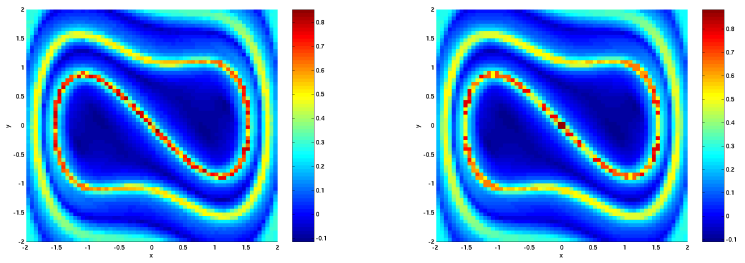

$N = 10$ $N = 10$

Figure 4.3: Direct expansion rate (left column) and expansion rate fields (right column) for the Duffing system for different numbers of iterations of the time-1 map.

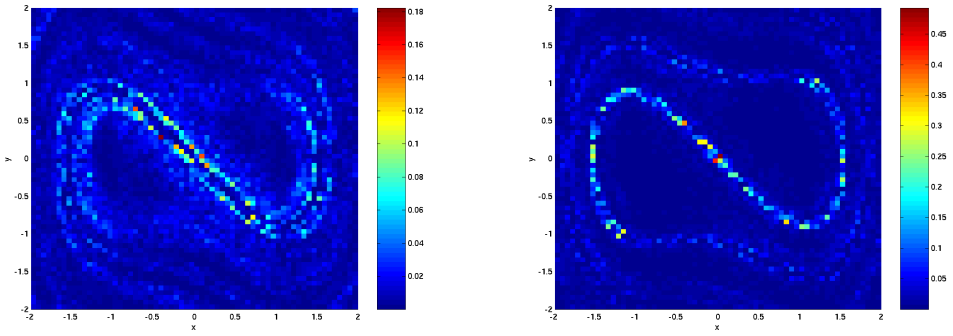

$N = 5$ $N = 10$

Figure 4.4: Absolute difference between direct expansion rate and expansion rate fields.

uncorrelated (see Figure 4.6, $N = 7$), and thus makes the direct expansion rate calculation, in particular, unfaithful. Moreover, as shown in Section 4.2.4, usually for large N the error in the direct expansion rate is hard to control. Furthermore, if, as in our case, the dynamical system lives on a compact set in phase space, then the direct expansion rates for all trajectories will eventually tend to zero. We therefore seek an intermediate number of iterates that is sufficiently long for the interesting structures to emerge, but sufficiently short to avoid the above effects.

Scaling results from turbulence studies provide an approach to determine this optimal number of iterates (see e.g. [9, 10], and especially [113] for a detailed discussion). We will adapt this purely physical interpretation to our specific context. For this let ε_0 denote the initial perturbation in x_0, which evolves according to

$$\varepsilon_N = f(x_{N-1} + \varepsilon_{N-1}) - f(x_{N-1}), \qquad \text{for } N = 1, 2, \ldots.$$

Suppose that the dynamical system is characterized by two different length scales l and L. The small length scale l represents a scale below which the separation ε_N (i.e. $|e_N| \leq l$) grows exponentially:

$$|\varepsilon_N| = |\varepsilon_0| \cdot e^{\lambda N},$$

where $\lambda > 0$.

In contrast, the large length scale L represents the scale of the largest invariant structures in the flow. Trajectories that are separated by this length scale $|e_N| \geq L$ are completely uncorrelated, which gives the so-called diffusive regime, with

$$\langle |\varepsilon_N|^2 \rangle \approx 2DN,$$

where D corresponds to the diffusion coefficient in turbulence and $\langle\cdot\rangle$ denotes an average taken over many particle pairs (e.g. an ensemble average); see, for example, Boffetta et al. [10]. Often the diffusive regime cannot be attained, especially when one considers a compact invariant set. For separations of intermediate length scales one typically expects that one observes behavior that is influenced by both regimes, this is the so-called anomalous regime.

From our point of view, we are most interested in the exponential regime. Thus, a natural threshold for the number of iterations is the time of transition from the exponential to the anomalous regime. This captures the stretching associated with exponential separation of initial conditions without capturing the diffusive behavior.

Hence, for a given dynamical system, we calculate the average direct expansion rates with respect to the given box covering $\mathcal{B}$ by

$$\langle \delta_\varepsilon(N,\cdot)\rangle_{\mathcal{B}} = \frac{1}{\sum_{B\in\mathcal{B}} m(B)} \sum_{B\in\mathcal{B}} m(B)\delta_\varepsilon(N,B). \tag{4.2}$$

The exponential regime may be identified as linear growth of $N\cdot\langle \delta_\varepsilon(N,\cdot)\rangle_{\mathcal{B}}$ versus N. The optimal number of iterates is then indicated as an elbow in the graph, see Figure 4.7.

Note that the results depend on the size of ε and are valid for the direct expansion rates approach only. However, as we will see later, these ideas will nevertheless provide some useful information about an appropriate number of iterates for discerning the relevant structures.

Another option is to consider the average or maximal difference between different expansion rate fields, that is, with respect to different numbers of iterations N. One plots the average difference for two subsequent scalar expansion rate fields (i.e. N and $N+1$). When the difference graph converges to zero, that is the expansion rate field does not change on average, it indicates that an appropriate value for N has been found.

4.3.4 Parallel Computing

As the expansion rates or direct expansion rates are computed per box, so, the computation does not depend on the complete box covering, the algorithm can be easily parallelized. A simple approach is to divide our box covering into several sets of boxes of about the same magnitude and compute the expansion rates for these packages independently on several compute clients. The results are collected on a server and can then be combined to obtain the results for the complete box covering under consideration. For this task we use ParTool [52], a simple parallelization code that enables us to define jobs and provides a communication structure between clients and server.

4.3.5 Examples

The Duffing Oscillator

Once again, we consider the Duffing oscillator (2.1):

$$\ddot{x} + \delta\dot{x} - x + x^3 \;=\; \gamma\cos\omega t,$$

with $\delta = 0.2$, $\gamma = 0.36$, $\omega = 1$. We choose $Q = [-2, 2] \times [-2, 2]$. Because of the periodic forcing we consider a time-2π map and can thus reduce the system to a two-dimensional autonomous map. Numerically, we find a hyperbolic fixed point of the Poincaré map at $\bar{x} \approx (0.04, 0.13)$. Its one-dimensional stable manifold and the well-known Duffing attractor formed by its unstable manifold are shown in Figure 4.5. For the approximation of these structures we used the set oriented continuation algorithm introduced in the previous chapter.

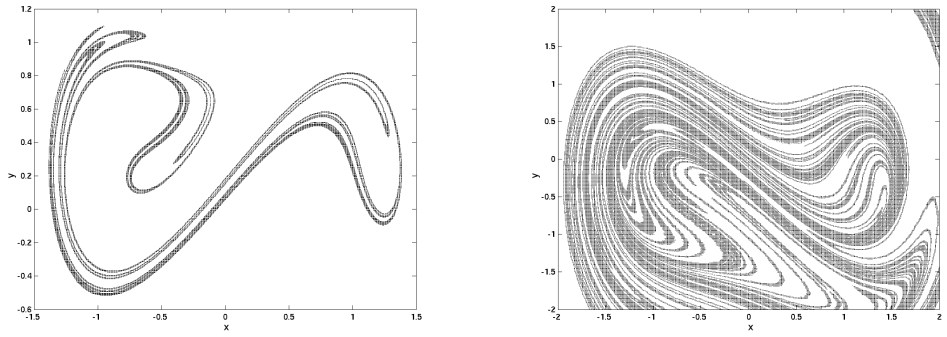

a) b)

Figure 4.5: Invariant manifolds for the Duffing oscillator, approximated using the continuation algorithm. a) Unstable manifold of the hyperbolic fixed point $\bar{x}$, forming the Duffing attractor; b) part of the stable manifold of $\bar{x}$.

In order to decide on an appropriate number of iterates, we consider a partition of Q on depth 12 (4096 boxes). We choose 10 pairs of points per box as described above ($\varepsilon \approx 0.002$) and compute the direct expansion rates for $N = 1, \ldots, 15$ iterates. Some results are shown in Figure 4.6. Note that for large N the results become fuzzy, as expected, but also observe how well they compare to Figure 4.5 b). We plot $N \cdot \langle \delta_\varepsilon(N, \cdot) \rangle_{\mathcal{B}}$ (see Equation (4.2), with $\mathcal{B}$ denoting the box covering) versus N in Figure 4.7. We see that $N = 5$ seems to be an appropriate number of iterations to use for further investigation as it marks the transition to the anomalous regime.

We compute the direct expansion rates for $N = 5$ with respect to finer partitions of the phase space in Figure 4.8, observing that the relation between local

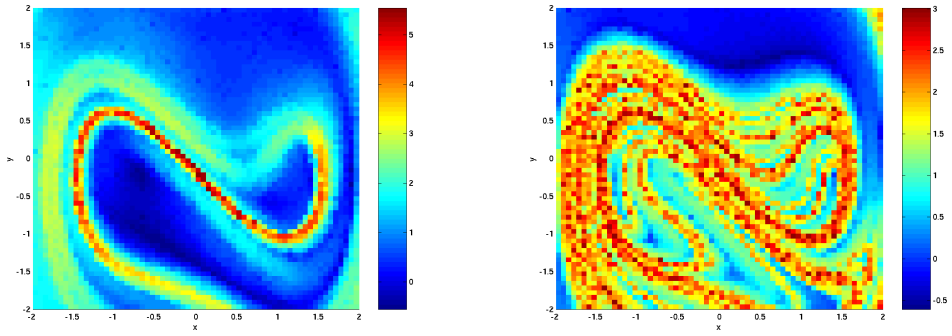

$N = 1$ $N = 3$

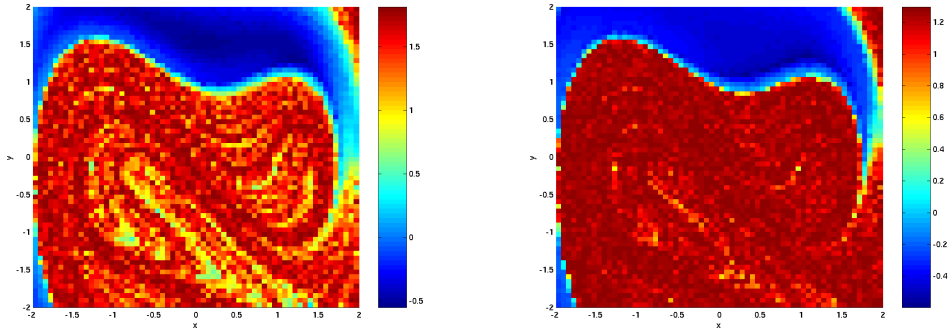

$N = 5$ $N = 7$

Figure 4.6: Direct expansion rate fields for the Duffing oscillator for different numbers of iterations N of the time-2π map.

maxima in the scalar field to the stable manifold of the hyperbolic fixed point becomes even more obvious.

Additionally, expansion rates for orbits in the time reversed system are computed, uncovering the unstable manifold of the hyperbolic fixed point of the Poincaré map. We plot the results for both forward and backward time computations together in Figure 4.9. For this we use a visualization method described in Winkler [113], who analyzed this model for a different set of parameters using the relative dispersion technique.

Hénon Map

We now apply our methods to the Hénon map [51]

$$h(x, y) = (1 + y - ax^2, bx),$$

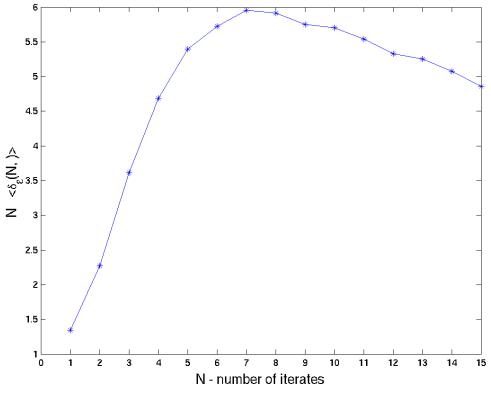

Figure 4.7: Average direct expansion rates for the Duffing oscillator.

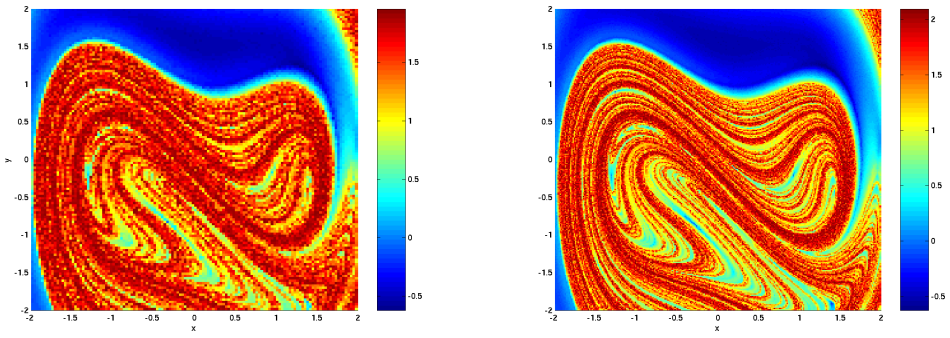

a) b)

Figure 4.8: Direct expansion rates for the Duffing oscillator, $N = 5$ for finer partitions. a) Box covering on depth 14 (16384 boxes); b) box covering on depth 16 (65536 boxes).

with $a = 1.4$ and $b = 0.3$. The Lyapunov exponents of the numerically observed attractor were found to be approximately $\lambda_1 = 0.42$ and $\lambda_2 = -1.62$ [6]. The system has two fixed points (x_1, bx_1) and (x_2, bx_2), where

$$x_{1,2} = \frac{b - 1 \pm \sqrt{(1-b)^2 + 4a}}{2a},$$

one of which is embedded within the attracting set. Its stable manifold bounds the basin of attraction of the attractor [43].

We consider a covering of part of the basin of attraction for the Hénon attractor with $Q = [-1.5, 1.5] \times [-0.4, 0.4]$. Expansion rates with respect to the

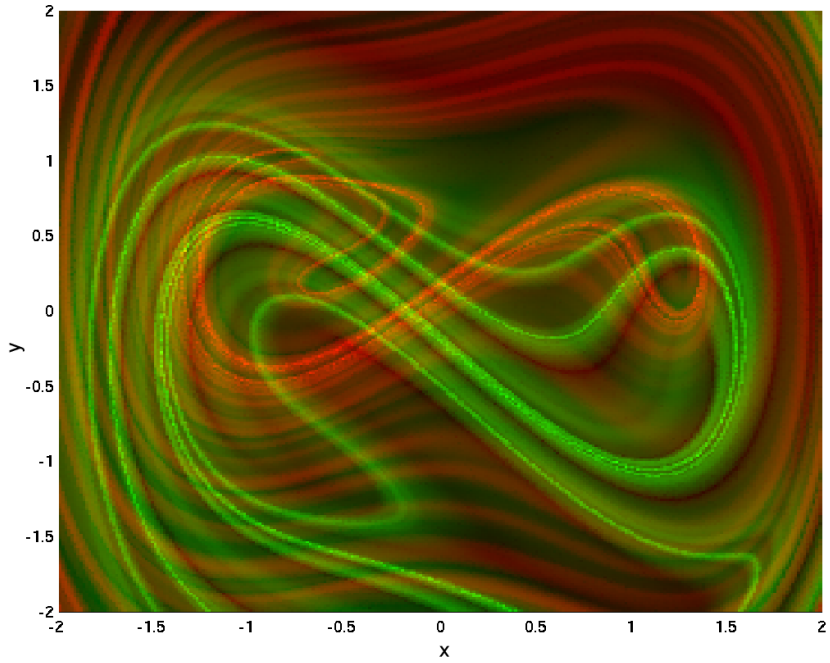

Figure 4.9: Direct expansion rates ($N = 2$) for the Duffing oscillator in forward and backward time uncovering parts of the stable manifold (green) and the unstable manifold (red) forming the Duffing attractor.

center points of a box covering on depth 18 (212744 boxes) are computed and the results for $N = 12$ and $N = 16$ are shown in Figure 4.10. Although there are infinitely many hyperbolic periodic points, the stable manifold of the saddle point is particularly characterized by large expansion rates. We then consider a small neighborhood of the saddle point as shown in Figure 4.11. We observe that the local stable manifold of the saddle appears clearly as a maximizer of the expansion rate.

For an analysis of these results, we numerically computed the periodic points of the Hénon map up to period 7 and checked their dominant Lyapunov exponents. For the saddle point we obtain $\lambda(\bar{x}) \approx 0.65$ whereas for the other periodic orbits we get values between 0.41 and 0.56, remarkably smaller than that of the fixed point. These observations have also been made in [18], where Lyapunov exponents for all periodic orbits up to period 10 have been computed.

With our choices of N, we have only sampled periodic orbits of low periods, which may explain the dominance of the saddle point. However, on the other

hand, periodic orbits of higher periods are expected to sample the whole attractor increasingly better than those of small periods, so that one could assume that their exponents are of the order of $\lambda_1 = 0.42$. Therefore, also an application of Lemma 4.2.7 may provide an explanation for the dominance of the stable manifold of the hyperbolic fixed point.

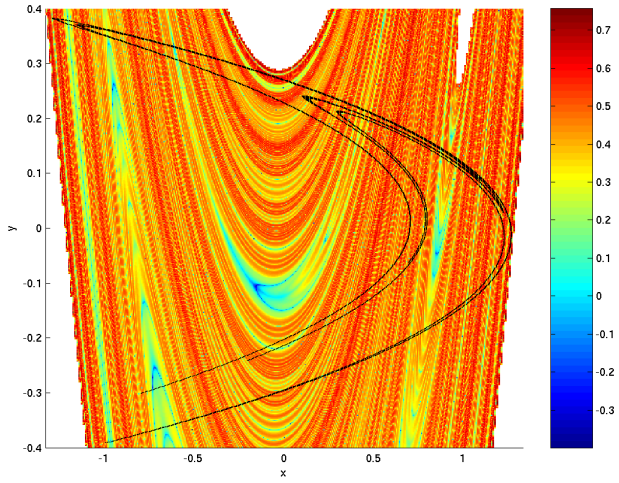

a)

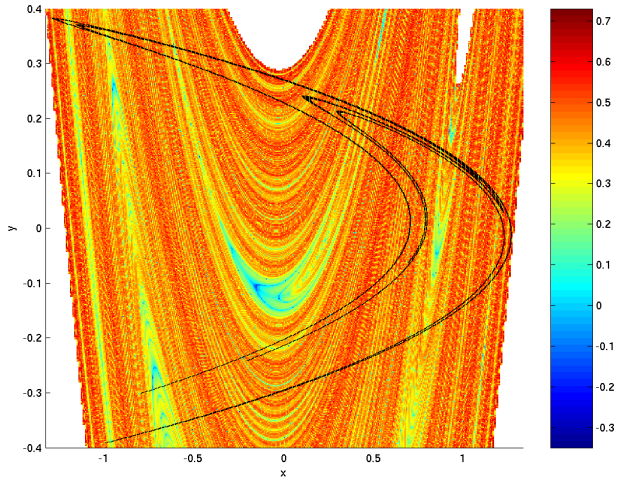

b)

Figure 4.10: Expansion rates for a covering of part of the basin of attraction of the Hénon attractor (black); a) $N = 12$; b) $N = 16$.

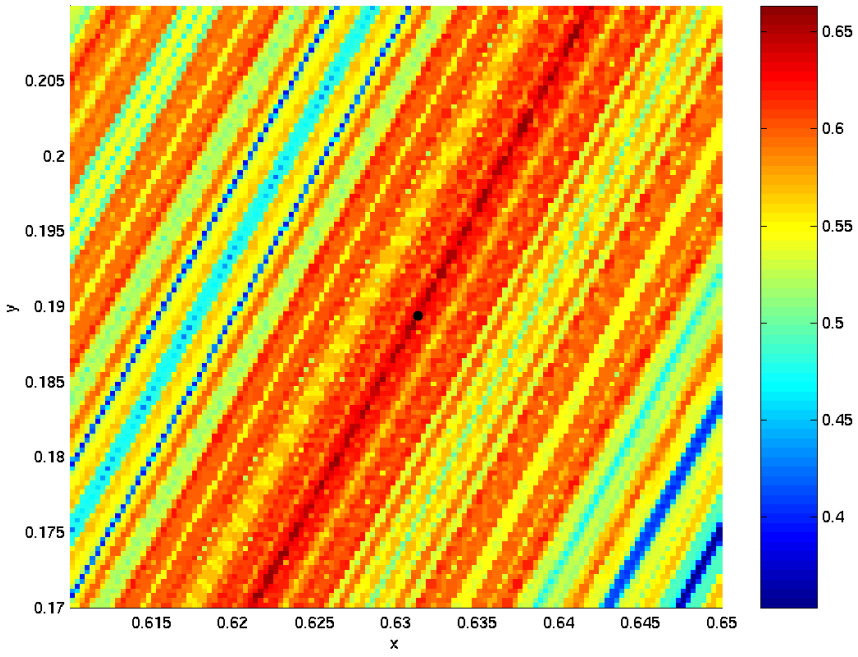

Figure 4.11: Expansion rates for $N = 20$ for a covering of a neighborhood of the saddle point (black dot) in the Hénon Map (depth 14, 25 grid points per box). Clearly visible is the stable manifold of the saddle as a maximizer of the expansion rate. The expansion rate values for the corresponding boxes are in good agreement with the dominant Lyapunov exponent of the unstable fixed point.

4.4 Extraction of Invariant Manifolds

Based on the results of the previous section, we propose a set oriented subdivision algorithm for the extraction of λ-unstable or (λ, N)-unstable sets as candidates for stable manifolds of hyperbolic periodic points. We prove convergence, and, additionally, we introduce a selection criterion for the algorithm that does not need information on the exact size of λ.

4.4.1 The Subdivision Algorithm

Let $\lambda > 0$ be given as well as an initial box Q with $Q \cap A_\lambda \neq \emptyset$ ($Q \cap A_{(\lambda,N)} \neq \emptyset$, respectively). The following algorithm proposes a subdivision scheme for the extraction of $Q \cap A_\lambda$ ($Q \cap A_{(\lambda,N)}$, respectively):

Algorithm 4.4.1 Given an initial collection $\mathcal{B}_0$ one inductively obtains $\mathcal{B}_k$ from $\mathcal{B}_{k-1}$ for $k = 1, 2, \ldots$ in two steps:

1. *Subdivision:* Construct a new collection $\hat{\mathcal{B}}_k$ such that

$$\bigcup_{B \in \hat{\mathcal{B}}_k} B = \bigcup_{B \in \mathcal{B}_{k-1}} B \text{ and } \operatorname{diam}(\hat{\mathcal{B}}_k) \leq \theta \operatorname{diam}(\mathcal{B}_{k-1})$$

   for some $0 < \theta < 1$.

2. *Selection:* Define the new collection $\mathcal{B}_k$ by

$$\mathcal{B}_k = \{B \in \hat{\mathcal{B}}_k \,:\, \delta_{(\varepsilon)}(i, B) \geq \lambda \text{ for } i = 1, \ldots, k\}.$$

Notably, for the extraction of the $A_{(\lambda,N)}$ one defines the new collection $\mathcal{B}_k$ by

$$\mathcal{B}_k = \{B \in \hat{\mathcal{B}}_k \,:\, \delta_{(\varepsilon)}(N - 1 + i, B) \geq \lambda \text{ for } i = 1, \ldots, k\}.$$

The subdivision algorithm produces a covering of the set under consideration, which indeed converges to the set of λ-expansive and (λ, N)-expansive points.

Proposition 4.4.2 *Let $\lambda > 0$ and $Q \subset X$ a compact subset. Let $A_{\lambda,Q} := A_\lambda \cap Q$ be the λ-unstable set with respect to Q and $\mathcal{B}_0$ a finite collection of boxes with $Q_0 := Q = \bigcup_{B \in \mathcal{B}_0} B$. Define $Q_k = \bigcup_{B \in \mathcal{B}_k} B$ as obtained by the subdivision algorithm, using $\delta(\cdot, B)$ in the selection step. Then*

$$A_{\lambda,Q} = Q_\infty.$$

Proof: Along similar lines as in Dellnitz and Hohmann [24]:

1. $A_{\lambda,Q} \subset Q_k$ for all k, as we consider the maximal expansion rate per box, and hence, $A_{\lambda,Q} \subset Q_\infty$.

2. Show that $Q_\infty \subset A_{\lambda,Q}$. For contradiction suppose there is a point $x \in Q_\infty$ such that $x \notin A_{\lambda,Q}$. As $A_{\lambda,Q}$ is compact there is $\delta > 0$ such that $d(x, A_{\lambda,Q}) > \delta$ and we also find $N \in \mathbb{N}$ such that $d(B_k(x), A_{\lambda,Q}) > \frac{\delta}{2}$ for $k > N$, where $B_k(x) \in \mathcal{B}_k$ is the box containing x. Consequently, we find $M > N$ such that $B_l(x) \cap A_{\lambda,Q} = \emptyset$ for all $l > M$, which is impossible by construction of the algorithm.

3. So we have $Q_\infty = A_{\lambda,Q}$ and the desired result.

Note that the convergence is in terms of the Hausdorff distance, see [24]. The convergence to $A_{(\lambda,N)} \cap Q$ can be proved in an analogous way. □

Another possibility is to extract $C_{(\lambda,N)}$ for a particular $N \in \mathbb{N}$. Obviously, this set contains all candidates of (λ, N)-expansive points. Here, in the selection step, we keep the box collection $\mathcal{B}_k$ with

$$\mathcal{B}_k = \{B \in \hat{\mathcal{B}}_k \,:\, \delta_{(\varepsilon)}(N, B) \geq \lambda\},$$

so, the number of iterations for the computation of the expansion rate is kept fixed.

Often, however, one does not know the hyperbolic points responsible for existence of λ-expansive sets, and therefore also λ is not explicitly known. In that case the subdivision algorithm above can be altered in the selection step in the following way

Black-Box-Selection: Define the new collection $\mathcal{B}_k$ by

$$\mathcal{B}_k = \{B \in \hat{\mathcal{B}}_k \,:\, \delta_{(\varepsilon)}(n, B) \geq \langle \delta_{(\varepsilon)}(n, \cdot) \rangle_{\hat{\mathcal{B}}_k}\},$$

where $n = k$, $n = N - 1 + k$ or $n = N$ as described above and $\langle \delta_{(\varepsilon)}(n, \cdot) \rangle_{\mathcal{B}}$ as in Equation 4.2. This procedure works well in test cases, as we will see later.

Sometimes it may be useful to carry out two or more subdivision steps at once before invoking a selection step. This depends on the dimension of the manifold to be extracted, see Schütze [99] for a detailed discussion on the computational effort.

4.4.2 Examples

Undamped Pendulum

The following ordinary differential equation describes the motion of a simple pendulum without friction or forcing:

$$\begin{aligned} \dot{x} &= y \\ \dot{y} &= \sin(x) \end{aligned}$$

The system has saddle points in $(\pi + k \cdot 2\pi, 0)$ and centers in $(k \cdot 2\pi, 0)$, $k \in \mathbb{Z}$. The saddles are connected by heteroclinic orbits, formed by the stable and unstable manifolds of neighboring fixed points. The eigenvalues of the Jacobian in the saddle points are ± 1, so their dominant Lyapunov exponent is 1. We consider the time-1 map $f(x) := \phi^1 x$ for initial conditions on the rectangle $Q = [-4, 4] \times [-3, 3]$. We want to get an approximation of the stable manifolds by extracting the λ-expansive and (λ, N)-expansive sets for different choices of λ. The dynamical system is conservative, so, apart from the saddles and their stable manifolds, all points have zero Lyapunov exponents. The scalar expansion rate field for $N = 10$ is shown in Figure 4.12.

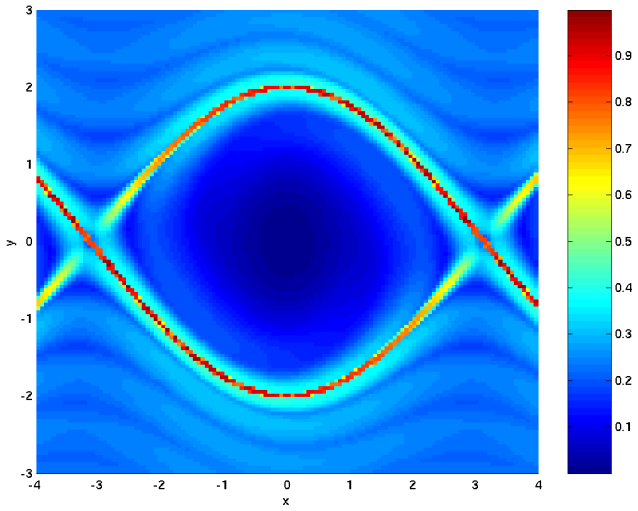

Figure 4.12: Expansion rates field with respect to a box covering on depth 14 (16384 boxes). In each box 100 grid points are chosen and $N = 10$ iterates of the time-1 map are computed.

For λ we choose $0.5, 0.7$ and 0.9. Coverings of the respective λ-unstable sets are shown in Figure 4.13. We choose 25 grid points per box for the approximation

of the set wise expansion rate. We start with a box covering on depth 10 and carry out six steps of the subdivision Algorithm 4.4.1. Note that the coverings form a nested sequence. In Figure 4.13 an approximation of the λ-expansive sets for $\lambda = 0.7$ after ten subdivision steps is also shown.

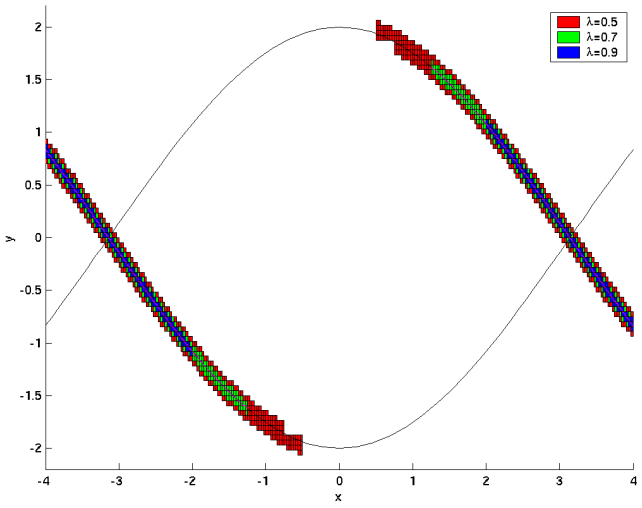

Figure 4.13: Box coverings of λ-expansive sets for the pendulum for different choices of λ. The heteroclinic connection between the two saddles at $(\pm\pi, 0)$ is shown in black. The center points of the covering of $A_{0.7} \cap Q$ after ten subdivision steps are shown in magenta.

Additionally, we demonstrate the results of the subdivision algorithm for $\lambda = 0.5$ and for the Black-Box selection criterion in Figure 4.14. Observe the fast convergence of the latter approach. Moreover, box coverings of different (λ, N)-expansive sets are given in Figure 4.15.

ABC Flow

We consider the following system of ordinary differential equations

$$\begin{aligned} \dot{x} &= A \sin z + C \cos y \\ \dot{y} &= B \sin x + A \cos z \\ \dot{z} &= C \sin y + B \cos x. \end{aligned}$$

This class of flows is known as ABC (Arnold-Beltrami-Childress) flows and it is notable for being an exact solution of Euler's equation, exhibiting a nontrivial

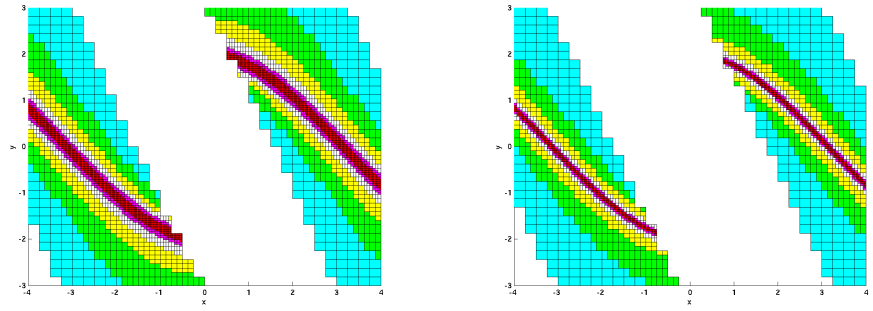

a) b)

Figure 4.14: Subdivision algorithm. a) Nested coverings of $A_{0.5} \cap Q$ after one to six subdivision steps. b) Same for Black-Box Selection.

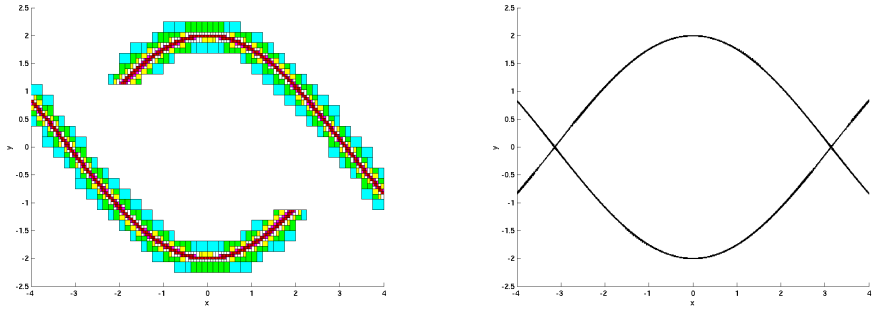

a) b)

Figure 4.15: a) Nested coverings of $A_{(0.5,5)} \cap Q$ after one to six subdivision steps. b) Box covering of $A_{(0.3,10)} \cap Q$ after ten subdivision steps.

streamline geometry. In our numerical studies we consider the cube $[0, 2\pi]^3$ and fix the parameter values $A = \sqrt{3}$, $B = \sqrt{2}$, $C = 1$. For a numerical analysis we refer to Haller [46], and to Dombre et al. [36] for an analytical investigation. The spatial periodicity suggests the employment of Poincaré sections in numerical studies or the consideration of cube planes, such as in [36] or [46]. Their analysis gives clear indication of the location of chaotic and regular regions. These are also visible in Figure 4.16, where we computed the direct expansion rates for different numbers of iterations of the time-1 map.

We want to extract the two-dimensional stable manifolds of hyperbolic periodic orbits from the three-dimensional phase space. These, in Haller's words [46], hyperbolic material surfaces, form the skeleton of the dynamics. We start

with an initial box covering on depth 12, choose $N = 6$ in the subdivision algorithm, and carry out five steps ($k = 1, \ldots 5$) of the subdivision algorithm based on the expansion rates for the box center points. We combine a double subdivision step with a selection step discarding those boxes whose expansion rate is below average (Black-Box approach). The result is shown in Figure 4.17, illustrating the complicated geometry of the mixing regions. To the best of our knowledge this has been the first time that these two-dimensional structures have been fully extracted and visualized.

We also want to extract the centers of the vortices; see [48] for a mathematically objective definition. These elliptic regions are typically characterized by near zero expansion rates. For this we employ the same method as described above but instead we keep the boxes whose expansion rate is below average. Figure 4.18 shows the result of this computation.

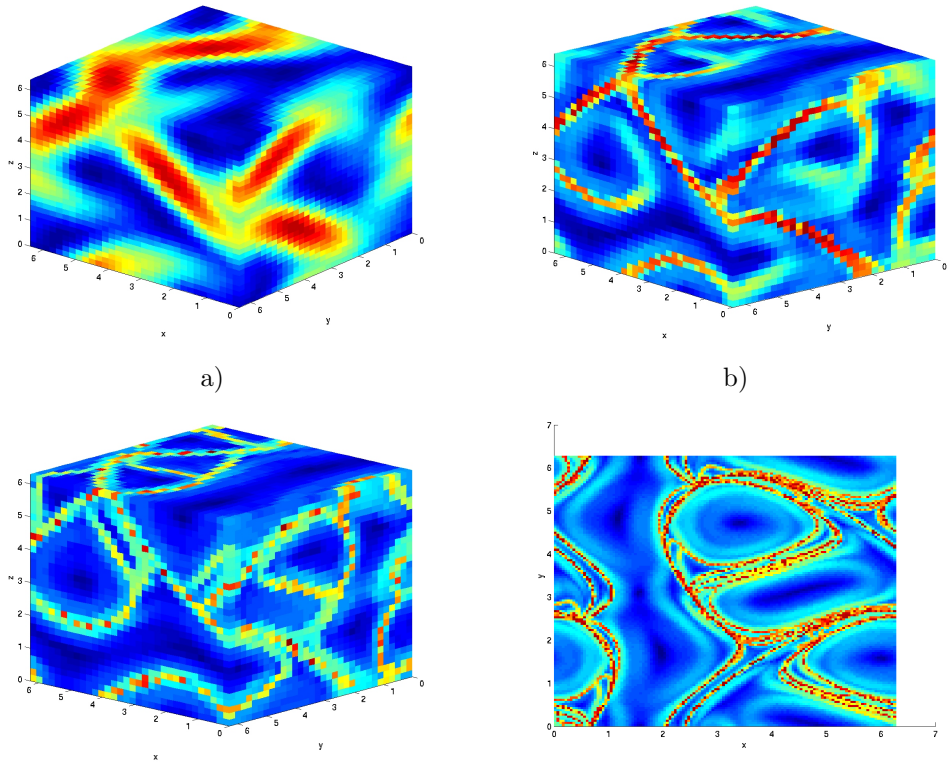

a) b)

c) d)

Figure 4.16: Direct expansion rates for the ABC-flow. The stable manifolds of periodic orbits are characterized by large values (red). Also elliptic regions are clearly visible (dark blue). a) $N = 1$; b) $N = 3$; c) $N = 5$; d) $N = 10$ ($y - z$ plane).

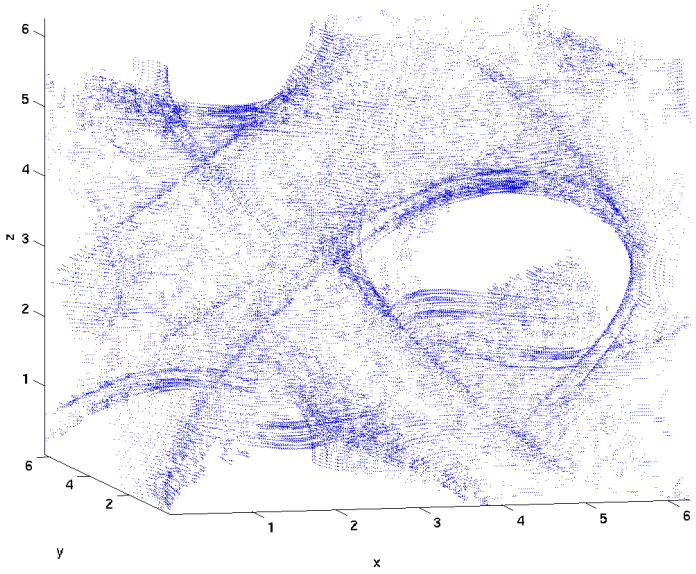

Figure 4.17: Regions in the ABC flow with high expansion, corresponding to hyperbolic material surfaces.

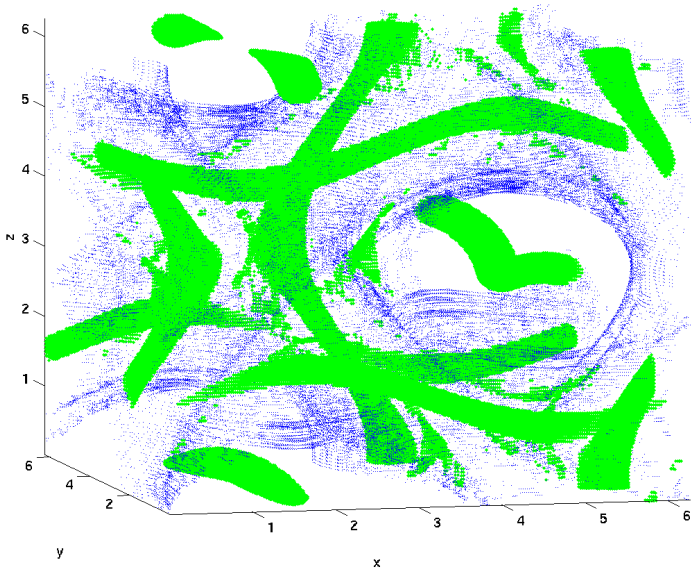

Figure 4.18: Approximation of hyperbolic (blue) and elliptic regions (green) in the ABC flow.

4.5 Expansion in Graphs

As briefly discussed in Chapter 1, the concept of almost invariant sets provides a partition of phase space that does not explicitly use the geometrical template of invariant manifolds. It is not untypical that the boundaries between these sets coincide with invariant manifolds of hyperbolic periodic points as demonstrated in [28] (see Figure 4.20 c)). Recently developed methods for the approximation of almost invariant sets make massive use of graph algorithmic techniques [28, 31, 38], such as implemented in PARTY/GADS [88, 89, 90]. This is a motivation for us to look explicitly for the boundaries between the sets by considering the information coded in the graph. We briefly show how to obtain a weighted, directed graph from a dynamical system, develop heuristics to detect the structures of interest in the graph and illustrate the techniques in two examples.

4.5.1 Dynamical Systems and Graphs

Let $f : X \to X$ be a dynamical system and let $A \subset X$ be a compact invariant set. Then the dynamics on A can be approximated in terms of transition probabilities between boxes. This allows, for example, the approximation of the underlying *SRB*-measure (if it exists), the natural invariant measure. The crucial observation is that the calculation of invariant measures can be viewed as a fixed point problem. Let $\mathcal{M}$ be the set of probability measures on $\mathbb{R}^l$. Then $\mu \in \mathcal{M}$ is invariant if and only if it is a fixed point of the Perron-Frobenius operator $P : \mathcal{M} \to \mathcal{M}$,

$$(P\mu)(B) = \mu(f^{-1}(B))) \text{ for all (measurable) subsets } B \subset \mathbb{R}^l.$$

Now let $B_i \in \mathcal{B}_k$, $i = 1, \ldots, n$, denote the boxes in the covering obtained after k steps in the subdivision algorithm. Following Ulam [107], the most natural discretization of the transfer operator P is given by the stochastic matrix $P_{\mathcal{B}} = (p_{ij})$, where

$$p_{ij} = \frac{m(f^{-1}(B_i) \cap B_j)}{m(B_j)}, \; i, j = 1, \ldots, n \tag{4.3}$$

and m denotes Lebesgue measure. So the matrix entry p_{ij} gives the probability of being mapped from box B_j to B_i in one iterate. Note that $P_{\mathcal{B}}$ is a weighted, column stochastic matrix that is typically sparse and thus defines a finite Markov chain. The transition probabilities can be computed either by a Monte Carlo method (see e.g. [55]) or, if local Lipschitz constants are known for f, by an exhaustion technique [64].

The computation of $P_{\mathcal{B}}$ is fast because rather than considering the long term dynamics only one iterate of f per test point is needed. An approximation of the

natural invariant measure is then given as the eigenvector of $P_{\mathcal{B}}$ corresponding to the eigenvalue 1.

Note that sometimes apart from the eigenvalue at 1 the transition matrix $P_{\mathcal{B}}$ possesses an eigenvalue that is close to 1, indicating the existence of two almost invariant sets: $A_1 \cup A_2 = \bigcup_{B \in \mathcal{B}_k} B$ with $A_1 \cap A_2 = \emptyset$. The respective eigenvector q is an approximation of a signed measure, where the sign structure of the entries in q determines which almost invariant set each box belongs to.

Now let $\mathcal{B}$ be a box covering of A on depth k and $P_{\mathcal{B}}$ the transition matrix (e.g. computed for a grid of initial conditions in each box), and $\mu_{\mathcal{B}}$ an approximation of the natural invariant measure. Then we can construct a graph $G = (V, E)$ with vertex set $V = \mathcal{B}_k$ and with directed edge set

$$E = E(\mathcal{B}) = \{(B_1, B_2) \in \mathcal{B} \times \mathcal{B} : f(B_1) \cap B_2 \neq \emptyset\}.$$

The function $vw : V \to \mathbb{R}$ with $vw(B_i) = \mu_{\mathcal{B}}(B_i)$ assigns a weight to the vertices and the function $ew : E \to \mathbb{R}$ with $ew((B_i, B_j)) = \mu_{\mathcal{B}}(B_i)p_{ji}$ assigns a weight to the edges. Furthermore, let

$$\bar{E} = \bar{E}(\mathcal{B}) = \{\{B_1, B_2\} \subset \mathcal{B} : (f(B_1) \cap B_2) \cup (f(B_2) \cap B_1) \neq \emptyset\}.$$

This defines an undirected graph $\bar{G} = (V, \bar{E})$ with a weight function $e\bar{w} : \bar{E} \to \mathbb{R}$ with $e\bar{w}(\{B_i, B_j\}) = \mu_{\mathcal{B}}(B_j)p_{ij} + \mu_{\mathcal{B}}(B_i)p_{ji}$ on the edges. The difference between the graphs G and $\bar{G}$ is that in $\bar{G}$ the edge weight between two vertices is the sum of the edge weights of the two directed edges between the same vertices in G. Thus, the total edge weights of both graphs are identical. As in typical graph partitioning problems the cost function to be optimized is a function of the edge weights, it is often sufficient to consider the undirected graph.

4.5.2 Graph Based Expansion

We now adapt our expansion rate approach to graphs. As the graph algorithms find almost invariant decompositions without any geometric information we also restrict ourselves to the analysis of the graphs as defined above. Intuitively, structures in the graph (for example, a set of vertices) that correspond to stable manifolds in the underlying dynamical system are expected be characterized by high stretching. This could be measured in terms of the size or weight of subgraphs induced by specific vertices. To make this more precise, we need to briefly introduce some notation.

Let $G = (V, E)$ be a graph with vertex set V and edge set E. Let $vw : V \to \mathbb{R}$ be a weight function on the vertices and let $ew : E \to \mathbb{R}$ be a weight function on the edges. For some $S \subset V$ let $W(S) := \sum_{v \in S} vw(v)$ and for some $F \subset E$ let

$W(F) := \sum_{e \in F} ew(e)$. For some $S \subset V$ let $\bar{S} := V \backslash S$. For some $S, T \subset V$ let $E_{S,T} := \{\{u, v\} \in E; u \in S, v \in T\}$.

In the following statement, different definitions for the expansion of a vertex v are given. For each vertex we consider the set of neighboring vertices $U(v)$. This set is comprised of all vertices that can be reached from v by a path of maximum length d, where d is a small positive integer. As such paths can be seen as pseudo-solutions with respect to the initial value v, we expect that they exhibit similar qualitative characteristics as the respective trajectories in the underlying dynamical system. We therefore expect that the use of measures related to the size or weight of $U(v)$ can pinpoint areas of high stretching in the graph and, thus, in the underlying dynamical system.

Definition 4.5.1 (Expansion of a vertex) For a vertex $v \in V$ let $U(v)$ be the set of vertices from V with a fixed distance of at most d from v. We consider the following definitions $\Lambda_{(i,d)}(v)$ for the **expansion of a vertex** v:

$$\begin{aligned}
\Lambda_{(1,d)}(v) &= |U(v)| & \Lambda_{(5,d)}(v) &= \frac{W(E_{U(v),U(v)})}{W(E_{U(v),\overline{U(v)}})} \\
\Lambda_{(2,d)}(v) &= W(U(v)) & \Lambda_{(6,d)}(v) &= \frac{W(E_{U(v),\overline{U(v)}})}{W(E_{U(v),U(v)})} \\
\Lambda_{(3,d)}(v) &= W(E_{U(v),U(v)}) & \Lambda_{(7,d)}(v) &= \frac{W(E_{U(v),U(v)})}{W(U(v))} \\
\Lambda_{(4,d)}(v) &= W(E_{U(v),\overline{U(v)}}) & \Lambda_{(8,d)}(v) &= \frac{W(E_{U(v),\overline{U(v)}})}{W(U(v))}
\end{aligned}$$

$\Lambda_{(1,d)}(v)$ considers the number of vertices in the subgraph with the expectation that nodes in areas of high stretching will typically span a large subgraph. $\Lambda_{(2,d)}(v)$ is the sum of the vertex weights of the subgraph, $\Lambda_{(3,d)}(v)$ the sum of the edge weights to edges within the subgraph, whereas $\Lambda_{(4,d)}(v)$ measures the weights of edges connecting the subgraph to the rest of the graph. Again one expects that parts of the graph that are characterized by strong mixing are well connected to the rest of the graph. The other four measures are combinations of the former.

4.5.3 Examples

We illustrate our definitions in two examples: the Duffing oscillator and a Poincaré map in the planar circular restricted three body problem, where transport of asteroids can be analyzed as in [28].

Duffing Oscillator

We again come back to the Duffing oscillator (see Example 2.1.16) and consider a box covering of $Q = [-2, 2] \times [-2, 2]$ on depth $k = 14$ (16384 boxes). Note that

Q is forward invariant as it contains the Duffing attractor. For the construction of the weighted, directed graph we compute the transition matrix $P_{\mathcal{B}}$ on this box covering for the time-2π map using 100 grid points per box. Moreover, we approximate the natural invariant measure as described above.

We want to compare the different measures $\Lambda_{(i,d)}(v)$ for the expansion of a vertex v. The results for $d = 1$ and $d = 3$ are shown in Figure 4.19.

For $i = 1, \ldots, 4$ and $i = 6$ the heuristic measures seem to pick up the stable manifold of the underlying dynamical system. For $d = 3$ a larger part of the manifold is unfolded than for $d = 1$. This observation is in accordance with the results of the previous sections.

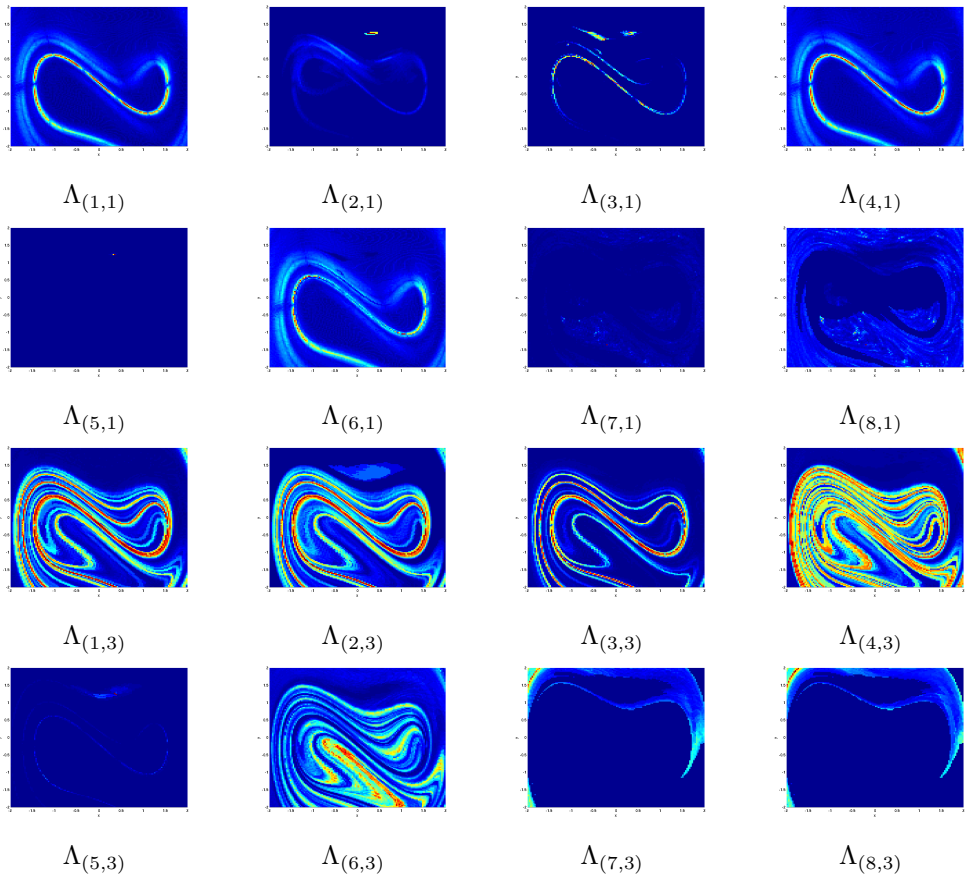

Figure 4.19: Graph based expansion for the Duffing oscillator with respect to a box covering on depth 14 (16384 boxes). The results for different measures for $d = 1$ and $d = 3$ are shown.

Transport of Asteroids

We now consider the example discussed in Dellnitz, Junge, Koon, et al. [28] concerning transport between two resonance regions for the planar circular restricted three body problem (PCRTBP). We only briefly describe the underlying model, for a detailed problem description we refer to [28].

The PCRTBP is a particular case of the general gravitational problem of three masses m_1, m_2, and m_3, assuming that the motion of all three bodies takes place in a common plane. The masses m_1 and m_2, here the Sun and Jupiter, move on circular orbits about their common center of mass. We are concerned with the motion of the massless test particle m_3, the third body. The universal constant of gravitation, $G = 1$, and the masses of the Sun and the planet are $1 - \epsilon$ and ϵ, where $\epsilon = m_2/(m_1 + m_2)$.

Choosing a rotating coordinate system so that the origin is at the center of mass, the Sun and the planet are on the x-axis at the points $(-\epsilon, 0)$ and $(1-\epsilon, 0)$ respectively. Let (x, y) be the position of the particle in the plane, then the equations of motion for the particle in this rotating frame are:

$$\ddot{x} - 2\dot{y} = -\bar{U}_x \qquad \ddot{y} + 2\dot{x} = -\bar{U}_y, \tag{4.4}$$

where

$$\bar{U} = -\frac{x^2 + y^2}{2} - \frac{1-\epsilon}{r_S} - \frac{\epsilon}{r_P} - \frac{\epsilon(1-\epsilon)}{2}.$$

Here r_S and r_P denote the distances from the particle to the Sun and Jupiter, respectively. The system has five fixed points, the libration points $L_1, \ldots, L_5$.

Equations (4.4) have an energy integral which is related to the Jacobi constant C. Hence, the motion of the test particle takes place on a 3-dimensional energy manifold (defined by a particular value of C) embedded in the 4-dimensional phase space $(x, y, \dot{x}, \dot{y})$.

The value of the energy is an indicator of the type of global dynamics possible for a particle in the PCRTBP. In the case discussed in this example, the particle is trapped either exterior or interior to the planet's orbit, or around the planet itself; see Figure 4.20 a). For energy values greater than that of L_2 there is a bottleneck around L_1 and L_2, permitting particles to move between the three realms.

For an analysis of the dynamics we consider the Poincaré surface-of-section (s-o-s) defined by $y = 0, \dot{y} > 0$, and the coordinates $(x, \dot{x})$ on that section, that is, we plot the x coordinate and velocity of the test particle at every conjunction with the planet. As a further restriction, we consider only the motion of test particles in the exterior realm ($x < -1$), see Figure 4.20 a) for an illustration. The mixed phase space structure comprised of regular and chaotic regions is shown in Figure 4.20 b). The system thus defined has a hyperbolic saddle point

at $\bar{x} = (-2.029579567343744, 0)$, where its stable and unstable manifolds form the boundaries between resonance regions.

We consider a box covering of the chain recurrent set [27] on depth 16 (32789 boxes) with $Q = [-2.95, -1.05] \times [-0.5, 0.5]$ for the Poincaré map described above, where $\epsilon = 9.5368e-4$ and $C = 3.05$. The transition matrix $P_{\mathcal{B}}$ is computed with respect to 256 grid points per box. In Dellnitz, Junge, Koon, et al. [28] we have used the undirected graph induced by $\mathcal{B}$, $P_{\mathcal{B}}$ and $\mu_{\mathcal{B}}$ and have shown that graph algorithms tend to pick up the same regions as bounded by the manifolds, see Figure 4.20 c).

Therefore we expect to find the relevant invariant manifolds even in the undirected graph. In order to unfold these structures we choose $d = 3$ and compute expansion of the vertices for the directed and undirected graph. Results for some of the measures $\Lambda_{(i,d)}$ together with parts of the stable and unstable manifold, computed using the continuation Algorithm 3.2.1 described in Chapter 3, are shown in Figure 4.21. Note that the structures characterized by high expansion have striking similarities to the invariant manifolds of the underlying dynamical system.

4.5.4 Discussion

In this section we have introduced a few heuristic measures for the analysis of expansive regions in graphs and have illustrated these definitions in two examples. The expansion $\Lambda_{(i,d)}(v)$ of a vertex v as defined above seems to produce the desired results especially for $i = 1, \ldots, 4$. However, the measures need to be tested more seriously and, of course, analyzed theoretically. Nevertheless, these experiments are a first step in the analysis of large data sets such as time series.

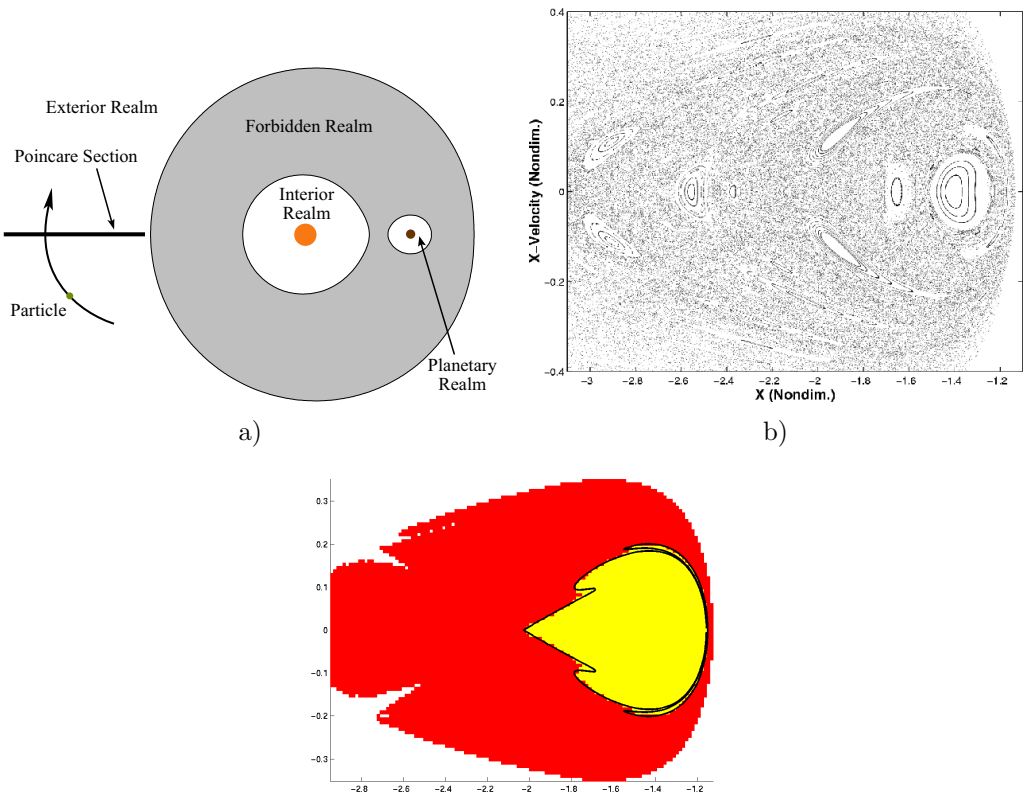

Figure 4.20: A Poincaré section of the flow in the restricted three-body problem. (Graphics taken from [28]). a) The location of the Poincaré surface-of-section (s-o-s). b) The mixed phase space structure of the PCRTBP is shown on this s-o-s. c) The red and yellow areas are an almost invariant decomposition into two sets. The border between the two sets roughly matches the boundary formed by the branches of the stable and unstable manifolds of the fixed point $(-2.029579567343744, 0)$ drawn as a line.

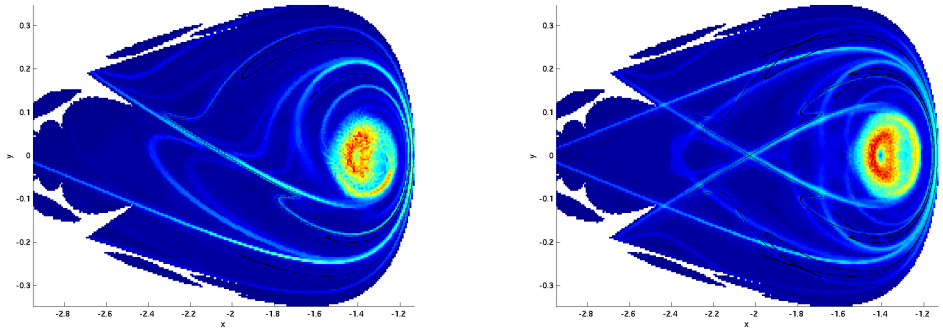

$\Lambda_{(2,3)}$ $\Lambda_{(2,3)}$

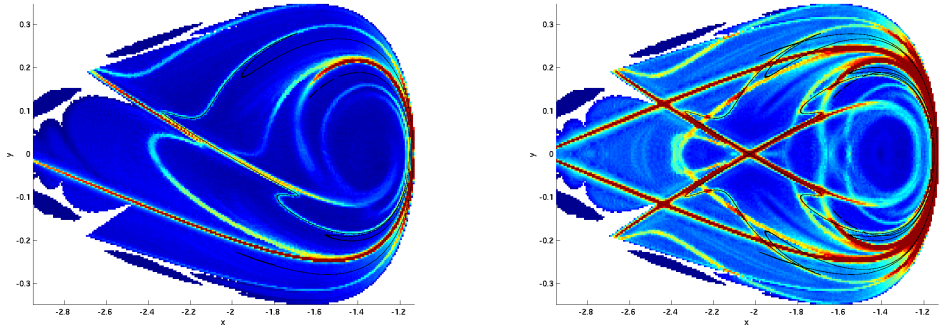

$\Lambda_{(3,3)}$ $\Lambda_{(3,3)}$

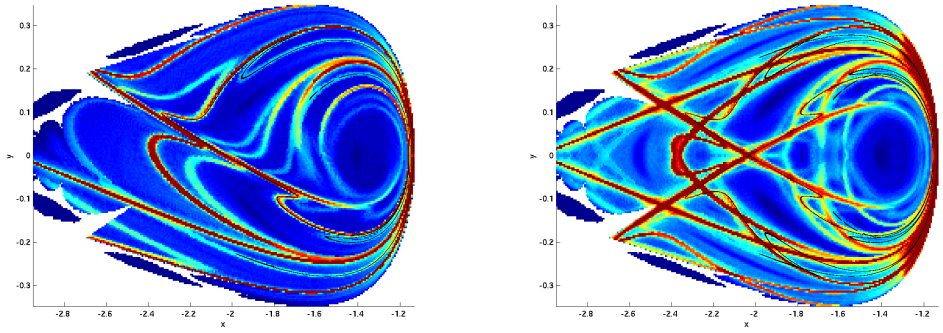

$\Lambda_{(4,3)}$ $\Lambda_{(4,3)}$

Figure 4.21: Transport of asteroids. Analysis of the graph based expansion, where different measures for $d = 3$ for the directed (left column) and undirected graph (right) are used. Parts of the stable and unstable manifold of a hyperbolic fixed point are superimposed (black).

Chapter 5

Analyzing Transport in Non-Autonomous Systems

5.1 Introduction

The analysis of transport in time-dependent dynamical systems has been an active research area in the past ten years. Obviously, for the numerical investigation of transport phenomena two main ingredients need to be considered: first one needs to detect and extract the relevant boundaries in the given dynamical system or data set. After that transport between these respective areas is quantified in terms of transport rates or transport probabilities. For this an approximation of the transport mechanism needs to be derived.

As already discussed in the introduction, once the invariant manifolds are approximated the transport rates are typically computed using lobe dynamics or related concepts [17]. However, this requires very detailed information on the invariant manifolds and an accurate approximation of fine scaled structures. These are often not available if finite data sets are considered and when numerical errors are involved. Moreover, while certainly feasible in two-dimensional systems, the estimation of volumes may cause problems in higher dimensions as well as in systems that are not volume-preserving. A major problem is also that certain transport mechanisms may not be explained via lobe dynamics [49, 62].

Here we want to provide alternative techniques for the analysis of transport in non-autonomous systems. First, in order to detect and extract invariant manifolds, we extend the expansion rate methods introduced in Chapter 4 to non-autonomous systems. In the time-dependent setting the (direct) expansion rates do not only depend on the integration time but also on the initial time. Nevertheless, all methods introduced in Chapter 4 are immediately applicable if one considers single τ-fibers. These provide a set of initial conditions for a fixed ini-

tial time, the expansion rates are then computed for solutions in phase space (see Remark 2.2.4). One typically needs to analyze a large number of time slices in order to be able to observe the temporal behavior of the structures of interest. To avoid this we propose a set oriented continuation scheme: it uses the fact that once part of the stable manifold is given for fixed τ, the manifold can be continued in backward time to obtain a part for time $\tau - T$. The methods are demonstrated by two examples. We remark that, similar to the autonomous case, we are, in general, not restricted to the analysis of two- or three-dimensional systems.

In the second part of this chapter we propose a set oriented approach for the computation of transport rates which is independent of manifolds. Moreover, our technique can deal with systems that are not volume-preserving without any additional effort. The method is based on the discretization of Perron-Frobenius operators such as introduced by Ulam [107]; see also [64] for a detailed discussion of this concept. This method allows the approximation of transport rates and probabilities between arbitrary sets of interest in non-autonomous systems. It extends the results proposed in Dellnitz, Junge, Koon, et al. [28] where the autonomous case has been treated.

5.2 Time-Dependent Invariant Manifolds

Various approaches have been developed over the last ten years for the numerical approximation of hyperbolic trajectories and their stable and unstable manifolds in non-autonomous dynamical systems, or even in systems where the velocity field is only defined for finite time. See Jones and Winkler [61] and Wiggins [112] for a discussion of different techniques in the context of geophysical fluid flows.

We briefly explain the philosophy of several approaches. A variety of methods deal with the location of hyperbolic regions, that is, regions that contract and stretch as they evolve with the flow. One approach is the Eulerian approach where the velocity field is considered on fixed time slices. Saddle points, so-called instantaneous stagnation points (ISPs), in these time frozen velocity fields may be a good first guess for a hyperbolic region in the flow. Although deciding whether a region is considered hyperbolic is often subjective, the purpose is mainly to find initial conditions for more refined techniques. The Eulerian approach is used by Malhotra and Wiggins [78] and Miller et al. [84].

Of course, a curve of ISPs is usually not a trajectory, but in the case where the time variation of the velocity field is slow it may indicate the existence of a hyperbolic trajectory staying close to the curve. This is intuitively clear from perturbation theory; see Haller and Poje [49] for an extension of this result and Poje and Haller [87] for an application to cross-stream mixing in a double-gyre ocean model.

Ide et al. [56], Ju et al. [63], and Mancho et al. [80] introduce a method that does not require slow time variation. It uses an iteration technique, which, when it converges, is guaranteed to converge to a hyperbolic trajectory. The curve of ISPs is used as an initial guess, but it is not required that the trajectory stays in the proximity of this curve.

Once the underlying hyperbolic trajectory has been approximated the stable and unstable manifolds can then be obtained using refined continuation techniques. A standard method is the straddling technique as introduced by You, Kostelich, and Yorke [114]; see [80] for an improved version using sophisticated point insertion and interpolation schemes. In Mancho et al. [79] this approach is applied to an oceanographic flow given as a finite data set.

The methods described above compute invariant manifolds based on an approximation of the underlying hyperbolic trajectory, where the latter seems to be the crucial part. Often the conditions for the existence of the hyperbolic trajectory are difficult if not impossible to verify in arbitrary systems. Also note that the methods and applications described above are formulated for two-dimensional systems.

Therefore, a different philosophy is to look directly for structures in the flow or data set that behave like invariant manifolds and approximate the manifolds of interest or at least their candidates. As discussed in Chapter 2 under certain assumptions the unstable manifold of a hyperbolic trajectory can be shown to coincide with the global pullback attractor [7, 8, 104]. In Chapter 3 we have described set oriented methods for the numerical approximations of pullback attractors as introduced by Aulbach et al. [7, 8] and Siegmund [104]. However, generally, these methods approximate *all* attracting sets with respect to a given time slice, where in our case we are usually interested in specific manifolds.

Another family of methods deals with statistical quantities such as finite-time Lyapunov exponents and exploit the fact that a stable manifold of a hyperbolic object is repelling (see e.g. Lapeyre [72]). While for analytically given velocity fields the computation of finite-time Lyapunov exponents, or related concepts like finite-size Lyapunov exponents [9, 10, 62, 70], is often the method of choice, the Jacobian is usually not available when the velocity field is given as a finite set of data points. Apart from the large computational effort, the numerical approximation of the derivatives introduces additional errors. This problem is at least partially circumvented by using the relative dispersion methods [12, 61, 108, 113] addressed in the previous chapter, which highlight areas of high stretching. Moreover, Haller introduces the direct Lyapunov exponent [46, 47], which is obtained by taking the numerical derivation of particle positions at a specific time with respect to a dense enough grid of initial conditions; see [109] for a comparison of the results with experimental measurements.

All these methods take necessary but usually not sufficient conditions for the

existence of (finite-time) stable manifolds into account. A technique based on the computation of hyperbolicity times by Haller [45, 46], generalized by Lapeyre et al. [73] fills this gap. Essentially, the eigenvalue structure of the Jacobian is used to distinguish between hyperbolic, elliptic and parabolic regions of the flow. By considering those trajectories that remain in the hyperbolic regime for the longest time, local stable manifolds are obtained. However, the technique is restricted to two and three dimensions and is computationally demanding.

Based on the ideas discussed in the previous chapter we extend our theoretical results and numerical methods to the non-autonomous case in order to detect candidates for (finite-time) invariant manifolds. However, in the time-dependent setting the (direct) expansion rates do not only depend on the integration time but also the initial time. Nevertheless, the methods introduced in Chapter 4 are immediately applicable if one considers a box covering with respect to single time slices. The structures of interest on the respective time slice are detected using the expansion rate or direct expansion rate approach in phase space. Using direct expansion rates seems to be particularly appropriate when only discrete velocity data is available and therefore the Jacobian could only be obtained numerically. The subdivision algorithm can be employed to extract λ-expansive sets on a time slice. Hence, because of the time-dependence, one typically needs to carry out these computations for a large number of time slices in order to analyze the temporal behavior of the structures of interest. To avoid this we propose a set oriented continuation scheme which works roughly as follows: for some initial time τ we are given the box covering of the λ-unstable set of points on the τ-fiber obtained by the subdivision algorithm as introduced in 4. We approximate regions with the same properties for initial times $t < \tau$ by employing a continuation step as described in Chapter 3, followed by a selection step restricting the box covering of the t-fiber to the λ-unstable set again.

5.2.1 Theoretical Results

In the same way as in the previous section we can define finite-time Lyapunov exponents and direct expansion rates for non-autonomous systems. For the remainder of this section we assume that our system under consideration is defined for infinite times. Characteristics for finite-time velocity fields will be addressed only briefly.

We consider non-autonomous differential equations of the form

$$\dot{x} = f(x,t), \text{ with } x \in \mathbb{R}^l,\, t \in \mathbb{R},$$

where $f : \mathbb{R}^l \times \mathbb{R} \to \mathbb{R}^l$ is C^r $(r \geq 1)$ in x and continuous in t. We assume that the unique solution $\varphi^{t,t_0}x_0$ to the initial value problem $x_0 = x(t_0)$ exists for all $t \in \mathbb{R}$.

Definition 5.2.1 (Expansion rate) Let $\tau, T \in \mathbb{R}$. The **expansion rate** or **finite-time Lyapunov exponent** is given by

$$\begin{aligned}\Lambda(T;\tau,x) &= \frac{1}{|T|}\log\left|D\varphi^{T+\tau,\tau}x\right| \\ &= \frac{1}{2|T|}\log[\lambda_{max}((D\varphi^{T+\tau,\tau}(x))^{\top}D\varphi^{T+\tau,\tau}(x)].\end{aligned}$$

In a similar manner we obtain the direct expansion rate.

Definition 5.2.2 (Direct expansion rate) Let $\varepsilon > 0$. The **direct expansion rate** is defined as

$$\Lambda_{\varepsilon}(T;\tau,x) = \frac{1}{|T|}\log\left(\max_{\{x:|x'-x|=\varepsilon\}}\frac{\left|\varphi^{T+\tau,\tau}(x') - \varphi^{T+\tau,\tau}(x)\right|}{\varepsilon}\right),$$

where $T, \tau \in \mathbb{R}$.

Here we have used the absolute value of T in the denominator to deal with backward time integration. It seems to be natural to consider expansion rates fields with respect to particular time slices, that is, initial conditions on a τ-fiber of the non-autonomous set. Note that the computation of the (direct) expansion rates is carried out in phase space, not in the extended phase space (see also Remark 2.2.4).

Analogously to the autonomous case we can define (λ, T)-expansive sets.

Definition 5.2.3 ((λ,T)-expansive) Let $\Sigma \subset \mathbb{R}^l \times \mathbb{R}$ be a non-autonomous set with fibers $\Sigma(\tau) \subset \mathbb{R}^l$, $\tau \in \mathbb{R}$. We call $x \in \Sigma(\tau)$ (λ, T)**-expansive** if there is a constant $\lambda > 0$ and $T > 0$ such that

$$\Lambda(t;\tau,x) \geq \lambda \; \forall \, t \geq T > 0.$$

The set of (λ, T)-expansive points with respect to a τ-fiber is denoted by $A_{(\lambda,t)}(\tau)$. Let

$$C_{(\lambda,t)}(\tau) := \{x \in \Sigma(\tau) : \Lambda(t;\tau,x) \geq \lambda\}.$$

Then

$$A_{(\lambda,T)}(\tau) := \bigcap_{t \geq T > 0} C_{(\lambda,t)}(\tau).$$

We define the families of time-dependent sets

$$\begin{aligned}C_{(\lambda,t)} &:= \{C_{(\lambda,t)}(\tau)\}_{\tau\in\mathbb{R}} \\ A_{(\lambda,T)} &:= \{A_{\lambda,T}(\tau)\}_{\tau\in\mathbb{R}}\end{aligned}$$

The relation between λ-expansive sets and uniformly hyperbolic trajectories is given in the following Proposition.

Proposition 5.2.4 *Let $\Gamma(t) = (\gamma(t), t)$ be a uniformly hyperbolic trajectory in $\mathcal{E}$. Then there is $\lambda > 0$ and $T > 0$ such that $\Gamma(t) \subset A_{(\lambda,T)}$.*

Proof: Let $x_0 = \gamma(0)$ be a point on the trajectory. Let $X(t) := D\varphi^{t,0}x_0$ be a fundamental matrix solution and $X(0) = I$. Denote $Y(t) := D\varphi^{0,t}(\varphi^{t,0}x_0)$. Clearly from the chain rule it follows that $Y(t) = X^{-1}(t)$, $t \in \mathbb{R}$, and also $Y(0) = I$. As $\gamma(t)$ is uniformly hyperbolic we find a projection P, which can be chosen to be orthogonal (see [34], Lemma 6.1), and dichotomy constants $K \geq 1, \mu > 0$ such that

$$\left|Y(t)(I-P)\right| \leq Ke^{-\mu t},$$

with $t \in \mathbb{R}$. As P is an orthogonal projection we find an orthogonal matrix Q such that $P = Q^\top P_1 Q$, where P_1 is a diagonal matrix with $0s$ and $1s$ on the diagonal. Hence $\left|I - P\right| = 1$. Now we have the following estimate:

$$1 = \left|X(t)Y(t)(I-P)\right| \leq \left|X(t)\right|\left|Y(t)(I-P)\right| \leq \left|X(t)\right|Ke^{-\mu t}.$$

So it follows for all $t \in \mathbb{R}$ that

$$\left|X(t)\right| \geq \frac{1}{K}e^{\mu t}.$$

As $K \geq 1$ and $\mu > 0$, there is $\tilde{T} > 0$ (i.e. $\tilde{T} > \frac{\log K}{\mu}$) such that $\frac{1}{K}e^{\mu\tilde{T}} > 1$. Because of the exponential growth, we can find $0 < \lambda \leq \mu$ and $T \geq \tilde{T}$ such that

$$\frac{1}{t}\log\left|X(t)\right| \geq \lambda$$

for all $t \geq T$. Relabeling gives that each x_0 on $\gamma(t)$ is (λ, T)-expansive, consequently $\Gamma(t) \subset A_{(\lambda,T)}$. ∎

In the same manner as in the autonomous case (Lemma 4.2.3) one can show the following relations between the stable manifold and λ-expansive sets:

Proposition 5.2.5 *Let $\Gamma(t) \subset A_{(\lambda,T)}$ be a uniformly hyperbolic trajectory in the extended phase space. Let $\mathcal{D}_\rho(\tau) \in (\Sigma(\tau), \tau)$ denote the ball of radius ρ centered at $\gamma(\tau)$ and define the tubular neighborhood of $\Gamma(t)$ in $\mathcal{E}$:*

$$\mathcal{N}(\Gamma(t)) := \bigcup_{\tau\in\mathbb{R}} (\mathcal{D}_\rho(\tau), \tau).$$

Let ρ_0 be sufficiently small. Then for $\rho \in (0, \rho_0)$ there is $\lambda \geq \mu > 0$ and $\tilde{T} \geq T > 0$ such that $W^s_{loc}(\Gamma(t)) \subset A_{(\mu,\tilde{T})}$, where $W^s_{loc}(\Gamma(t)) \subset \mathcal{N}(\Gamma(t))$ is the local stable manifold of $\Gamma(t)$ as introduced in Theorem 2.2.6.

Proof: In an analogous way to the autonomous case the statement follows from the continuity of the expansion rate for fixed times as well as the exponential convergence of trajectories in the stable manifold to the hyperbolic trajectory. □

Notes on finite-time velocity fields

As already remarked in Chapter 2, in the context of finite-time velocity fields we are restricted to deal with finite-time invariant manifolds. These are typically not unique and the definition of global manifolds is also problematic.

In this context Haller [46] (see also Haller and Yuan [50], as well as Shadden, Lekien, and Marsden [102]) uses an alternative concept and considers directly characteristic structures in two- and three-dimensional non-autonomous flows. In these systems the structures organizing the dynamics are typically one- or two-dimensional material lines $\mathcal{L}(t)$ and surfaces $\mathcal{M}(t)$, that is, smooth curves and surfaces of fluid particles advected by the velocity field. Now let $I \subset \mathbb{T}$ be an open interval within the finite time interval $\mathbb{T} := [t_-, t_+]$. $\mathcal{L}(t)$ or $\mathcal{M}(t)$ are called **attracting over** I if infinitesimal perturbations from $\mathcal{L}(t)$ or $\mathcal{M}(t)$ converge exponentially to the material objects while in I. A material object is **repelling over** I if it is attracting over I in backward time, hence infinitesimal perturbations diverge from $\mathcal{L}(t)$ or $\mathcal{M}(t)$ at an exponential rate. Haller [46] calls these attracting or repelling objects **finite-time hyperbolic material lines** and **surfaces**. The objects are also known as **Lagrangian coherent structures**, see Haller and Yuan [50] and especially Shadden, Lekien, and Marsden [102] for a discussion. In the latter manuscript, Lagrangian coherent structures are defined as ridges in the scalar finite-time Lyapunov exponent field. This requires the evaluation of the Hessian matrix.

Checking whether material objects are attracting or repelling in Haller's sense requires measuring the growth of infinitesimal perturbations normal to the object. The expansion rate however measures all kinds of stretching. Hence, $A_{(\lambda,T)}$ can be seen as a superset of finite-time hyperbolic objects or material lines. Of course, the time span under consideration needs to be appropriately reduced, so we use I instead of $\mathbb{R}$ in the definition of λ-expansivity.

In Malhotra et al. [78] and Wiggins [112] a definition for a finite-time hyperbolic trajectory is given that is not dichotomy-based. In their setting a trajectory is finite-time hyperbolic on $[t_-, t_+]$, if none of its finite-time Lyapunov exponents are zero on this interval. In the previous paragraphs we have derived a similar relation between finite-time Lyapunov exponents and the dichotomy concept.

We will not give any explicit finite-time theory when developing the numerical algorithms in the following section. Nevertheless, in Chapter 6 our methods are successfully applied to a case where the velocity field is given as a finite data

set. In particular, we extract Lagrangian coherent structures in the context of geophysical fluid flows.

5.2.2 Numerical Methods

The set oriented expansion rates methods introduced in Chapter 4 are immediately applicable to the non-autonomous and finite-time setting. Instead of dealing with the entire extended phase space we consider the dynamics with respect to time slices. Suppose we are given a box collection $\mathcal{B}_k$ that is a covering of our region of interest, in this case a covering of a fiber $\Sigma(\tau)$ of the non-autonomous set. We then define the expansion rate for a box $B \in \mathcal{B}_k$ as

$$\delta(T;\tau,B) := \max_{x\in B} \Lambda(T;\tau,x),$$

and in an analogous way the direct expansion rate for B as

$$\delta_\varepsilon(T;\tau,B) := \max_{x\in B} \Lambda_\varepsilon(T;\tau,x_0).$$

These quantities can be efficiently approximated as described in Chapter 4. Also the subdivision Algorithm 4.4.1 for the numerical extraction of $A_{(\lambda,T)}(\tau)$ or $C_{(\lambda,T)}(\tau)$ can be employed. Note that, of course, the selection criterion can only be evaluated at discrete time steps.

However, because of the time-dependence, one typically needs to carry out these computations for a large number of different time slices in order to analyze the temporal behavior of the structures of interest. To avoid this computational load a continuation algorithm is introduced in the following paragraphs.

5.2.3 The Continuation Algorithm

As discussed in Chapter 2 each time slice of the stable manifold is (pullback) attracting in the time reversed system. So the idea is to first extract the stable manifold candidate on a given τ-fiber using the subdivision Algorithm 4.4.1. Then the box covering is mapped to some past time slice at $\tau - T$ using the continuation step in Algorithm 3.3.3, see Remark 3.3.4. In a subsequent corrector step the required λ-expansive behavior is checked.

Let $Q \subset \mathbb{R}^l$ and for $k = 0, 1, \ldots$ let

$$\mathcal{P}_k = \bigcup_{B\in\mathcal{B}_k} B, \text{ with } B \cap B' = \emptyset \text{ for B } \neq B' \in \mathcal{B}_k$$

be a partition of Q on level k, obtained by applying the subdivision step (1.) in Algorithm 3.1.1 k times with respect to the initial box $\mathcal{B}_0 := Q$.

Algorithm 5.2.6 Let $\{\varphi^{t,s}\}$ be a cocycle with respect to the non-autonomous differential equation $\dot{x} = f(x,t)$, $x \in \mathbb{R}^l$, $t \in \mathbb{R}$. Moreover, let $\lambda > 0$, $\tau \in \mathbb{R}$, $\tilde{T} > 0$, $h > 0$ and $n \in \mathbb{N}$ be given.

Let $\mathcal{P}_k$ be a box partition of the compact set Q on level k consisting of m boxes. Let B_I, where $I = \{i \in \{1,\dots,m\} : B_i \cap A_{(\lambda,\tilde{T})}(\tau) \neq \emptyset\}$, denote the boxes in a covering of $A_{(\lambda,\tilde{T})}(\tau) \cap Q$ (e.g. as obtained by the application of the subdivision Algorithm 4.4.1). Choose $T > 0$. Set

$$\hat{\varphi}(1,\tau)B_I = B_{\tilde{J}},$$

where

$$\tilde{J} := \{j \in \{1,\dots,m\} : B_j \cap \varphi^{\tau-T,\tau} B_I \neq \emptyset\}.$$

Then we compute an approximation of $A_{(\lambda,\tilde{T})}(\tau - T) \cap Q$ following these two steps.

1. *Continuation (Predictor step):*

$$B_{\tilde{J}} = \hat{\varphi}(1,\tau)B_I.$$

2. *Selection (Corrector steps):*
   Obtain covering B_J by selecting

$$J := \{j \in \tilde{J} : \delta_{(\varepsilon)}(\tilde{T} + i \cdot h; \tau - T, B_j) \geq \lambda \text{ for } i = 0,\dots,n\}.$$

A convergence statement for this algorithm is given in the following Proposition:

Proposition 5.2.7 *Let $\Gamma(t)$ be a uniformly hyperbolic trajectory in the extended phase space. Let $\lambda > 0$ and $\tilde{T} > 0$ such that $W^s_{loc}(\Gamma(t)) \subset A_{(\lambda,\tilde{T})} \subset W^s(\Gamma(t))$. Suppose further that $\Gamma(t) \subset Q \times \mathbb{R}$ and that $A_{(\lambda,\tilde{T})}(t) \cap Q$ is connected for each $t \in \mathbb{R}$. Let $\tau \in \mathbb{R}$ be given. Then for each $\tilde{\varepsilon} > 0$ we find $\tilde{d} = \operatorname{diam} \mathcal{B}_k$, $T > 0$ and $n \in \mathbb{N}$ in the above algorithm (using $\delta(\cdot, B)$ in the selection step) such that $d_H(Q_J, A_{(\lambda,\tilde{T})}(\tau - T) \cap Q) < \tilde{\varepsilon}$. Here $Q_J = \cup_{j \in J} B_j$, and d_H denotes the Hausdorff distance.*

Proof: Let $\tilde{\varepsilon} > 0$. Let B_I, $I \subset \{1,\dots,m\}$, denote the boxes of a covering of $A_{(\lambda,\tilde{T})}(\tau) \cap Q$ on depth k obtained by an application of the subdivision Algorithm 4.4.1. Note that every $t-$fiber of $W^s_{loc}(\Gamma(t))$ has a non-empty intersection with Q. As $W^s_{loc}(\Gamma(t)) \subset A_{(\lambda,\tilde{T})} \subset W^s(\Gamma(t))$, we find $T > 0$ such that after the continuation step $A_{(\lambda,\tilde{T})}(\tau - T) \cap Q \subset \hat{\varphi}(1,\tau)B_I$. This follows from the fact that under time reversal the stable manifold consists of solutions which grow exponentially and especially from the fact that the local stable manifold fiber at time τ is a generator for the global stable manifold fiber at time $\tau - t$ for $t \to \infty$. See also [67] for a related statement.

Given this coarse covering of $A_{(\lambda,\tilde{T})}(\tau - T) \cap Q$ we find $n \in \mathbb{N}$ such that the selection step arrives at a covering of $A_{(\lambda,\tilde{T})}(\tau - T) \cap Q$ where no more boxes are discarded. This is true because the box level is kept fixed. Note that the accuracy $\tilde{\varepsilon} > 0$ can be achieved by simply adapting the box diameter $\tilde{d}$ in the partition $\mathcal{P}_k$, that is, in the subdivision algorithm. □

Remarks 5.2.8

1. The condition $\Gamma(t) \subset Q \times \mathbb{R}$ can be ensured by a time-dependent coordinate transformation, which moves the hyperbolic trajectory into zero. The new system has the general form $\dot{y} = A(t)y(t) + g(y,t)$, where $A(t)$ is the linearization with respect to the hyperbolic trajectory $\gamma(t)$, and $y(t) = x(t) + \gamma(t)$ [63]. In this case, Q may be chosen as a box with center at the origin.

2. The condition that $A_{(\lambda,\tilde{T})}(t) \cap Q$ is connected for every $t \in \mathbb{R}$ is satisfied if Q is chosen small enough.

3. Finally, we can relax the above requirements by considering a large enough finite interval $\mathcal{I} \subset \mathbb{R}$ with $\tau - T, \tau \in \mathcal{I}$.

In typical applications it is often sufficient to extract $C_{(\lambda,\tilde{T})}(\tau)$. After the continuation step we carry out only one selection step and thus restrict the covering to an approximation of $C_{(\lambda,\tilde{T})}(\tau - T)$.

5.2.4 Examples

We illustrate our method with two examples. First we consider a variation of the Duffing oscillator with decaying aperiodic forcing as used in Mancho et al. [80]. The second model contains a simple double gyre structure with an oscillating separation point as proposed by Shadden, Lekien, and Marsden [102].

Duffing Oscillator with Aperiodic Forcing

Another variation of Duffing's equation with decaying aperiodic forcing is given by the following non-autonomous differential equation (see Mancho et al. [80])

$$\begin{aligned} \dot{x} &= y \\ \dot{y} &= x - x^3 + \epsilon e^{-(t+2)} \cos(t+2). \end{aligned}$$

We fix $\epsilon = 0.1$. The system exhibits a hyperbolic trajectory which tends to zero for $t \to \infty$. We approximate parts of its stable manifold on different time-slices using the following set-up. We choose a box covering of the compact set $Q = [-2,2] \times [-2,2]$ and depth 14 (16384 boxes). We compute the direct expansion rates using

20 pairs of Monte Carlo points in each box with initial distance $\varepsilon \approx 0.00156$ (corresponding to 20% of the box radius). We consider initial times $\tau \in [-6, 0]$ and $T = 10$. The results for different time slices are shown in Figure 5.1. Note that the stable manifold is asymmetric for $\tau < 0$ but settles down to a figure-8 double homoclinic orbit for larger τ.

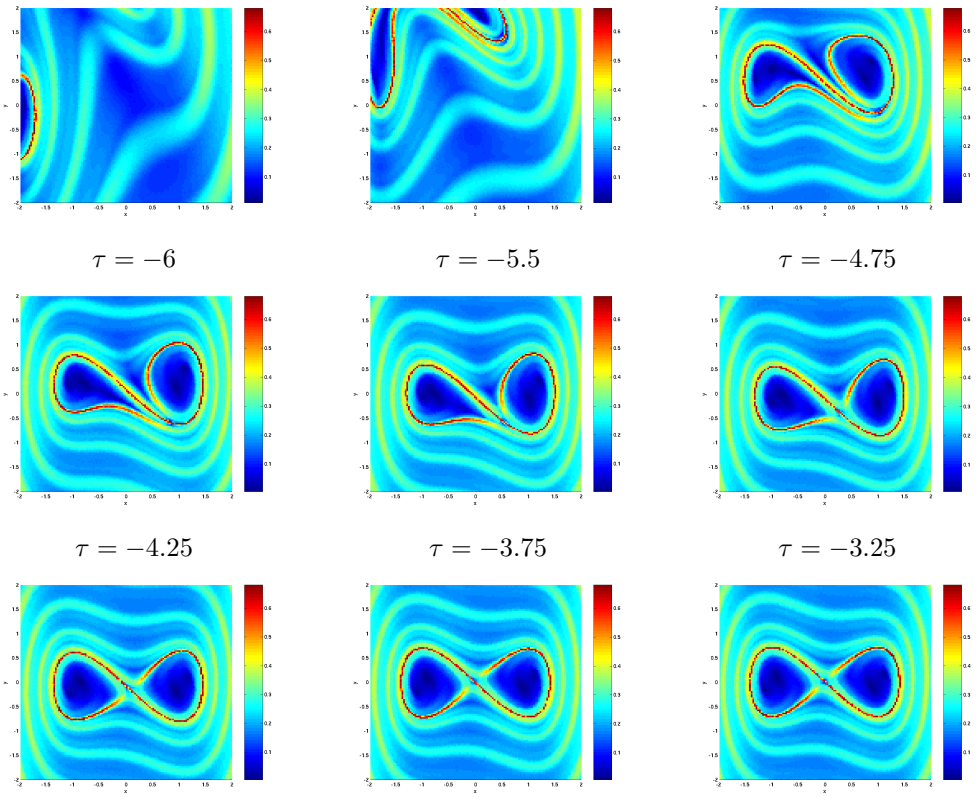

Figure 5.1: Direct expansion rates for the aperiodically forced Duffing oscillator with respect to different τ-fibers, choosing $T = 10$. For the computation 20 pairs of Monte Carlo points per box of initial distance $\varepsilon \approx 0.00156$ are used (16384 boxes).

We now show how the continuation algorithm can be used. We extract $A_{(0.5,5)}(0)$, carrying out six steps of the subdivision Algorithm 4.4.1. The choice of $\lambda = 0.5$ is motivated by the fact that for $t \geq 0$ the time dependence becomes increasingly negligible as the forcing decays exponentially. In the limit one would obtain an autonomous system with hyperbolic fixed point at the origin with Lyapunov exponents ± 1. So all points on the hyperbolic trajectory and its stable

manifold have a dominant Lyapunov exponent 1. However, as the trajectory is far off from zero for negative times (see Figure 5.1), for points on its stable manifold and rather short integration times we expect finite-time Lyapunov exponents to be smaller than one, converging to one for large integration times. The quantitative results presented in Figure 5.1 indicate that $\lambda = 0.5$ may be a reasonable choice.

We start with a box covering on depth 10. Each step of the algorithm consists of two subdivision steps and one selection step. The resulting covering (3801 boxes on depth 20) is shown in Figure 5.2 a). Based on this approximation we now want to compute $A_{(0.5,5)}(-4)$. For this we choose $T = 4$, $\lambda > 0.5$, $\tau = 0$, $\tilde{T} = 5$, $h = 1$ and $n = 5$ in Algorithm 5.2.6. Hence the box covering is mapped to the time slice at $\tau = -4$, where each box is discretized by 48 points uniformly distributed on its edges plus the center point. The continuation step yields a box collection of 7300 boxes on the -4-fiber, see Figure 5.2 b). In the first selection step 4942 boxes are discarded, in the second 1000, and in the third step only 30. For $k = 4$ all boxes are kept and we obtain a box covering of $A_{(0.5,5)}(-4)$ with 1328 boxes as shown in Figure 5.2 c). For comparison we also computed a covering of $A_{(0.5,5)}(-4)$ using the subdivision Algorithm 4.4.1 with the same set-up as described above for $\tau = 0$. The result is shown in Figure 5.2 d). Although this box covering consists of as many as 3822 boxes, it compares well qualitatively to the result obtained by the continuation algorithm.

The computational effort can be estimated in terms of the number of boxes for which expansion rates are computed, whereas the continuation step is negligible. Here the continuation algorithm is advantageous: instead of evaluating 15704 boxes (subdivision algorithm on the -4-fiber), in the continuation algorithm the expansion rates have to be computed for only 12344 boxes.

Double Gyre Flow

We consider the stream-function [102]

$$\Psi(x, y, t) = A \sin(\pi f(x, t)) \sin(\pi y),$$

where

$$f(x, t) = \epsilon \sin(\omega t) x^2 + (1 - 2\epsilon \sin(\omega t)) x.$$

With

$$\dot{x} = -\frac{\partial \Psi}{\partial y}(x, y, t) \tag{5.1}$$

$$\dot{y} = \frac{\partial \Psi}{\partial x}(x, y, t) \tag{5.2}$$

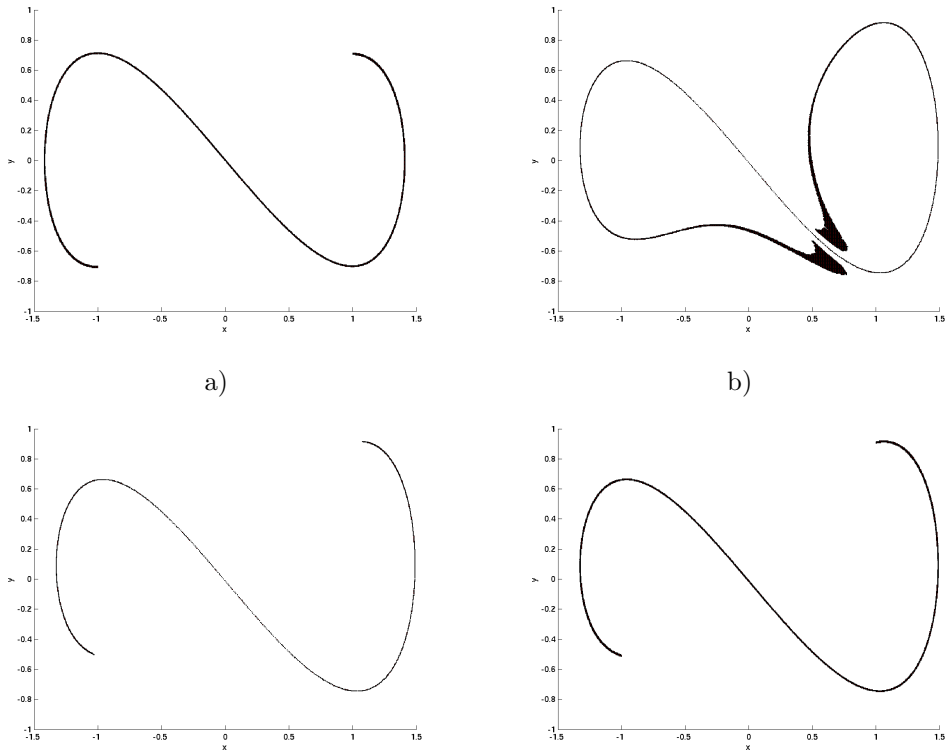

a) b)

c) d)

Figure 5.2: Continuation algorithm for the exponentially forced Duffing oscillator. a) Covering of $A_{(0.5,5)}(0)$ using the subdivision algorithm. b) Continuation step: box covering is mapped to past slice at $\tau = -4$. c) Box covering of $A_{(0.5,5)}(-4)$ after selection steps. d) Covering of $A_{(0.5,5)}(-4)$ using the subdivision algorithm.

we obtain the corresponding systems of differential equations

$$\dot{x} = -\pi A \sin(\pi f(x,t)) \cos(\pi y) \tag{5.3}$$

$$\dot{y} = \pi A \cos(\pi f(x,t)) \sin(\pi y) \frac{df}{dx}(x,t). \tag{5.4}$$

This can be seen as a periodically perturbed velocity field of a steady Rayleigh-Bénard flow.

For $\epsilon = 0$, it corresponds to an autonomous double-gyre pattern on a rectangle $[0,2] \times [0,1]$. For small $\epsilon \neq 0$ the instantaneous separation point moves along the x-axis with a period $\frac{2\pi}{\omega}$. For $t = 0$ the separation point is in the same position as in the autonomous case whereas for $t = \frac{\pi}{2\omega}$ the separation point is at its far right

position, see Figure 5.3 for an illustration of the velocity fields for fixed t. Note that the boundary of the rectangle is invariant.

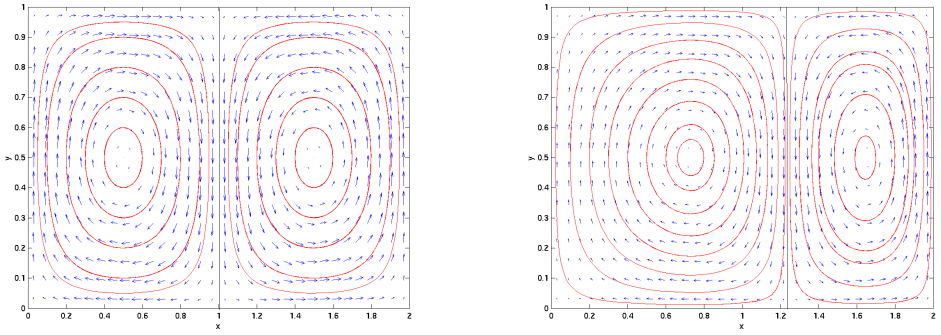

a) b)

Figure 5.3: Double gyre flow for $A = 1$,$\epsilon = 0.25$, $\omega = 2\pi$. a) Velocity field at $t = 0$; b) velocity field at $t = 0.25$.

In spite of its simple dynamics the invariant manifold structure with respect to the moving separation point is very complicated. To uncover this we fix $A = 1$, $\epsilon = 0.25$, $\omega = 2\pi$, making the flow periodic with period 1. We choose a box covering of the compact set $Q = [0, 2] \times [0, 1]$ on depth 14 (16384 boxes) and compute direct expansion rates using 20 pairs of Monte Carlo points of initial distance $\varepsilon \approx 0.0008$ (i.e. 20% of the box radius). These computations are done for different τ and T. The results are shown in Figure 5.4.

Moreover, an animation which illustrates the time-dependence of the structures of interest can be found at

`http://www-math.upb.de/~padberg/thesis.html`.

In order to illustrate the complicated manifold structure, we additionally approximate the unstable manifold. A superposition of parts of the stable and unstable manifold for a box covering on depth 16 (65536 boxes) is shown in Figure 5.5.

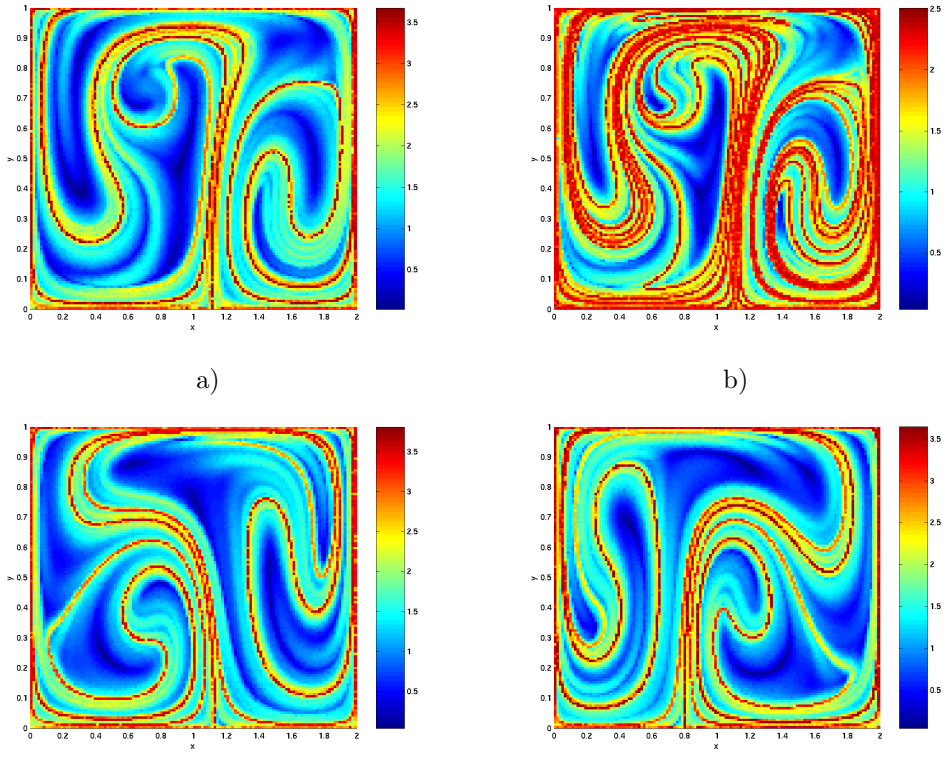

a) b)

c) d)

Figure 5.4: Direct expansion rates for the double gyre flow for $\epsilon = 0.25$, $\omega = 2\pi$ and $A = 1$ with respect to different τ-fibers and $T > 0$. For the computation 20 pairs of Monte Carlo points per box of initial distance $\varepsilon \approx 0.0008$ are used (16384 boxes). a) $\tau = 0$, $T = 2$; b) $\tau = 0$, $T = 3$; c) $\tau = 0.3$, $T = 2$; d) $\tau = 0.7$, $T = 2$.

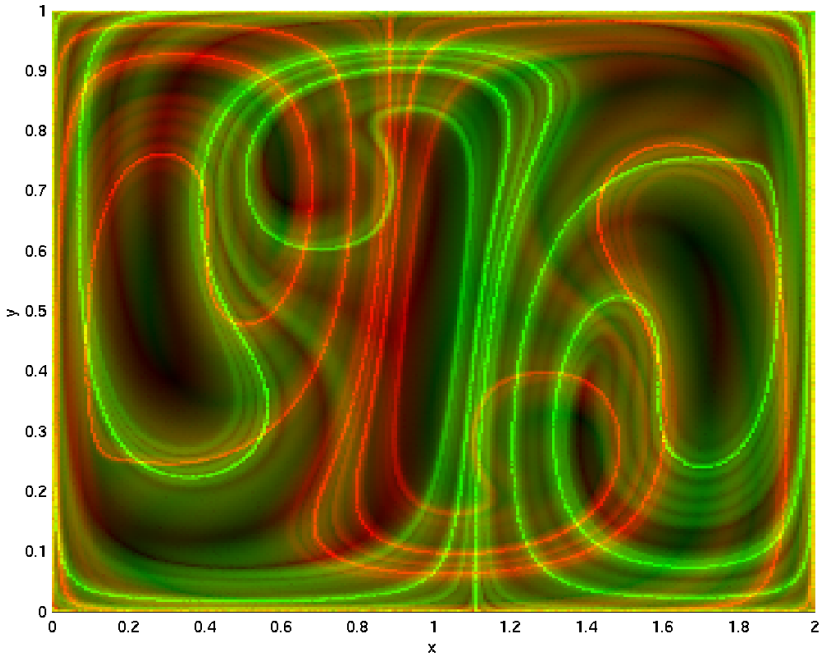

Figure 5.5: Stable (green) and unstable manifolds (red) in the double gyre flow for $\epsilon = 0.25$, $\omega = 2\pi$ and $A = 1$. Direct expansion rates for a box covering on depth 16 (65536 boxes), using 20 pairs of Monte Carlo points per box of initial distance $\varepsilon \approx 0.0004$. The direct expansion rates are computed for $\tau = 0$, $T = 2$ and $T = -2$.

5.3 Computation of Transport Rates

After relevant transport regions have been detected and approximated, another important task is to quantify the particle transport in terms of transport rates or transport probabilities. In the case of an area-preserving two-dimensional system one usually considers the evolution of lobes and computes the area of their intersection with the target region, see for example Coulliette and Wiggins [17], Miller et al. [84], or Lekien [74]. The accuracy of the boundary under time evolution can be ensured by point insertion techniques [74]. However, the estimation of areas often becomes difficult due to deformation and multiple intersections. For example, in Dellnitz, Junge, Koon, et al. [28] it was observed that the iteration of boundaries and lobes via a Poincaré map was only possible for a small number of iterates because of the increasingly complicated structure of the lobes. The extension of this method to higher dimensional systems is problematic for the same reason. Although considering lobe dynamics is also possible for systems that are not volume-preserving, it usually makes the analysis more difficult.

A different approach is to start with a number of test particles in the source set and to record how many of them reach the target region as a function of time, see for example Gabern et al. [39] for an application of such a Monte Carlo method to chemical physics, or Gladman et al. [41] for an example related to transport in the solar system. Note that these methods assume a uniform distribution of particles in the starting region, which often cannot be justified if it is comprised of regular and chaotic areas. Moreover, trajectories have to be computed for very long time intervals which is usually not desirable in the context of chaotic dynamics.

In Dellnitz, Junge, Koon et al. [28] a set oriented approach for the numerical detection of almost invariant sets via graph partitioning techniques is introduced. In this context transport rates are computed by directly using an approximation of the Perron-Frobenius operator, which is available from the already computed approximation of almost invariant sets. Moreover, estimates for the discretization error as well as on upper and lower bounds for the transport rate are derived. An application of this technique for the analysis of transport of Mars-Crossing asteroids is discussed in Dellnitz, Junge, Lo et al. [29]. Although the computation of the transition matrix is computationally expensive, it is important to note that it already contains all of the necessary information on the dynamics and so one avoids the approximation of long trajectories.

In this section we want to extend the results in Dellnitz, Junge, Koon et al. [28] to the context of non-autonomous dynamical systems. We define a time-dependent family of transfer operators which can be used to compute transport rates and probabilities between arbitrary sets of interest. In particular, our method is not restricted to the analysis of volume-preserving dynamical systems.

In addition, the use of boxes for the discretization of the phase space provides us with a natural setting for the efficient estimation of volumes even in higher dimensional systems.

To provide a detailed theoretical justification of our approach we also derive error estimates which improve the results described in [28]. This gives us also estimates of upper and lower bounds on the transport rate. Moreover, we propose an adaptive approach for the reduction of the error generalizing the techniques introduced in [28].

The method is illustrated by two examples. First we consider a Rossby Wave Flow with aperiodic forcing [78]. Then we compute scattering rates for a Rydberg atom in crossed magnetic and electric fields [22, 39, 59]. Although this is an example of an autonomous system, the results demonstrate the strength of the adaptive method.

An application of these techniques in the context of analyzing transport in ocean flows is presented in Chapter 6. Here we compute transport rates from near shore areas to regions in the open sea west of Monterey Bay.

5.3.1 A Transfer Operator Approach

We now want to derive a general framework for the computation of transport rates in time-dependent dynamical systems. The following description closely follows that in [28], where the autonomous case has been treated. Let

$$f_k : M \to M,\ k \in \mathbb{Z},\ x_{k+1} = f_k(x_k),$$

be a family of maps and define

$$f_{[k,l]} := f_{l-1} \circ f_{l-2} \circ \cdots \circ f_k \text{ for } k < l \text{ and } f_{[k,k]} = Id.$$

So $f_{[k,l]}$ maps a point $x_k \in M$ at time k to some point x_l at time l. Let $U_1(k), \ldots, U_{n_k}(k) \subset M$ a partition of M into n_k regions at time k. Let m denote the Lebesgue measure on M. We are interested in the **transport probability**

$$p(R(k), S(l)) = \frac{m(f_{[k,l]}^{-1}(S(l)) \cap R(k))}{m(R(k))},$$

that is the (conditional) probability that a particle initialized in some region $R(k)$ at time k is transported to the region $S(l)$ at time l. We denote by

$$T(R(k), S(l)) := m(f_{[k,l]}^{-1}(S(l)) \cap R(k))$$

the **transport rate**, that is, the volume of particles in $R(k)$ that is mapped to $S(l)$.

Obviously, the quantification of transport is a question about the evolution of densities or measures on M.

The evolution of a (signed) measure ν on M can be described in terms of the *transfer operator* (or *Perron–Frobenius operator*) associated with f_k. In our setting this is a family of linear operators $P_k : \mathcal{M} \to \mathcal{M}$,

$$(P_k\nu)(A) = \nu(f_{k-1}^{-1}(A)), \quad A \text{ measurable},$$

on the space $\mathcal{M}$ of signed measures on M. We denote by

$$(P_{[k,l]}\nu)(A) = \nu(f_{[k,l]}^{-1}(A)) = \nu(f_k^{-1} \circ f_{k+1}^{-1} \circ \cdots f_{l-1}^{-1}(A))$$

the transfer operator associated with $f_{[k,l]}$. Note that $P_{[k,l]}$ is a cocycle:

1. $P_{[k,k]} = I$,
2. $P_{[l,k]} \circ P_{[m,l]} = P_{[m,k]}$.

This operator concept relates directly to the transport quantities of interest:

Corollary 5.3.1 *Let $m_{R(j)} \in \mathcal{M}$ be the measure $m_{R(j)}(A) = m(A \cap R(j)) = \int_A \chi_{R(j)}\, dm$, where $\chi_{R(j)}$ denotes the indicator function on the region $R(j)$ at time j. Then*

$$T(R(k), S(l)) = (P_{[k,l]}m_{R(k)})(S(l)) = m(f_{[k,l]}^{-1}(S(l)) \cap R(k)). \tag{5.5}$$

Evidently, since we are interested in actually computing the quantities of interest, we need to explicitly deal with the transfer operator. Since an analytical expression for it will usually not be available, we need to derive a finite dimensional approximation to it.

Discretization of Transfer Operators. As a finite dimensional space $\mathcal{M}_\mathcal{B}$ of measures on M we consider the space of absolutely continuous measures with density $h \in \Delta_\mathcal{B} := \operatorname{span}\{\chi_B : B \in \mathcal{B}\}$, being piecewise constant on the elements of the partition $\mathcal{B}$. Let $Q_\mathcal{B} : L^1 \to \Delta_\mathcal{B}$ be the projection

$$Q_\mathcal{B}h = \sum_{B\in\mathcal{B}} \frac{1}{m(B)} \int_B h\, dm\, \chi_B.$$

Then for every set A that is the union of partition elements we have

$$\int_A Q_\mathcal{B}h\, dm = \int_A h\, dm. \tag{5.6}$$

For the following statements suppose that the partition $\mathcal{B}$ of M into boxes is time-independent. Then the Galerkin projection (see e.g. Junge [64]) $Q_{\mathcal{B}}$ of the transfer operator is also independent of k. Hence a discretization of the transfer operator $P_{[k,l]}$ with respect to the box collection $\mathcal{B}$ is given in terms of a transition matrix (p_{ij}) as introduced in Chapter 4 (Equation 4.3, see also [107]):

$$p_{ij} = \frac{m(f_{[k,l]}^{-1}(B_i) \cap B_j)}{m(B_j)}, \; i,j = 1,\ldots,n.$$

For a detailed discussion on the projection and discretization we refer to Junge [64].

Approximation of Transport Rates. Note that we can write

$$T(R(k), S(l)) = \int_{S(l)} P_{[k,l]} \chi_{R(k)} \, dm.$$

For some measurable set A let

$$\underline{A} = \bigcup_{B \in \mathcal{B}: B \subset A} B \quad \text{and} \quad \overline{A} = \bigcup_{B \in \mathcal{B}: B \cap A \neq \emptyset} B,$$

see Figure 5.6 for an illustration.

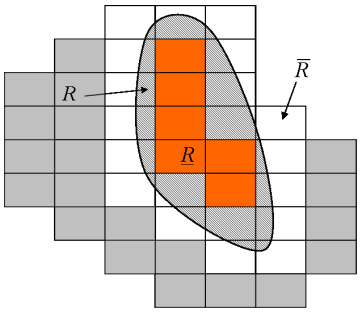

Figure 5.6: The sets $\underline{R}$ and $\overline{R}$ of a region R. The volume of the boundary boxes is one major contributor to the error in computing transport rates.

Since $P_{[k,l]}$ is positive, we get the following estimate.

Proposition 5.3.2 *The transport rate $T(R(k), S(l))$ is bounded by the following integrals:*

$$\int_{\underline{S}(l)} P_{[k,l]} \chi_{\underline{R}(k)} \, dm \leq T(R(k), S(l)) \leq \int_{\overline{S}(l)} P_{[k,l]} \chi_{\overline{R}(k)} \, dm. \tag{5.7}$$

The next step is to replace $P_{[k,l]}$ by $Q_{\mathcal{B}}P_{[k,l]}$, which is the discretized transfer operator. This is a transition matrix, which will be denoted by $\tilde{P}_{[k,l]}$. The error in making such a replacement is given by the estimate in the following Lemma.

Lemma 5.3.3 *Let $R := R(k), S := S(l) \subset M$. Then*

$$\begin{aligned}&\left|\int_S P_{[k,l]}\chi_R \, dm - \int_S Q_{\mathcal{B}}P_{[k,l]}\chi_R \, dm\right| \\ &\leq \max\left\{m\left(f_{[k,l]}^{-1}(S \setminus \underline{S}) \cap R\right), m\left(f_{[k,l]}^{-1}(\overline{S} \setminus S) \cap R\right)\right\}.\end{aligned}$$

Proof: Using Equation (5.6) and the fact that

$$\int_{\underline{S}} Q_{\mathcal{B}}P_{[k,l]}\chi_R \, dm \leq \int_S Q_{\mathcal{B}}P_{[k,l]}\chi_R \, dm \leq \int_{\overline{S}} Q_{\mathcal{B}}P_{[k,l]}\chi_R \, dm \tag{5.8}$$

we get

$$\begin{aligned}&\int_S P_{[k,l]}\chi_R \, dm - \int_S Q_{\mathcal{B}}P_{[k,l]}\chi_R \, dm \\ &\leq m\left(f_{[k,l]}^{-1}(S) \cap R\right) - \int_{\underline{S}} Q_{\mathcal{B}}P_{[k,l]}\chi_R \, dm \\ &= m\left(f_{[k,l]}^{-1}(S) \cap R\right) - \int_{\underline{S}} P_{[k,l]}\chi_R \, dm \\ &= m\left(f_{[k,l]}^{-1}(S) \cap R\right) - m\left(f_{[k,l]}^{-1}(\underline{S}) \cap R\right) \\ &= m\left(f_{[k,l]}^{-1}(S \setminus \underline{S}) \cap R\right).\end{aligned}$$

Similarly we obtain

$$\int_S Q_{\mathcal{B}}P_{[k,l]}\chi_R \, dm - \int_S P_{[k,l]}\chi_R \, dm \leq m\left(f_{[k,l]}^{-1}(\overline{S} \setminus S) \cap R\right),$$

which gives the desired statement. □

So the boxes that contribute the most to the error are those that contain preimages of the boundary of the target set $S(l)$.

However, the statement above is a theoretical result. Usually, it is not desirable to deal with the transition matrix $\tilde{P}_{[k,l]}$, as for this one needs to compute long parts of orbits. Instead we work with

$$P_{[k,l]_{\mathcal{B}}} := \tilde{P}_{[l-1,l]} \cdot \tilde{P}_{[l-2,l-1]} \cdots \tilde{P}_{[k,k+1]},$$

which is the product of "one-step" transition matrices, forming a cocycle.

The following Lemma gives a bound on the error:

Lemma 5.3.4 *Let $R := R(k), S := S(l) \subset M$ and*

$$S_l = S, \quad S_{n-1} = f_{n-1}^{-1}(\overline{S_n}), \quad n = l, l-1, \ldots, k+1;$$

and

$$s_l = S, \quad s_{n-1} = f_{n-1}^{-1}(\underline{s_n}), \quad n = l, l-1, \ldots, k+1.$$

Then

$$\begin{aligned}
&\left| \int_S P_{[k,l]} \chi_R \, dm - \int_S P_{[k,l]_{\mathcal{B}}} \chi_R \, dm \right| \\
&\leq \max \left\{ m \left(f_{[k,l]}^{-1}(S \setminus \underline{S}) \cap R \right), m \left(f_{[k,l]}^{-1}(\overline{S} \setminus S) \cap R \right) \right\} \\
&+ \max \left\{ m \left((S_k \setminus f_{[k,l]}^{-1}(\underline{S})) \cap R \right), m \left((f_{[k,l]}^{-1}(\overline{S}) \setminus s_k) \cap R \right) \right\}.
\end{aligned}$$

Proof:

$$\begin{aligned}
&\left| \int_S P_{[k,l]} \chi_R \, dm - \int_S P_{[k,l]_{\mathcal{B}}} \chi_R \, dm \right| \\
&\leq \left| \int_S (P_{[k,l]} - Q_{\mathcal{B}} P_{[k,l]}) \chi_R \, dm \right| + \left| \int_S (Q_{\mathcal{B}} P_{[k,l]} - P_{[k,l]_{\mathcal{B}}}) \chi_R \, dm \right|.
\end{aligned}$$

An error estimate for the first term on the right hand side is provided by the previous Lemma. Hence it remains to show that

$$\begin{aligned}
&\left| \int_S (Q_{\mathcal{B}} P_{[k,l]} - P_{[k,l]_{\mathcal{B}}}) \chi_R \, d\mu \right| \\
&\leq \max \left\{ m \left((S_k \setminus f_{[k,l]}^{-1}(\underline{S})) \cap R \right), m \left((f_{[k,l]}^{-1}(\overline{S}) \setminus s_k) \cap R \right) \right\}.
\end{aligned}$$

Obviously one has

$$m\left(s_k \cap R\right) \leq \int_S P_{[k,l]_{\mathcal{B}}} \chi_R \, dm \leq m\left(S_k \cap R\right).$$

Hence, using this estimate as well as Equations (5.6) and (5.8) we obtain

$$\begin{aligned}
&\int_S (Q_{\mathcal{B}} P_{[k,l]} - P_{[k,l]_{\mathcal{B}}}) \chi_R \, dm \\
&\leq \int_{\overline{S}} Q_{\mathcal{B}} P_{[k,l]} \chi_R \, dm - m\left(s_k \cap R\right) \\
&= m \left(f_{[k,l]}^{-1}(\overline{S}) \cap R \right) - m\left(s_k \cap R\right) \\
&= m \left((f_{[k,l]}^{-1}(\overline{S}) \setminus s_k) \cap R \right)
\end{aligned}$$

and similarly

$$\int_S (P_{[k,l]_{\mathcal{B}}} - Q_{\mathcal{B}} P_{[k,l]}) \chi_R \, dm \leq m\left((S_k \setminus f_{[k,l]}^{-1}(\underline{S})) \cap R \right),$$

which gives the desired result. □

Note that this error statement is an improvement of a similar one in [28], as here, setting $n = l - k$, the error stays bounded for $n \to \infty$.

Using Proposition 5.3.2 and Lemma 5.3.4 we obtain the following estimate on the error between the true transport rate $T(R(k), S(l))$ and its approximation. To abbreviate the notation, let $\underline{e_R}, \overline{e_R}, \underline{u_R}$ and $\overline{u_R} \in \mathbb{R}^b$ be defined by

$$(\underline{e_R})_i = \begin{cases} 1, & \text{if } B_i \subset R, \\ 0, & \text{else} \end{cases}, \quad (\overline{e_R})_i = \begin{cases} 1, & \text{if } B_i \cap R \neq \emptyset, \\ 0, & \text{else} \end{cases}$$

and

$$(\underline{u_R})_i = \begin{cases} m(B_i), & \text{if } B_i \subset R, \\ 0, & \text{else,} \end{cases}, (\overline{u_R})_i = \begin{cases} m(B_i), & \text{if } B_i \cap R \neq \emptyset, \\ 0, & \text{else,} \end{cases},$$

where $i = 1, \ldots, b$.

Lemma 5.3.5 *Let $R := R(k), S := S(l) \subset M$,*

$$S_l = S(l), \quad S_{n-1} = f_{n-1}^{-1}(\overline{S_n}), \quad n = l, l-1, \ldots, k+1;$$

and

$$s_l = S(l), \quad s_{n-1} = f_{n-1}^{-1}(\underline{s_n}), \quad n = l, l-1, \ldots, k+1.$$

Then

$$\begin{aligned} &\left| T(R(k), S(l)) - \underline{e_S}^T P_{[k,l]_{\mathcal{B}}} \, \underline{u_R} \right| \\ &\leq \underline{e_S}^T P_{[k,l]_{\mathcal{B}}} (\overline{u_R} - \underline{u_R}) + (\overline{e_S} - \underline{e_S})^T P_{[k,l]_{\mathcal{B}}} \overline{u_R} \\ &+ \max\left\{ m\left(f_{[k,l]}^{-1}(S \setminus \underline{S}) \cap R \right), m\left(f_{[k,l]}^{-1}(\overline{S} \setminus S) \cap R \right) \right\} \\ &+ \max\left\{ m\left((S_k \setminus f_{[k,l]}^{-1}(\underline{S})) \cap R \right), m\left((f_{[k,l]}^{-1}(\overline{S}) \setminus s_k) \cap R \right) \right\}. \end{aligned}$$

Proof: The proof follows directly from Proposition 5.3.2 and Lemma 5.3.4, see also [28]. Note that an analogous statement can be obtained to estimate the error

$$\left| T(R(k), S(l)) - \overline{e_S}^T P_{[k,l]_{\mathcal{B}}} \, \overline{u_R} \right|.$$

□

This estimate gives a bound on the error between the true transport rate $T(R(k), S(l))$ and $\underline{e_S}^T P_{[k,l]_\mathcal{B}} \ \underline{u_R}$, that is the one computed via the transition matrix. Major contributors to the error are not only the elements of the fine partition $\mathcal{B}$ that intersect the boundaries of $R(k)$ and $S(l)$ but also boxes that contain preimages of the boundary of $S(l)$. So an obvious consequence of Lemma 5.3.5 is that in order to ensure a certain degree of accuracy of the transport rates, these boxes need to be refined.

Notably, the numerical effort to compute the approximate transport rate $\underline{e_S}^T P_{[k,l]_\mathcal{B}} \ \underline{u_R} = \underline{e_S}^T \tilde{P}_{[l-1,l]} \tilde{P}_{[l-2,l-1]} \cdots \tilde{P}_{[k,k+1]} \ \underline{u_R}$ essentially consists in $n = l - k$ matrix-vector-multiplications – where the matrices $\tilde{P}_{[i,i+1]}$ are sparse.

Convergence. Using Lemma 5.3.5 one can show convergence for the approximate transport rate to the true transport rate if the diameter of the boxes in the covering goes to zero. See [28] for the convergence statement in the autonomous setting and a proof.

Autonomous transport. If the dynamical system under consideration is autonomous or given as the Poincaré return map of a time-periodic dynamical system, the above statements simplify such that one has only to deal with powers of a single time-independent transition matrix $P_\mathcal{B}$. Note that the statements above also hold for the autonomous case. The autonomous framework with slightly different results is described in detail in [28].

Adaptive refinement of box covering As shown above, those boxes contribute considerably to the error that either map onto the boundary of the target set or whose preimage lie on the boundary of the source set. Hence, the adaptive approach in [28] needs to be refined.

Let $R := R(k), S := S(l) \subset M$ with $n := l - k > 0$. We propose the following algorithm:

Algorithm 5.3.6 Let $\mathcal{B}$ be a box covering of M. Let $N := \lceil \frac{n}{2} \rceil$ and let $P_{[k,l]_\mathcal{B}}$ be the product of transition matrices as defined above.

Determine the boundary boxes:

$$b_R := \overline{R} \setminus \underline{R},$$
$$b_S := \overline{S} \setminus \underline{S},$$

and compute

$$\underline{T(R,S)} := \underline{e_S}^T P_{[k,l]_\mathcal{B}} \ \underline{u_R},$$
$$\overline{T(R,S)} := \overline{e_S}^T P_{[k,l]_\mathcal{B}}; \ \overline{u_R},$$

the *numerical* lower and upper bound on the transport rate $T(R(k), S(l))$ respectively. Choose $J \in \mathbb{N}$.

1. For $j = 1, \ldots, J$:
2. Mark all boxes B for which

$$f_{[l-i,l]}(B) \cap b_S \neq \emptyset \text{ for } i \in \{1, \ldots, N\}$$

   or

$$f^{-1}_{[k,k+i]}(B) \cap b_R \neq \emptyset \text{ for } i \in \{1, \ldots, N\}.$$

   (This information is coded in the transition matrices.)
3. Subdivide marked boxes.
4. Compute $P_{[k,l]_{\mathcal{B}}}$.
5. Determine b_R, b_S, $\underline{T(R,S)}$, and $\overline{T(R,S)}$.

The algorithm produces an adaptive covering, refining especially those boxes that contribute to the error in computing the transport rates. Moreover, the algorithm gives an upper and lower bound to the transport rate, at least up to the error estimated in Lemma 5.3.5.

5.3.2 Examples

In order to illustrate the methods we first consider the example of a Rossby Wave flow which is a non-autonomous system. The second application is from physical chemistry, where ionization rates for the Rydberg atom in crossed fields are computed.

Rossby Wave Flow

We first consider a transport example constructed from a Rossby Wave Flow with non-decaying aperiodic disturbance as suggested by Malhotra and Wiggins [78]. The velocity field is given by

$$\begin{aligned} \dot{x} &= c - \sin(x)\cos(y) - \epsilon \frac{\partial f}{\partial y}(x, y, t), \\ \dot{y} &= \cos(x)\sin(y) + \epsilon \frac{\partial f}{\partial x}(x, y, t). \end{aligned}$$

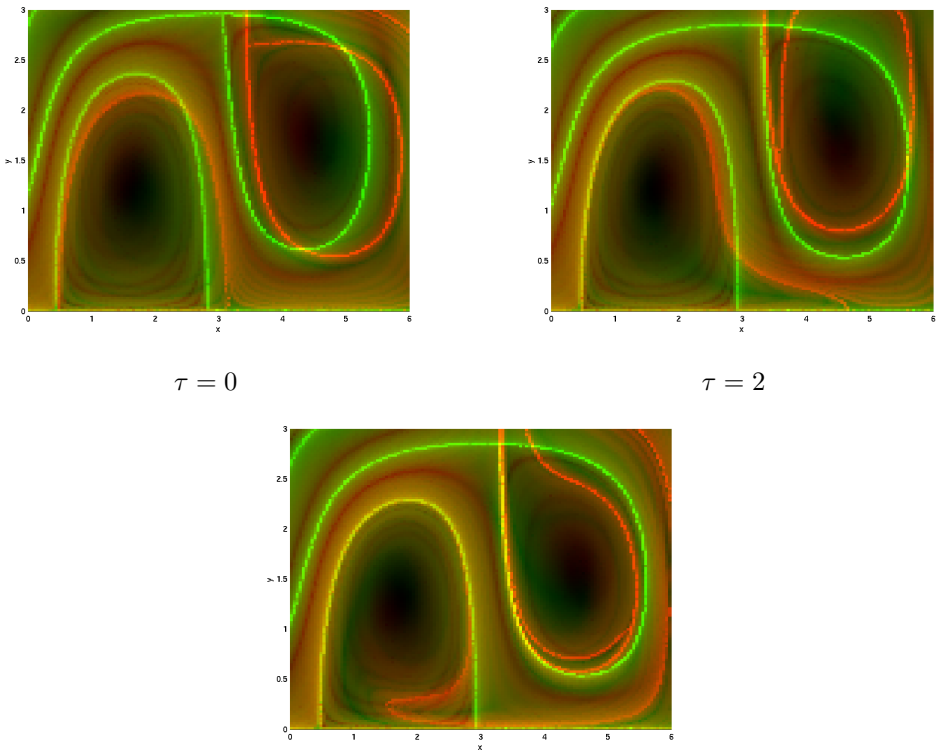

Figure 5.7: Crossings of stable (green) and unstable manifold (red) in the Rossby Wave Flow. Direct expansion rates (20 pairs of points) for $\tau = 0$ and $T = 30$ and $T = -30$, respectively. Note in particular the deformation of the unstable manifold as time increases.

with constants $c = 0.5$ and $\epsilon = 0.1$. The aperiodic disturbance is chosen as $f(x, y, t) = -\frac{1}{2}xy \tanh^2 2t$. It causes the pathological nature of the manifolds crossing, see Figure 5.7, and the creation of a finite and small number of lobes.

In order to test our algorithms we construct the following transport problem: we fix a box $S(l)$ and are interested in the transport rate of points that are initialized in the region $R(0)$ bounded by the unstable manifold at $\tau = 0$ as shown in Figure 5.8. The deformation of the manifold is such that parts of the interior region will have a nonempty intersection with the target box as time increases.

In order to describe our results in the framework introduced above, we choose non-autonomous maps f_k, $k \in \mathbb{Z}$, by $f_k := \varphi^{k+1,k}$, that is, time-1 maps of the evolution. We consider $Q = [0, 6] \times [0, 3]$ and start with a partition on depth 14

(16384 boxes) as shown in Figure 5.8.

We want to compute transport rates $T(R(0), S(l))$ for $l = 1, \ldots, 6$. Note that in spite of the notation $S(l)$ is time-independent. As we have extracted $R(0)$ numerically, we only know the respective box coverings $\underline{R(0)}$ and $\overline{R(0)}$, whereas $S(l)$ is directly chosen as a set of boxes.

As the f_k are area-preserving, we can compute an upper and lower bound on the transport rate using a straight-forward approach. We map the boundary boxes, the yellow boxes in Figure 5.8, by $f_{[0,l]}$ using 48 points on the edges of each box plus the center point. For different l we compute the area of the intersection with the target set. As a lower bound we consider the area that is bounded by images of the boundary boxes excluding the boundary, as an upper bound we use the area bounded by images of boundary boxes inclusive of the boundary. The results are shown in Figure 5.9 a).

In order to show how our methods work, we compute the l-step transition matrices $\tilde{P}_{[0,l]}$ as well as $P_{[0,l]_{\mathcal{B}}} = \tilde{P}_{[l-1,l]} \cdot \tilde{P}_{[l-2,l-1]} \cdot \ldots \cdot \tilde{P}_{[0,1]}$ using 100 grid points per box. The different results for the numerical upper and lower bounds as a function of l are given in Figure 5.9 b). We observe, that the results for $P_{[0,l]_{\mathcal{B}}}$ are very close to the transport rates based on the l-step transition matrix $\tilde{P}_{[0,l]}$. Moreover, the bounds on the transport rates appear much tighter than using the naive approach, see Figure 5.9 a). This is due to the fact that using the transition matrices the transport probabilities for every single box are considered, that means that only the fraction of its volume that is transported to the target set is taken into account. On the other hand, in the simple straight-forward computation the entire volume of a transport box is considered.

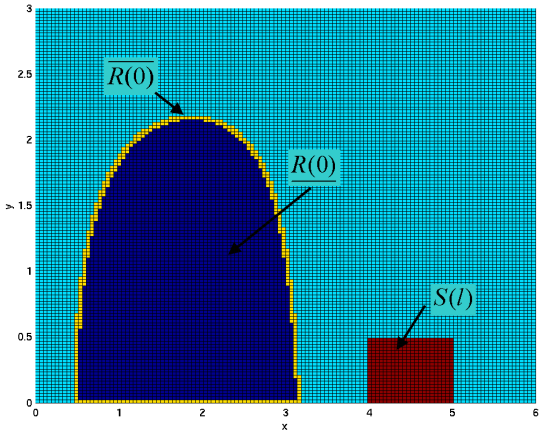

Figure 5.8: Box partition of phase space for the transport problem in the Rossby wave flow on depth 14 (16384 boxes).

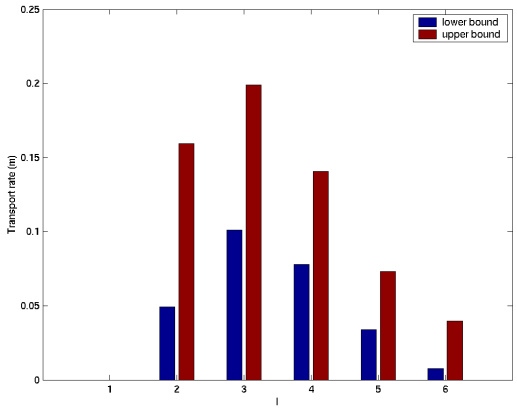

a)

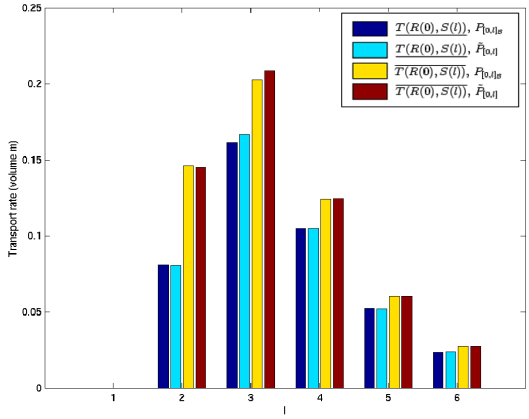

b)

Figure 5.9: Upper and lower bound on transport rates for different final times l. a) Naive approach. b) Estimates computed using the transition matrix $P_{[0,l]_{\mathcal{B}}}$ as well as $\tilde{P}_{[0,l]}$.

In order to test the adaptive approach, we choose a covering on depth 10 (1024 boxes), but we refine the boundary boxes (depth 14). Then the adaptive approach is employed for different numbers of steps $J = \{1, \ldots, 4\}$. As our boundary (yellow) is only known for a box level on depth 14, it does not make sense to refine these boxes within the subdivision algorithm. This would only mean additional computational effort without gaining new information. So with the adaptive method, we obtain a box covering on depth 10/14 (this means that some boxes are at depth 10 and others at finer levels, where 14 is the maximum), see Figure 5.10 a). The results for an approximation of $p(R(0), S(l))$ in terms of

$\underline{T(R(0), S(l))/m(R(0))}$ are given in Figure 5.10 b). Note that the results for the adaptive approach compare well to the non-adaptive approach, though the former is computationally advantageous, as the covering consists only of 6206 boxes.

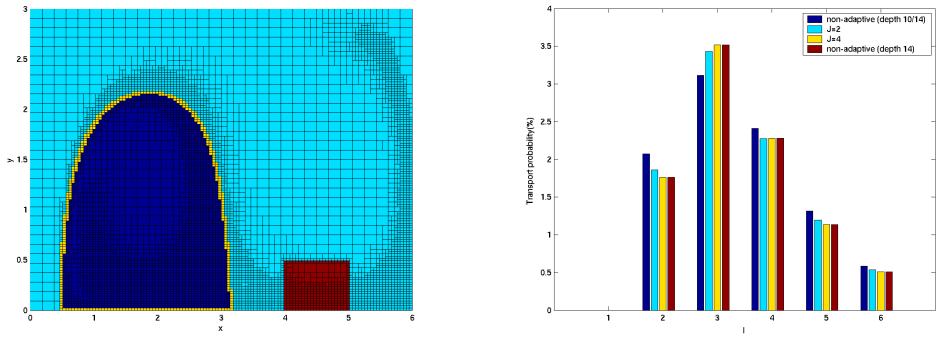

a) b)

Figure 5.10: a) Adaptive partition of phase space for the transport problem on depth 10/14, choosing $J = 4$ in the adaptive Algorithm 5.3.6 (6206 boxes). b) Transport probabilities with respect to a box covering on depth 10/14 and for different choices of J in Algorithm 5.3.6. For comparison also the results for the original covering on depth 14 (see Figure 5.8) are shown.

Ionization of the Rydberg atom

We now consider an autonomous dynamical system and describe a model from chemical physics. The ionization of a Rydberg atom interacting with crossed electric and magnetic fields resembles a unimolecular chemical reaction. The activation previous to reaction is given by the initial excitation of a single electron to a high energy level in such a way that its dynamics can be described using classical physics. The reaction itself is given when the energy flows through the ionization channel and the electron is detached, see for example [22, 39, 59].

In the following paragraphs we will deal with the planar Rydberg problem. For a more detailed description, we refer to the recent work by Dellnitz et al. [22], where we have also analyzed a higher-dimensional model using set oriented methods.

The planar Rydberg model is described by the following classical Hamiltonian:

$$H = \frac{1}{2}(p_x^2 + p_y^2) - \frac{1}{r} + \frac{1}{2}(xp_y - yp_x) + \frac{1}{8}(x^2 + y^2) - \epsilon x,$$

where $r = \sqrt{x^2 + y^2}$ is the distance from the electron to the nucleus of the atom and ϵ is the scaled electric field. The equations of motion are given as

$$\begin{aligned} \ddot{x} &= -\frac{x}{r^3} - \dot{y} + \epsilon \\ \ddot{y} &= -\frac{y}{r^3} + \dot{x}. \end{aligned}$$

The energy in terms of positions and velocities is

$$E(x, y, \dot{x}, \dot{y}) = \frac{1}{2}(\dot{x}^2 + \dot{y}^2) - \epsilon x - \frac{1}{r}.$$

The system has a unique fixed point, commonly known as the Stark Saddle Point, at $x = \frac{1}{\sqrt{\epsilon}}$ and $y = \dot{x} = \dot{y} = 0$. The energy of the fixed point is $E = -2\sqrt{\epsilon}$ and it is the threshold value for the ionization to be possible.

We choose $\epsilon = 0.57765$ and we fix an energy level that allows ionization, in our case $E = -1.52$. Hence, the position space (x, y) looks as sketched in Figure 5.11.

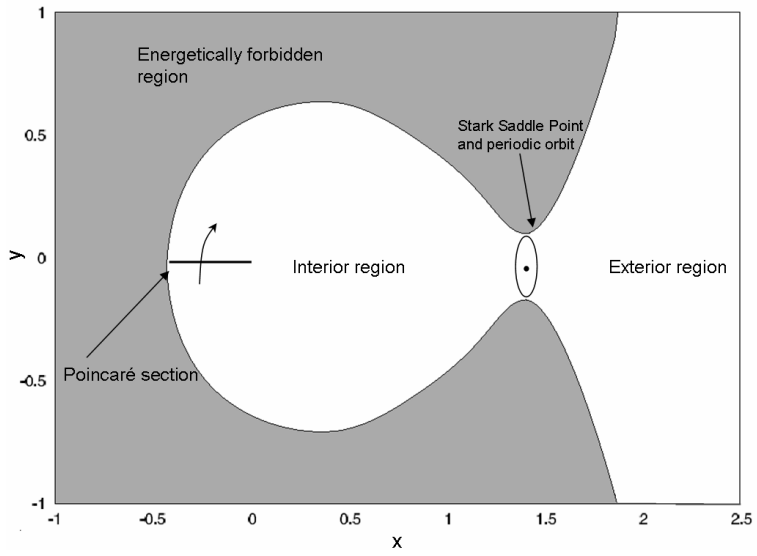

Figure 5.11: The planar Rydberg problem. Sketch of the position space at an energy level allowing ionization.

The grey part is energetically not permissable, the interior corresponds to the situation where the electron is attached, the exterior where the electron is detached. The fixed point is located in the gateway between the two regions of interest. As the fixed point is of type *saddle*×*center*, there exists a normally hyperbolic invariant manifold, a periodic orbit in our planar case. Its stable and

unstable manifolds, the so-called tubes provide the only dynamically possible way between the interior (electron attached) and the exterior (electron detached) regions and completely explain the transport mechanism; see also [39, 42, 71, 92].

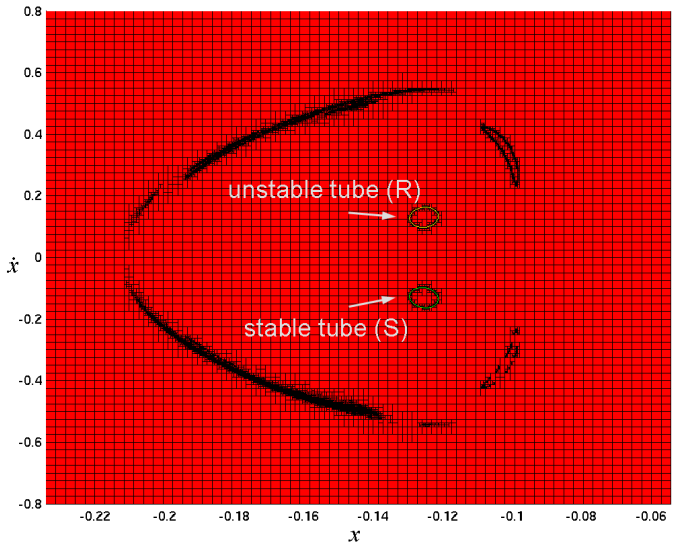

Figure 5.12: Adaptive box covering of Poincaré surface in the interior region (see Figure 5.11) using Algorithm 5.3.6 with $J = 10$. Also shown are the first intersections of the stable and unstable tubes with the Poincaré section.

We define a Poincaré section in the interior region by $y = 0$, $\dot{y} > 0$, and $x < 0$. The tubes, that is, the stable and unstable manifold of the periodic orbit around the Stark Saddle Point, intersect the Poincaré section infinitely often; see Figure 5.12 for the first intersection. Note that the resulting map is not area preserving as points are mapped out through the stable tube.

We want to compute the transport rate from the unstable to the stable tube intersection. This corresponds to the capture of an electron and its subsequent ionization, also known as the full-scattering problem. The transport mechanism for this Poincaré map is such that the particles are mapped from one tube intersection of the unstable tube with the Poincaré section to the next until the unstable and the stable tubes intersect, enabling particles to leave. In our setting, we use information on the exact location of the first tube intersections only to define a source and a target set. The data is obtained from a computation of the stable and unstable manifolds of the hyperbolic periodic orbit in the full 4-dimensional phase space and has been provided by F. Gabern and S. Ross.

Unlike the situation in [28] particles are not transported from the source to the target set within one iteration of the Poincaré map, but we need at least

five iterates to observe a positive transport rate. So we need to make sure that $P_{[0,k]_{\mathcal{B}}} = P_{\mathcal{B}}^k$, where $k \geq 5$, is approximated as correctly as possible.

We start with a box covering of $Q = [-0.235, -0.055] \times [-0.8, 0.8]$ on depth 12, with the boxes containing the tube intersections on depth 24 (7640 boxes). We choose $N = 3$, carry out $J = 10$ steps of the adaptive refinement Algorithm 5.3.6 and obtain a covering consisting of 27640 boxes. For the computation of the transition matrix 100 grid points are used. The resulting box covering ($J = 10$) is shown in Figure 5.12; observe how nicely further intersections of tubes are picked up. The scattering probabilities are approximated by $\underline{e_S} P_{\mathcal{B}}^k \underline{u_R}$. The transport probabilities as a function of k for different box coverings obtained within the adaptive approach for $J \in \{1, \ldots, 10\}$ are given in Figure 5.13.

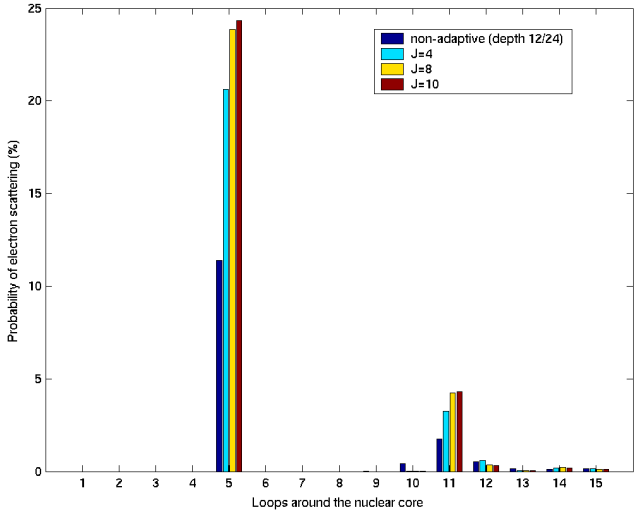

Figure 5.13: Scattering probabilities for different levels of refinement of the transport boxes. J is the number of steps in the adaptive Algorithm 5.3.6.

Observe the impact that the refinement of the transport boxes (not the boundary boxes) has on the probabilities. We remark that the quantitative results compare well to other approaches [40, 39, 59]. As pointed out in [39], the non-monotonicity of the scattering profile has been observed in similar problems in chemistry.

Chapter 6

Application to Ocean Flows

6.1 Introduction

As one of the five major upwelling regions in the world the central California coast has received considerable oceanographic study. Upwelling is a phenomenon where cold nutrient-rich water is driven to the surface due to wind, the angle of the coastline, and the rotation of the earth. This upwelled water occurs as a cool band along the coast, separated from warmer offshore waters by a variable series of fronts, plumes and eddies. Upwelled water supports high levels of phytoplankton, which forms the basis of the food chain for all marine animals. In this context, the oceanography of Monterey Bay, a deep embayment in central California, has received considerable study in the last few years [14, 81].

For example, the Office for Naval Research sponsored Autonomous Ocean Sampling Network II project [2] (AOSN II) as well as its successor Adaptive Sampling and Prediction (ASAP) [4] have the objective to integrate sophisticated platforms and techniques to better observe and predict the ocean. In particular, the analysis of the upwelling event has been one of the major goals of these projects. Within the AOSN II field experiment in Monterey Bay in summer 2003 geophysical data has been obtained during the upwelling period through different sensing devices such as autonomous underwater vehicles, ships, aircraft, as well as high frequency radar arrays; see Figure 6.1 for an illustration.

In this context, the analysis of the velocity data with the purpose to extract Lagrangian coherent structures (LCS) plays an important role. These objects are defined as ridges in the scalar finite-time Lyapunov exponent field [102], see also Chapter 5. For example, numerical evidence shows that LCS often correspond to temperature fronts [74]. Moreover, the knowledge of these structures is useful when optimizing the trajectories of underwater gliders [57] or the distribution of sensors [105]. It is realistic to assume that approximate ocean forecasts

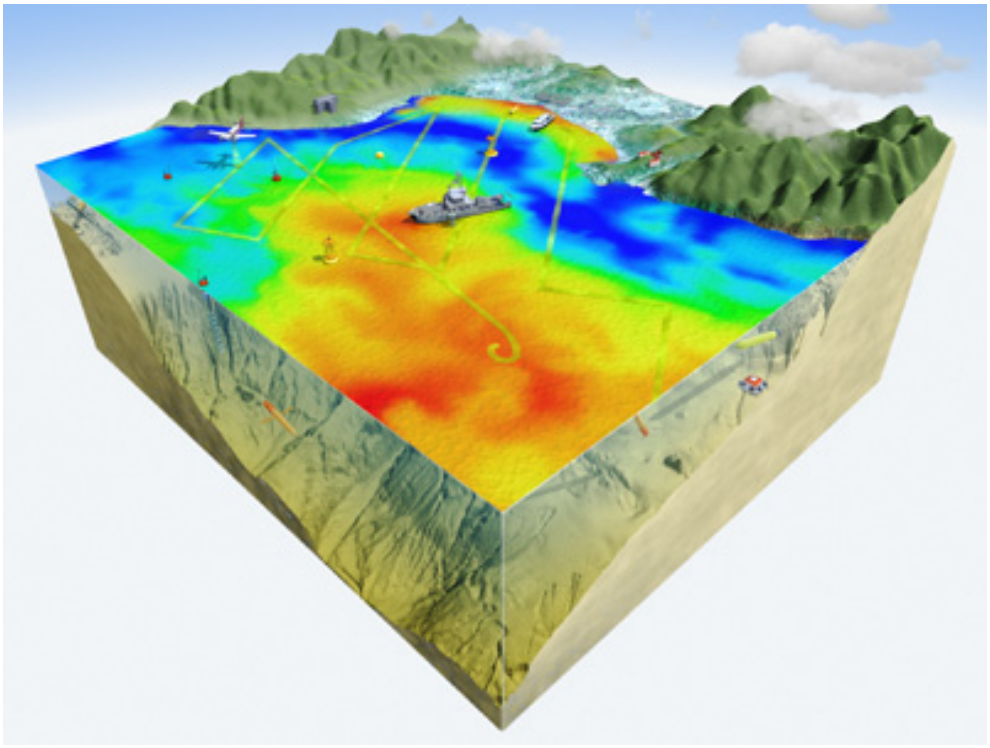

Figure 6.1: The AOSN II field experiment in Monterey Bay involves several ships and dozens of floating, diving, and flying oceanographic instruments operating simultaneously. Their goal is to observe and model water movement, temperature, and other upwelling-related processes in Monterey Bay over a 4-week period during August, 2003. In this image of the Monterey Bay study area, the color of the ocean surface indicates water temperature - cold upwelling water is shown in blue and warmer water in yellow and red. Image credit: David Fierstein © 2003, MBARI [81].

can be made [54] and that the structures of interest are robust to errors in the forecast [47]. Then real-time computations of LCS may improve the forecast of interesting mesoscale features, such as fronts, coherent masses of moving fluid - that might have a different temperature, salinity or fluorescence -, or eddies. This knowledge is essential to obtain an efficient distribution of sensing devices in order to reduce errors in the data assimilation. First efforts in this direction have been made within the AOSN II field experiment [2]. Here LCS were approximated via direct Lyapunov exponents [47, 74] (DLE), however only taking two-dimensional velocity data into account.

In the following sections we want to test the methods developed in the previous

chapters and use them for the analysis of ocean flows. To be more precise, we apply our techniques to time-dependent two-dimensional data sets, obtained within the AOSN II project from high frequency radar measurements in Monterey Bay in summer 2003 [2]. We identify LCS [102] as structures characterized by large direct expansion rates and demonstrate that they correspond to the curves obtained by considering direct Lyapunov exponents. For the integration and interpolation of the two-dimensional time-dependent data we use MANGEN [74, 75], which also takes the different boundary conditions into account. However, in this context very long trajectories need to be considered to obtain a clear picture of the location of the Lagrangian structures of interest. This is computationally very expensive and therefore not applicable for real-time (hours) computations in an experiment. To decrease the computational effort, we propose a different direct expansion rate approach that only considers the box centers. This alternative method is very efficient but nevertheless gives a good indication of the location of areas of high stretching.

Additionally, using the set-up described above, we compute transport rates from near-shore regions to regions in the open sea west of Monterey Bay. The results demonstrate the strong time-dependence of the transport processes, having serious implications for such things as pollution timing as discussed in [74, 75]. We note that, due to the open boundary allowing particles to leave the area under consideration, previous methods that take advantage of volume-preservation are difficult to apply.

Moreover, the first set of experiments indicate that our methods allow the consideration of three-dimensional oceanic flows. Treatment of such data sets will be essential in the future for being able to analyze genuinely three-dimensional events such as coastal upwelling. For our analysis we use velocity data provided by the Harvard Ocean Prediction System (HOPS) [1, 54]. This data set was also collected and assimilated during the AOSN II field experiment.

6.2 Two-Dimensional Ocean Flows

In this section we will analyze a two-dimensional finite-time velocity field representing surface velocity data obtained from high frequency radar measurements in Monterey Bay. The data set represents 1072 time slices of hourly measurements, covering July 23, 2003 to September 5, 2003. The data has been re-analyzed, that is gaps are filled, and has been interpolated into a regular 22×18 grid.

Note that the data is given only with respect to a relatively small region ($[122.334°, -121.821°] \times [36.5659°, 36.9736°]$). To avoid that too many particles will be advected out of the region, we choose with

$$Q = [-122.15, -121.75] \times [36.5, 37]$$

an initial box that is considerably smaller than the underlying grid, see Figure 6.2. We consider a covering on depth 14 consisting of 8404 boxes. Notably, a single box covers an area of approximately 280 m $\times$ 430 m, whereas the size of the outer box Q corresponds to an area of approximately 35.6 km $\times$ 55.5 km.

For direct expansion rate computations we consider ten pairs of Monte Carlo points in each box with initial distance $\varepsilon = 0.0003125$ (20% of box radius), corresponding to approx. 28 m.

The trajectories are computed using MANGEN [74]. It employs a fourth-order Runge-Kutta scheme with adaptive step-size control, bi-cubic interpolation in space and cubic interpolation in time. Moreover, boundary conditions at the shore and at open boundaries are used. The trajectories are computed over $T = 144$ hours choosing a relative tolerance of 10^{-5}. If particles leave the grid, we set their velocity to zero. Note that trajectories that leave the region are typically not part of a coherent structure, see for example [98, 106].

The result for such a computation is given in Figure 6.2 b), where magenta and red structures correspond to objects characterized by high expansion. Observe how nicely the results compare to the results obtained from the LCS computation using the direct Lyapunov exponents given in Figure 6.2 a).

Note that in this chapter we will use a slightly different color scheme to visualize structures of maximum expansion. Boxes with negative or zero expansion rates will be colored blue. Positive expansion rates are indicated by different shades from magenta to red. Light red corresponds to maximum expansion.

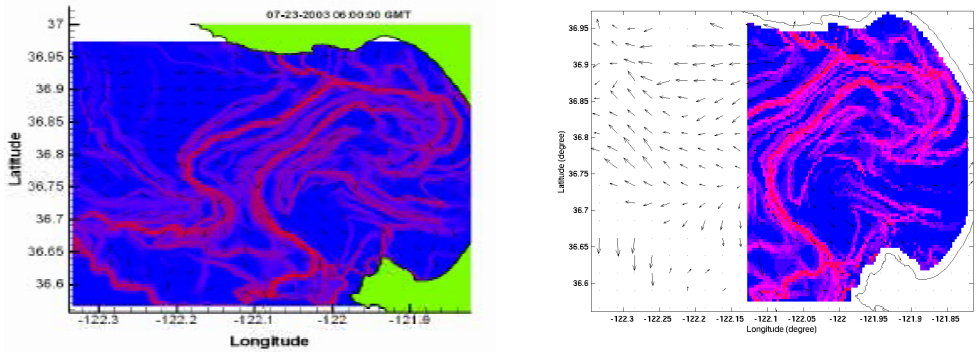

a) b)

Figure 6.2: Comparison of DLE field and the direct expansion rate field using high frequency radar data obtained with the AOSN II field experiment in Monterey Bay in summer 2003 [2]. a) DLE field for July 23, 2003, 6:00, computed over 144 hours [101]; b) direct expansion rate field for the same set-up.

Barriers to Transport Moreover, we demonstrate that the structures detected by our methods are barriers to transport. We release drifting objects on each side of the dominant LCS, see Figure 6.3 a). Their positions after they have been advected by the flow for several hours are shown in Figure 6.3 b)-d). The result demonstrates not only that the Lagrangian coherent structures bound dynamically distinct regions but also that they repel particles.

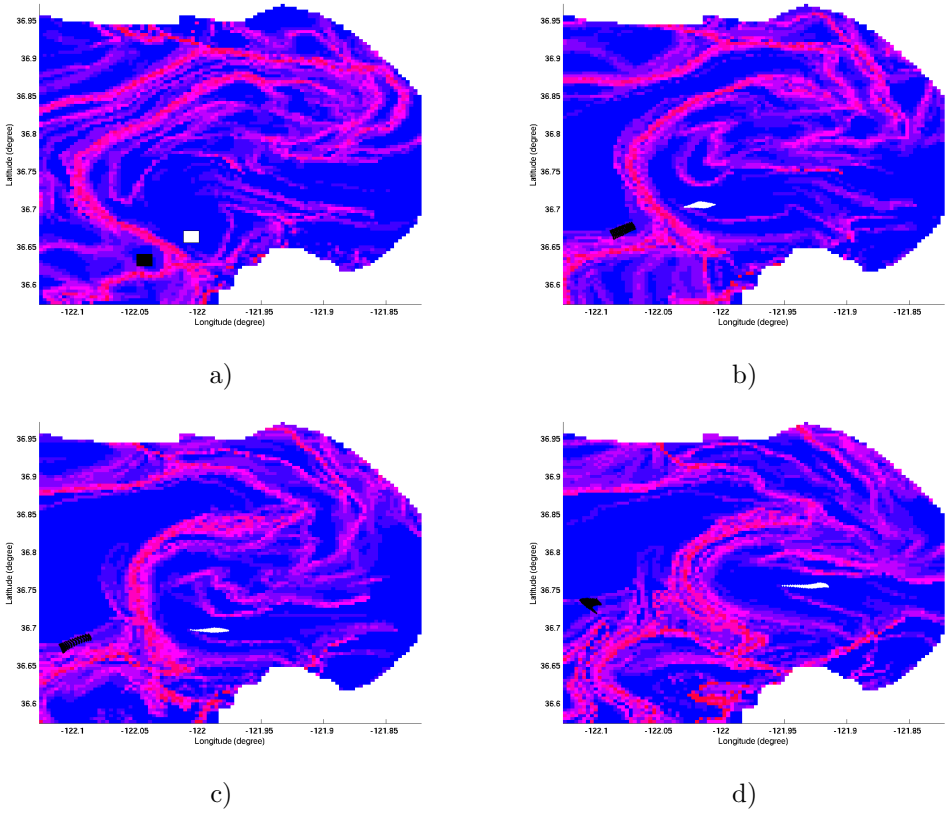

Figure 6.3: Lagrangian coherent structures serve as barriers to transport. Particles are released on each side of the dominant Lagrangian coherent structure and advected. The Lagrangian coherent structures are approximated using direct expansion rates as described in the text. a) Drifting objects are initialized on July 23, 2003, 6:00 GMT. b) Position of the packages and the coherent structures 18 hours later; c) after 30 hours; d) after 42 hours.

Advection of Lagrangian coherent structures Finally, we test how particles initialized on the LCS are advected by the flow. For this we extract the LCS by the subdivision algorithm. We start with a covering on depth 14. The selection

criterion is to keep only those boxes whose direct expansion rate is above average, where the average is taken over all boxes with positive direct expansion rate. We subdivide in both coordinate directions and impose the selection criterion again. Then we integrate the trajectories with respect to the center points of the boxes in the resulting covering. The results are shown in Figure 6.4. Note that for small integration times (e.g. 6 or 18 hours) the advected particles stay very close to the LCS or even on the object. This demonstrates that the structures of interest are at least approximately Lagrangian, that is, they are material lines moving with fluid. This confirms the results in [102]. In an experimental context this also means that the expansion rate field does not need to be computed at every time instance but can be advected using a flow forecast.

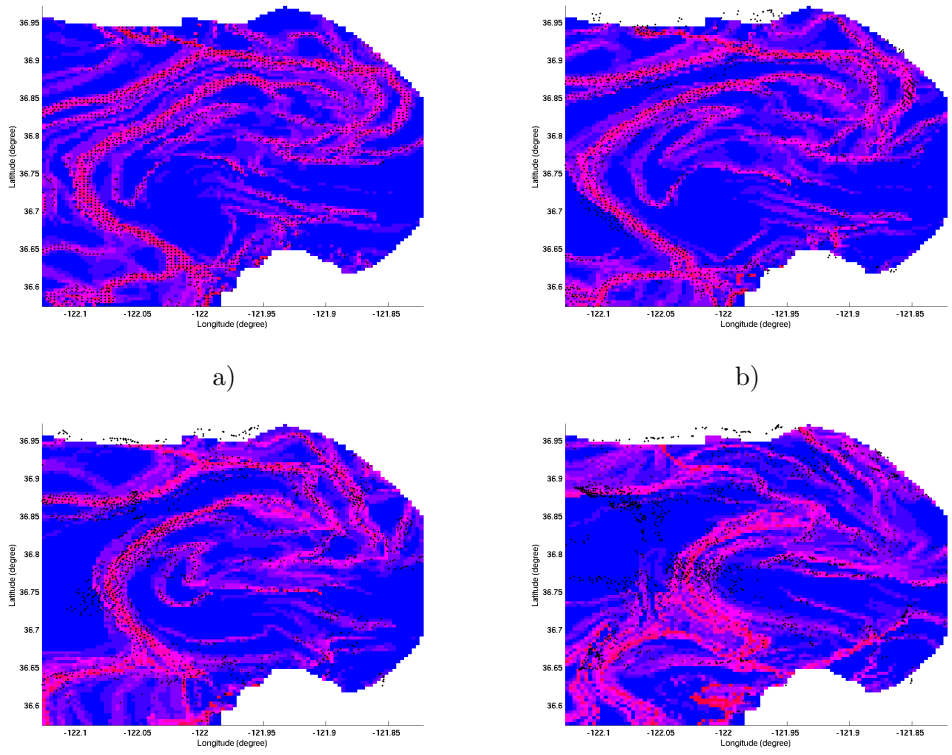

Figure 6.4: Advection of particles initialized on Lagrangian coherent structures. a) LCS are extracted using the subdivision algorithm (7246 boxes). Here the center points of the respective box covering are superimposed on the direct expansion rate field. b) Advection of the center points over 6 hours, c) 18 hours, d) 42 hours. For clarity only a quarter of the points are shown.

Faster algorithm However, we have seen that for the approximation of LCS long trajectories need to be computed and when employing the direct expansion rate approach, this has to be carried out for a large number of initial conditions (test points). Hence an algorithm that can be used within an experimental setting is needed. We therefore propose the following approach. We only consider the center points of a box and compute an approximate direct expansion rate as follows:

$$\delta_{fast}(T;\tau,B_i) := \log\left(\max_j \frac{1}{T}\frac{|\varphi^{T+\tau,\tau}(c_i)-\varphi^{T+\tau,\tau}(n_j(c_i))|}{|n_j(c_i)-c_i|}\right),$$

where c_i denotes the center point of the box B_i and $n_j(c_i)$ the center point of the j-th neighboring box of B_i, see Figure 6.5. Obviously, this idea is in spirit of the relative dispersion methods discussed before.

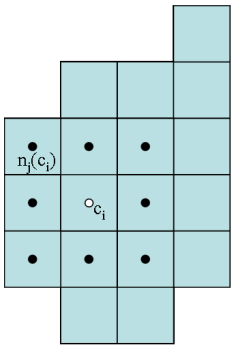

Figure 6.5: Choice of test points for an alternative approach to obtain coarse grained picture of LCS - only the center points of the boxes serve as initial conditions.

We apply this method to our box covering. A comparison between the direct expansion rate field using 10 pairs of Monte Carlo points per box and the fast approach using only the center points is shown in Figure 6.6. Though the fast method provides a coarser picture it gives a good indication of the location of Lagrangian coherent structures, although only as many as 5% of initial conditions are considered compared to the usual direct expansion rate approach. An animation of the evolution of the Lagrangian coherent structures approximated this way can be found at

`http://www-math.upb.de/~padberg/thesis.html`.

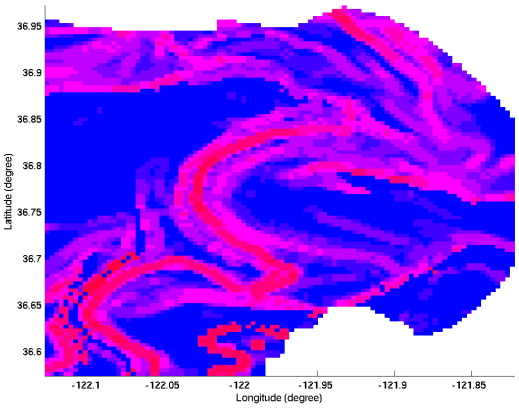

a)

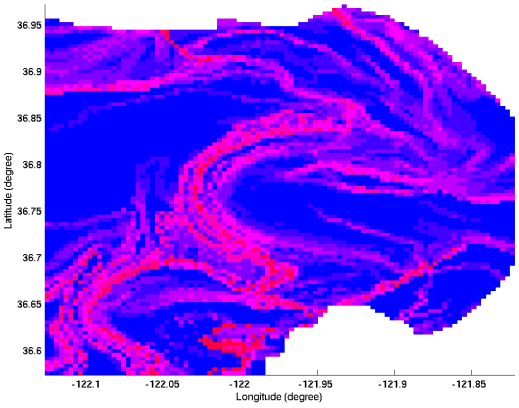

b)

Figure 6.6: Approximation of Lagrangian coherent structures using direct expansion rates. a) '"Fast" method only using the center points; b) standard direct expansion rate approach.

6.3 Transport in Monterey Bay

We now want to quantify transport between near shore regions and the open sea.

To describe the results in the notation introduced in Chapter 5, we consider the non-autonomous mappings

$$f_k = \varphi^{6(k+1),6k},$$

where $\varphi^{t+\tau,\tau}$ is the (numerical) evolution of the flow and $t = 1$ corresponds to one hour. So f_k maps a point to its position six hours in the future. Here $k = 0$

corresponds to the date July 23, 2003, 05:00 GMT. We consider source sets R_i and a target set S, see Figure 6.7 and compute time-dependent transport probabilities between theses sets.

Note that S and R_i are box sets, that means $\underline{S} = \overline{S}$. Moreover, they are chosen time-independently, that is $S(k) = S$ for all k. We are now interested in transport probabilities $p(R_i(k), S(l)) = \frac{T(R_i(k),S(l))}{m(R_i(k))}$ for different k and l. In particular, we want to analyze how different release times affect the transport of particles into the set S.

Based on the box covering described above we compute transition matrices $\tilde{P}_{[k,k+1]}$ using 100 Monte Carlo Points per box. Multiplication yields transition matrices $P_{[k,l]_\mathcal{B}}$ which will be employed for the transport calculations as described in Chapter 5.

The results are shown in Figures 6.7 and 6.8. The different colors of the bars correspond to different release times. The transport probabilities are then given as a function of the time since release, where $n = 1$ corresponds to six hours. So, transport probabilities within a time span of 72 hours are considered. Although the setting is very simple the results nevertheless illustrate the serious time-dependence of the transport mechanism. Note that we do not observe transport between R_3 and S within the time span considered - therefore this result is not shown in Figure 6.8. This is surprising as R_3 is located very close to the target set in phase space. Such observations, however, may have implications, for example, on optimal pollution timing [74, 75].

6.4 Three-Dimensional Ocean Flows

We now want to apply our methods to three-dimensional velocity data, obtained from measurements within the AOSN II project [2]. The data under consideration has been re-analyzed on the basis of the HOPS ocean model [1, 54]. It covers August 2, 2003 to September 6, 2003, given at intervals of three hours (281 time slices) and has been interpolated into a rotated spherical grid with $96 \times 83 \times 22$ elements. The 22 levels correspond to planes between 1 m and 900 m below the water surface. In order to be able to use standard interpolation schemes, we rotate the grid data to a rectangular domain and choose an initial box $Q = [-122, -121.2] \times [36, 36.8] \times [-80, 0]$. We consider a box covering on depth 21 (1230264 boxes). Here the size of a single box corresponds to approximately 560 m $\times$ 690 m $\times$ 60 cm, which means that two different length scales need to be dealt with. For our computation we use a fourth-order Runge-Kutta integration scheme ($h = 1$, corresponding to 3 hours) as well as linear interpolation in space and time.

We compute trajectories for $T = 48$ (i.e. 144 hours). Unfortunately, MAN-

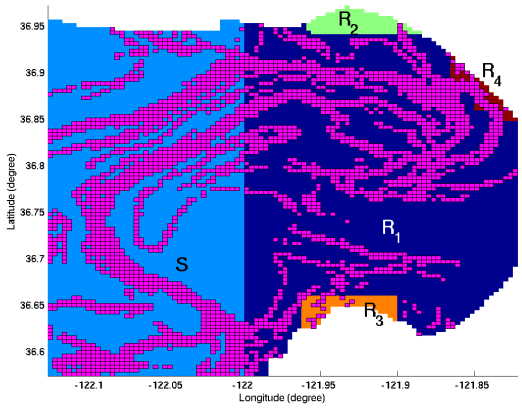

a)

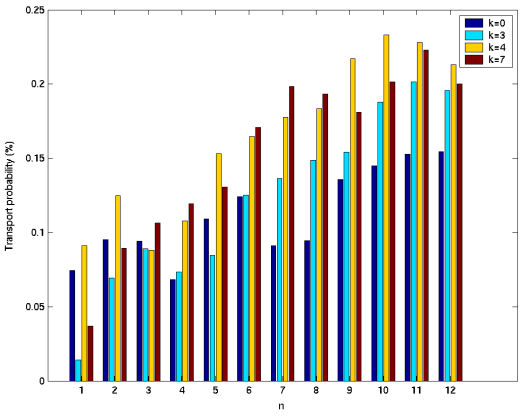

b)

Figure 6.7: a) Sets under consideration for transport rates with boxes of large expansion rates for $k = 0$ superimposed. b) Transport probability $p(R(k), S(l))$, where $R(k) = \cup_{i=1,\ldots,4} R_i(k)$, for different k and l, with $l = k + n$.

GEN does not yet support computations in 3d and therefore trajectories are integrated and interpolated using MATLAB. That also means, that in these first experiments we do not take any boundary conditions into account. However, the data covers a very large region, whereas our box covering is only chosen with respect to a small region. So we expect that particles initialized in the box covering will hardly leave the large region within the time span under consideration.

Results for the direct expansion rate approach, using 20 pairs of Monte Carlo points per box with initial distance $\varepsilon = 0.0015$ (50% box radius), are shown in

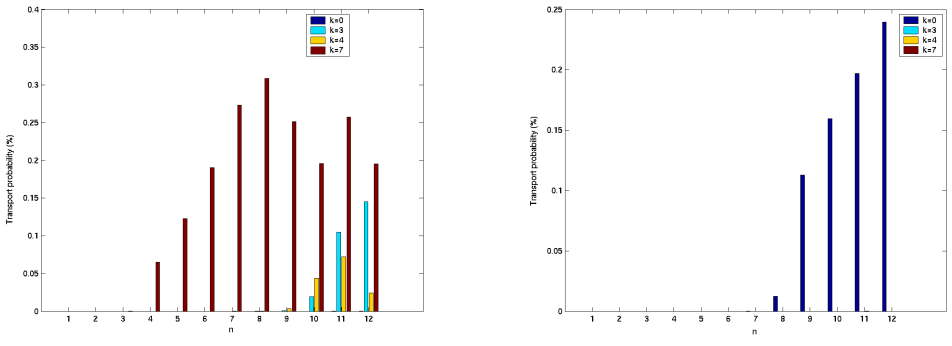

a) b)

Figure 6.8: a) Transport probability $p(R_2(k), S(l))$, for different k and l with $l = k + n$. b) Transport probability $p(R_4(k), S(l))$.

Figure 6.9. We also use the second approach introduced in Section 6.2, where only center points are considered, see Figure 6.10. Note that for the visualization the box covering has been transformed to match the original rotation of the grid.

Both methods give a striking indication of the existence of repelling material surfaces. We note that to the best of our knowledge this has been the first time that these structures have been computed and visualized for three-dimensional ocean flows based on finite-time velocity data. The improvement of these computations using higher order interpolation schemes is subject to future research.

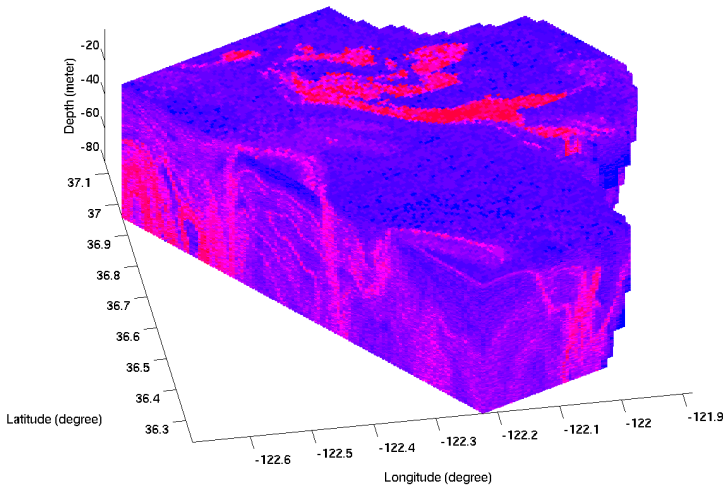

Figure 6.9: Approximation of Lagrangian coherent structures in Monterey Bay using re-analyzed data from a three-dimensional ocean model (HOPS data). Computation of direct expansion rates with respect to 20 pairs of Monte Carlo points per box (1230264 boxes).

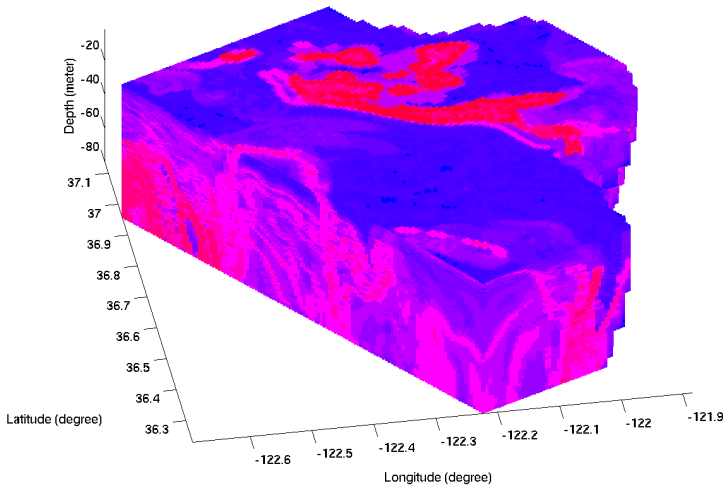

Figure 6.10: Approximation of Lagrangian coherent structures in Monterey Bay. Computation of direct expansion rates considering only the center points (1230264 boxes) as described in Section 6.2.

Chapter 7

Conclusion

Transport processes play an important role in many natural phenomena. Over the past twenty years the analogy between the global, geometrical study of nonlinear dynamical systems and transport and mixing studies in classical and fluid mechanics has been used to obtain a deeper understanding of transport issues in a variety of systems, notably in geophysical models

For the analysis of transport processes two main ingredients need to be considered. First, boundaries between dynamically distinct regions are detected and approximated. In the context of dynamical systems these structures correspond to invariant manifolds of hyperbolic periodic points or, in time-dependent systems, of hyperbolic trajectories. Secondly, transport is quantified in terms of transport rates and probabilities. Here lobe dynamics is often employed to explain the transport mechanism and derive transport rates.

Much effort has been made to extend the above ideas to finite-time velocity fields given by a finite set of data. However, most of the methods to extract finite-time invariant manifolds or Lagrangian coherent structures have been formulated and applied to the two-dimensional context only. Moreover, lobe dynamics is hardly applicable to the analysis of flows with general time dependence. Aperiodicity, however, is characteristic of finite-time velocity fields.

This thesis contributes to the current research on the detection of invariant manifolds in non-autonomous dynamical systems and the approximation of transport rates by making use of the advantages of different techniques. In particular, we have extended the well-established methods related to finite-time Lyapunov exponents and relative dispersion, and have embedded them in the set oriented approach first proposed by Dellnitz and Hohmann [23, 24]. We have demonstrated that this new multilevel technique, the *expansion rate approach*, allows for the efficient detection, approximation, and continuation of stable and unstable manifolds to hyperbolic objects.

In addition, we have presented a set oriented technique for the computation

of transport rates in dynamical systems with general time dependencies which is independent of invariant manifolds. The method relies on a discretization of the Perron-Frobenius operator of the underlying non-autonomous dynamical system and extends and improves the results in Dellnitz, Junge, Koon et al. [28], where the autonomous case has been treated. Hence, this approach can also be applied to dynamical systems where the invariant manifold cannot be obtained accurately enough to consider lobe dynamics or where the underlying transport mechanism remains obscure.

Altogether this thesis makes four major contributions to the current research in the numerical analysis of chaotic transport:

1. Detection and extraction of invariant manifolds in autonomous dynamical systems,

2. Extraction and continuation of invariant manifolds in non-autonomous dynamical systems,

3. Manifold independent approach for the computation of transport rates between regions of interest in non-autonomous dynamical systems, and

4. Application of these methods to geophysical fluid data obtained from high frequency radar measurements in Monterey Bay in summer 2003 [2].

Although the methods developed work successfully in the examples considered within this thesis, there are still a lot of open problems. First of all we have only extracted *candidates* of invariant manifolds, that is, we have only considered necessary but not sufficient conditions. To find sufficient conditions which are applicable to general flows and which can be evaluated with reasonable numerical effort is subject to future research.

Another challenging problem is that the computation of transport rates using transition matrices is computationally demanding. Typically, a discretization of a subset of phase space needs to be considered that has full dimension. Although the use of adaptive methods as proposed in Chapter 5 reduces the number of boxes considerably, the extension to higher dimensional systems (i.e. > 4) remains problematic. Furthermore, when applying the adaptive refinement algorithm for the transport boxes, in every step of the algorithm the transition matrices need to be computed from scratch although only very few boxes have been subdivided. Hence, more efficient methods need to be designed for quantifying transport.

In this thesis we have made efforts to the analysis of finite-time geophysical data sets. In a first set of experiments we have also considered graphs, proposing a first step to the analysis of general time series. However, to deal with an increasing amount of data obtained from measurements, with the structures of

interest typically hidden in a huge multi-dimensional data set with many different scales, is certainly one of the future challenges in scientific computing. How to analyze such time series and extract from them the information relevant for the solution of the problem under consideration is largely open.

Bibliography

[1] AOSN II (Harvard). `http://people.deas.harvard.edu/~leslie/AOSNII/`.

[2] AOSN II (Princeton). `http://www.princeton.edu/~dcsl/aosn/`.

[3] H. Aref. The development of chaotic advection. *Physics of Fluids*, 14(4):1315–1325, 2002.

[4] ASAP. `http://www.princeton.edu/~dcsl/asap/`.

[5] P.J. Aston and M. Dellnitz. The computation of Lyapunov exponents via spatial integration with application to blowout bifurcations. *Computer Methods in Applied Mechanics and Engineering*, 170:223–237, 1999.

[6] P.J. Aston and M. Dellnitz. Computation of the dominant Lyapunov exponent via spatial integration using matrix norms. *Proceedings of the Royal Society A*, 459:2933–2955, 2003.

[7] B. Aulbach, M. Rasmussen, and S. Siegmund. Approximation of attractors of nonautonomous dynamical systems. *Discrete and Continuous Dynamical Systems Series B*, 5(2):215–238, 2005.

[8] B. Aulbach, M. Rasmussen, and S. Siegmund. Invariant manifolds as pullback attractors of nonautonomous differential equations. *Discrete and Continuous Dynamical Systems Series A*, 2005. to appear.

[9] G. Boffetta, A. Celani, M. Cencini, G. Lacorata, and A. Vulpiani. Nonasymptotic properties of transport and mixing. *Chaos*, 10(1):50–60, 2000.

[10] G. Boffetta, G. Lacorata, G. Redaelli, and A. Vulpiani. Detecting barriers to transport: a review of different techniques. *Physica D*, 159:58–70, 2001.

[11] G. Boffetta, G. Lacorata, and A. Vulpiani. Introduction to chaos and diffusion. In G. Boffetta, G. Lacorata, G. Visconti, and A. Vulpiani, editors, *Chaos in geophysical flows*. Otto Editore, 2003.

[12] K.P. Bowman. Manifold geometry and mixing in observed atmospheric flows. Preprint, 1999.

[13] D. Bürkle, M. Dellnitz, O. Junge, M. Rumpf, and M. Spielberg. Visualizing complicated dynamics. In *Proceedings of Visualization '99*, 1999.

[14] F.P. Chavez, R.P. Michisaki, G.E. Friederich, J.T. Pennington, B. Schlining, C. Fayos, P. Walz, C. Sakamoto, R. Hopcroft, R. Kudela, C. Castro, E. Mauri, and K. R. Buck. A ten-year time series from Monterey Bay, California: seasonal, interannual and long-term patterns. `http://www.mbari.org/bog/Projects/CentralCal/intro.htm`.

[15] D.N. Cheban, P.E. Kloeden, and B. Schmalfuß. Pullback attractors under discretization. In *Proceedings of Equadiff '99*, pages 1024–1029. World Scientific, 2000.

[16] W.A. Coppel. *Dichotomies in Stability Theory.* Lecture Notes in Mathematics. Springer-Verlag, New York, NY, 1978.

[17] C. Coulliette and S. Wiggins. Intergyre transport in a wind-driven, quasigeostrophic double gyre: An application of lobe dynamics. *Nonlinear Processes in Geophysics*, 8:69–94, 2001.

[18] P. Cvitanović, R. Artuso, P. Dahlqvist, R. Mainieri, G. Tanner, G. Vattay, N. Whelan, and Andreas Wirzba. *Chaos: Classical and Quantum.* Niels Bohr Institute, Copenhagen, 2003. `www.nbi.dk/ChaosBook`.

[19] F.S. De Blasi and J. Schinas. On the stable manifold theorem for discrete time dependent processes in Banach spaces. *Bull. London Math. Soc.*, 5:275–282, 1973.

[20] C. Dellago and Wm.G. Hoover. Are local Lyapunov exponents continuous in phase space? *Physics Letters A*, 268:330–334, 2000.

[21] M. Dellnitz, G. Froyland, and O. Junge. The algorithms behind GAIO – Set oriented numerical methods for dynamical systems. In *Ergodic Theory, Analysis, and Efficient Simulation of Dynamical Systems*, pages 145–174, 2001.

[22] M. Dellnitz, K.A. Grubits, J.E. Marsden, K. Padberg, and B. Thiere. Set oriented computation of transport rates in 3-degree of freedom systems: the Rydberg atom in crossed fields. *Regular and Chaotic Dynamics*, 10(2):173–192, 2005.

[23] M. Dellnitz and A. Hohmann. The computation of unstable manifolds using subdivision and continuation. In H.W. Broer, S.A. van Gils, I. Hoveijn, and F. Takens, editors, *Nonlinear Dynamical Systems and Chaos*, pages 449–459. Birkhäuser, *PNLDE* 19, 1996.

[24] M. Dellnitz and A. Hohmann. A subdivision algorithm for the computation of unstable manifolds and global attractors. *Numerische Mathematik*, 75:293–317, 1997.

[25] M. Dellnitz and O. Junge. An adaptive subdivision technique for the approximation of attractors and invariant measures. *Computing and Visualization in Science*, 1:63–68, 1998.

[26] M. Dellnitz and O. Junge. On the approximation of complicated dynamical behavior. *SIAM Journal on Numerical Analysis*, 36(2):491–515, 1999.

[27] M. Dellnitz and O. Junge. Set oriented numerical methods for dynamical systems. In B. Fiedler, G. Iooss, and N. Kopell, editors, *Handbook of Dynamical Systems II: Towards Applications*, pages 221–264. World Scientific, 2002.

[28] M. Dellnitz, O. Junge, W.S. Koon, F. Lekien, M.W. Lo, J.E. Marsden, K. Padberg, R. Preis, S.D. Ross, and B. Thiere. Transport in dynamical astronomy and multibody problems. *International Journal of Bifurcation and Chaos*, 15(3):699–727, 2005.

[29] M. Dellnitz, O. Junge, M.W. Lo, J.E. Marsden, K. Padberg, R. Preis, S.D. Ross, and B. Thiere. Transport of Mars-crossing asteroids from the quasi-Hilda region. *Physical Review Letters*, 94(23):231103, 2005.

[30] M. Dellnitz, K. Padberg, and R. Preis. Integrating multilevel graph partitioning with hierarchical set oriented methods for the analysis of dynamical systems. Technical report, Preprint 152, DFG Priority Program: Analysis, Modeling and Simulation of Multiscale Problems, 2004.

[31] M. Dellnitz and R. Preis. Congestion and almost invariant sets in dynamical systems. In F. Winkler, editor, *Symbolic and Numerical Scientific Computation (Proceedings of SNSC'01)*, LNCS 2630, pages 183–209. Springer, 2003.

[32] P. Deuflhard, M. Dellnitz, O. Junge, and Ch. Schütte. Computation of essential molecular dynamics by subdivision techniques I: Basic concept. In *Computational Molecular Dynamics: Challenges, Methods, Ideas*, LNCSE 4, pages 98–115. Springer, 1998.

[33] L. Dieci, R.D. Russell, and E.S. van Vleck. On the computation of Lyapunov exponents for continuous dynamical systems. *SIAM J. Numer. Anal.*, 34(1):402–423, 1997.

[34] L. Dieci and E.S. van Vleck. Lyapunov spectral intervals: Theory and computations. *SIAM J. Numer. Anal.*, 40(2):516–542, 2002.

[35] R. Doerner, B. Hübinger, W. Martienssen, S. Grossmann, and S. Thomae. Stable manifolds and predictability of dynamical systems. *Chaos, Solitons & Fractals*, 10(11):1759–1782, 1999.

[36] T. Dombre, U. Frisch, J.M. Greene, M. Hénon, A. Mehr, and A.M. Soward. Chaotic streamlines in the ABC flows. *J. Fluid Mech.*, 167:353–391, 1986.

[37] G. Froyland. Statistically optimal almost-invariant sets. *Physica D*, 200:205–219, 2005.

[38] G. Froyland and M. Dellnitz. Detecting and locating near-optimal almost-invariant sets and cycles. *SIAM Journal on Scientific Computing*, 24(6):1839–1863, 2003.

[39] F. Gabern, W.S. Koon, J.E. Marsden, and S.D. Ross. Theory and computation of non-RRKM lifetime distributions and rates in chemical systems with three or more degrees of freedom. Submitted to *Physica D*, 2005.

[40] F. Gabern and S.D. Ross, 2004. personal communication.

[41] B.J. Gladman, J.A. Burns, M. Duncan, P. Lee, and H.F. Levinson. The exchange of impact ejecta between terrestial planets. *Science*, 271:1387–1392, 1996.

[42] G. Gómez, W.S. Koon, M.W. Lo, J.E. Marsden, J. Masdemont, and S.D. Ross. Invariant manifolds, the spatial three-body problem and space mission design. *Advances in the Astronautical Sciences*, 109(1):3–22, 2001.

[43] J. Guckenheimer and P. Holmes. *Nonlinear Oscillations, Dynamical Systems, and Bifurcations of Vector Fields*. Number 42 in Applied Mathematical Sciences. Springer-Verlag, New York, NY, 1983.

[44] W. Hahn. *Stability of Motion*. Grundlehren der mathematischen Wissenschaften in Einzeldarstellungen. Springer-Verlag, New York, NY, 1967.

[45] G. Haller. Finding finite-time invariant manifolds in two-dimensional velocity fields. *Chaos*, 10(1):99–108, 2000.

[46] G. Haller. Distinguished material surfaces and coherent structures in three-dimensional fluid flows. *Physica D*, 149:248–277, 2001.

[47] G. Haller. Lagrangian coherent structures from approximate velocity data. *Physics of Fluids*, 14, 2002.

[48] G. Haller. An objective definition of a vortex. *Journal of Fluid Mechanics*, 525:1–26, 2005.

[49] G. Haller and A.C. Poje. Finite time transport in aperiodic flows. *Physica D*, 119:352–380, 1998.

[50] G. Haller and G. Yuan. Lagrangian coherent structures and mixing in two-dimensional turbulence. *Physica D*, 147:352–370, 2000.

[51] M. Hénon. A two dimensional map with a strange attractor. *Commun. Math. Phys.*, 50, 1976.

[52] M. Hessel. Partool. Script for Parallel Computing, 2002.

[53] H. Heuser. *Lehrbuch der Analysis - Teil 2.* Teubner, Stuttgart, 1995.

[54] HOPS. `http://oceans.deas.harvard.edu/HOPS/HOPS.html`.

[55] F. Hunt. A Monte Carlo approach to the approximation of invariant measures. *Random Comput. Dynam.*, 2:111–133, 1994.

[56] K. Ide, D. Small, and S. Wiggins. Distinguished hyperbolic trajectories in time-dependent fluid flows: analytical and computational approach for velocity fields defined as data sets. *Nonlinear Processes in Geophysics*, 9:237–263, 2002.

[57] T. Inanc, S.C. Shadden, and J.E. Marsden. Optimal trajectory generation in ocean flows. Accepted for the Proceedings of the American Control Conference, Oregon, Portland, June 2005.

[58] M.C. Irwin. Hyperbolic time-dependent processes. *Bull. London Math. Soc.*, 5:209–217, 1973.

[59] C. Jaffé, D. Farrelly, and T. Uzer. Transition states in atomic physics. *Physical Review A*, 60:3833–3850, 1999.

[60] C.K.R.T. Jones. A dynamics group look at the ocean. *SIAM News*, 33(2):1, 2000.

[61] C.K.R.T. Jones and S. Winkler. Invariant manifolds and Lagrangian dynamics in the ocean and atmosphere. In B. Fiedler, G. Iooss, and N. Kopell, editors, *Handbook of Dynamical Systems II: Towards Applications*, pages 55–92. World Scientific, 2002.

[62] B. Joseph and B. Legras. Relation between kinematic boundaries, stirring, and barriers for the antarctic polar vortex. *Journal of the Atmospheric Sciences*, 59:1198–1212, 2002.

[63] N. Ju, D. Small, and S. Wiggins. Existence and computation of hyperbolic trajectories of aperiodically time dependent vector fields and their approximations. *International Journal of Bifurcation and Chaos*, 13(6):1449–1457, 2003.

[64] O. Junge. *Mengenorientierte Methoden zur numerischen Analyse dynamischer Systeme.* PhD thesis, Universität Paderborn, 1999.

[65] O. Junge. An adaptive subdivision technique for the approximation of attractors and invariant measures: Proof of convergence. *Dynamical Systems*, 16(3):213–222, 2001.

[66] A. Katok and B. Hasselblatt. *Introduction to the Modern Theory of Dynamical Systems.* Cambridge University Press, New York, NY, 1995.

[67] H. Keller and G. Ochs. Numerical approximation of random attractors. In H. Crauel and M. Gundlach, editors, *Stochastic Dynamics*, pages 93–115. Springer-Verlag, New York, 1999.

[68] P.E. Kloeden, H. Keller, and B. Schmalfuß. Towards a theory of random numerical dynamics. In H. Crauel and M. Gundlach, editors, *Stochastic Dynamics*, pages 259–282. Springer-Verlag, New York, 1999.

[69] P.E. Kloeden and B. Schmalfuß. Nonautonomous systems, cocycle attractors and variable time-step discretization. *Numerical Algorithms*, 14:141–152, 1997.

[70] T.-Y. Koh and B. Legras. Hyperbolic lines and the stratospheric polar vortex. *Chaos*, 12(2):382–394, 2002.

[71] W.S. Koon, M.W. Lo, J.E. Marsden, and S.D. Ross. Heteroclinic connections between periodic orbits and resonance transitions in celestial mechanics. *Chaos*, 10(2):427–469, 2000.

[72] G. Lapeyre. Characterization of finite-time Lyapunov exponents and vectors in two-dimensional turbulence. *Chaos*, 12(3):688–698, 2002.

[73] G. Lapeyre, B.L. Hua, and B. Legras. Comment on "finding finite-time invariant manifolds in two-dimensional velocity fields" [Chaos 10, 99 (2000)]. *Chaos*, 11(2):427–430, 2001.

[74] F. Lekien. *Time-dependent dynamical systems and geophysical flows*. PhD thesis, California Institute of Technology, 2003.

[75] F. Lekien, C. Coulliette, and J.E. Marsden. Lagrangian structures in very high-frequency radar data and optimal pollution timing. In *7th Experimental Chaos Conference - AIP Conference Proceedings Nr.676*, pages 162–168, 2003.

[76] R.S. MacKay, J.D. Meiss, and I.C. Percival. Transport in Hamiltonian systems. *Physica*, 13D:55–81, 1984.

[77] N. Malhotra, I. Mezić, and S. Wiggins. Patchiness: a new diagnostic tool for Lagrangian trajectory analysis in time-dependent fluid flows. *International Journal of Bifurcation and Chaos*, 8(6):1053–1093, 1998.

[78] N. Malhotra and S. Wiggins. Geometric structures, lobe dynamics, and Lagrangian transport in flows with aperiodic time-dependence, with applications to Rossby wave flow. *Nonlinear Science*, 8:401–456, 1998.

[79] A.M. Mancho, D. Small, and S. Wiggins. Computation of hyperbolic trajectories and their stable and unstable manifolds for oceanographic flows represented as data sets. *Nonlinear Processes in Geophysics*, 11:17–33, 2004.

[80] A.M. Mancho, D. Small, S. Wiggins, and K. Ide. Computation of stable and unstable manifolds of hyperbolic trajectories in two-dimensional, aperiodically time-dependent vector fields. *Physica D*, 182:188–222, 2003.

[81] MBARI - Monterey Bay Aquarium Research Institute. `http://www.mbari.org/`.

[82] I. Mezić and A. Banaszuk. Comparison of systems with complex behavior. To appear, 2005.

[83] I. Mezić and S. Wiggins. A method for visualization of invariant sets of dynamical systems based on the ergodic partition. *Chaos*, 9(1):213–218, 1999.

[84] P.D. Miller, C.K.R.T. Jones, A.M. Rogerson, and L.J. Pratt. Quantifying transport in numerically generated velocity fields. *Physica D*, 110:105–122, 1997.

[85] V.I. Oseledec. A multiplicative ergodic theorem: Ljapunov characteristic numbers for dynamical systems. *Transactions of the Moscow Mathematical Society*, 19:197–231, 1968.

[86] J.M. Ottino. *The kinematics of mixing: stretching, chaos and transport*. Cambridge University Press, Cambridge, 1989.

[87] A.C. Poje and G. Haller. Geometry of cross-stream mixing in a double gyre ocean model. *Journal of Physical Oceanography*, 29(8):1649–1665, 1999.

[88] R. Preis. *The PARTY Graphpartitioning-Library, User Manual - Version 1.9 9*. Universität Paderborn, 1998.

[89] R. Preis. *Analyses and Design of Efficient Graph Partitioning Methods*. Heinz Nixdorf Institut Verlagsschriftenreihe, 2000. PhD thesis, Universität Paderborn.

[90] R. Preis. *GADS - Graph Algorithms for Dynamical Systems; User Manual*. Universität Paderborn, 2005. In preparation.

[91] V. Rom-Kedar and S. Wiggins. Transport in two-dimensional maps. *Archive for Rational Mechanics and Analysis*, 109:239–298, 1990.

[92] S.D. Ross. *Cylindrical Manifolds and Tube Dynamics in the Restricted Three-Body Problem*. PhD thesis, California Institute of Technology, 2004.

[93] D. Ruelle. Sensitive dependence on initial condition and turbulent behavior of dynamical systems. In O. Gurel and O.E. Rössler, editors, *Bifurcation Theory and Applications in Scientific Disciplines*, pages 408–416. New York Academy of Sciences, New York, 1979.

[94] D. Ruelle. *Elements of Differentiable Dynamics and Bifurcation Theory*. Academic Press, 1989.

[95] R.J. Sacker and G.R. Sell. A spectral theory for linear differential systems. *J. Differential Equations*, 7:320–358, 1978.

[96] B. Sandstede, S. Balasuriya, C.K.R.T. Jones, and P. Miller. Melnikov theory for finite time vector fields. *Nonlinearity*, 13:1357–1377, 2000.

[97] B. Schmalfuß. Attractors for the non-autonomous dynamical systems. In *Proceedings of Equadiff '99*, pages 684–689. World Scientific, 2000.

[98] J. Schneider and T. Tél. Extracting flow structures from tracer data. *Ocean Dynamics*, 53:64–72, 2003.

[99] O. Schütze. *Set Oriented Methods for Global Optimization*. PhD thesis, Universität Paderborn, 2004.

[100] R. Seydel. *Practical Bifurcation and Stability Analysis: From Equilibrium to Chaos*. Interdisciplinary Applied Mathematics. Springer-Verlag, New York, NY, 1994.

[101] S. Shadden. DLE field for CODAR data (AOSN II, 2003), 2004. Obtained from `http://gyre.cds.caltech.edu/AOSN/public/`.

[102] S.C. Shadden, F. Lekien, and J.E. Marsden. Definition and properties of Lagrangian coherent structures: Mixing and transport in two-dimensional aperiodic flows. *submitted to Physica D*, 2005.

[103] M. Shub. *Global Stability of Dynamical Systems*. Springer, 1987.

[104] S. Siegmund. Computation of nonautonomous invariant manifolds. In B. Aulbach, S. Elaydi, and G. Ladas, editors, *Proc. of ICDEA2001*. Taylor & Francis, 2003.

[105] M. Toner and A.C. Poje. Lagrangian velocity statistics of directed launch strategies in a Gulf of Mexico model. *Nonlinear Processes in Geophysics*, 11:35–46, 2004.

[106] I. Triandaf, E.M. Bollt, and I.B. Schwartz. Approximating stable and unstable manifolds in experiments. *Physical Review E*, 67:037201, 2003.

[107] S.M. Ulam. *A collection of mathematical problems*. Interscience Publishers, 1960.

[108] J. von Hardenberg, K. Fraedrich, F. Lunkeit, and A. Provenzale. Transient chaotic mixing during a baroclinic life cycle. *Chaos*, 10(1):122–134, 2000.

[109] G.A. Voth, G. Haller, and J.P. Gollub. Experimental measurements of stretching fields in fluid mixing. *Physical Review Letters*, 88(25):254501, 2003.

[110] S. Wiggins. *Chaotic Transport in Dynamical Systems*. Springer-Verlag, New York, NY, 1992.

[111] S. Wiggins. *Introduction to Applied Nonlinear Dynamical Systems and Chaos (Second Edition)*. Number 2 in Texts in Applied Mathematics. Springer-Verlag, New York, NY, 2003.

[112] S. Wiggins. The dynamical systems approach to Lagrangian tranport in oceanic flows. *Annu. Rev. Fluid Mech.*, 37:295–328, 2005.

[113] S. Winkler. *Lagrangian dynamics in geophysical fluid flows.* PhD thesis, Brown University, 2001.

[114] Z. You, E.J. Kostelich, and J.A. Yorke. Calculating stable and unstable manifolds. *International Journal of Bifurcation and Chaos*, 1(3):605–623, 1991.

List of Figures

1.1 Illustration of the discrete velocity field measured in Monterey Bay in summer 2003 within the AOSN II project [2]. Also shown is an approximation of Lagrangian coherent structures (red), which mediate transport and mixing (see Chapter 6). 3

1.2 Stable and unstable manifold of a hyperbolic saddle point in a time-discrete dynamical system. Points initialized on either sides of the stable manifold move along different branches of the unstable manifold under the dynamics. 5

2.1 A disk transversely intersecting the stable manifold converges to the unstable manifold. 15

2.2 Duffing oscillator for $\gamma = 0$. a) $\delta = 0.25$: Saddle at the origin and two sinks at $(\pm 1, 0)$. The unstable manifold of the saddle spirals into the sinks, the stable manifold forms a separatrix between the two basins of attraction of the sinks. b) $\delta = 0$: Saddle at the origin and two centers at $(\pm 1, 0)$. Stable and unstable manifolds of the saddle form two homoclinic orbits. 21

2.3 The extended phase space of a non-autonomous system is foliated by time slices or fibers. 24

3.1 Hierarchical storage of the box collections in the software package GAIO. Illustration taken from [27]. 32

3.2 Nested sequence of coverings of the Hénon attractor, obtained after 2, 6, 10, and 12 steps in the subdivision algorithm. 33

3.3 Coverings of the unstable manifold of the saddle point at $(0.6314, 0.1894)$ for the Hénon map. Shown are the initial box containing the fixed point (black) and box collections obtained after 4, 8, and 13 steps in the continuation algorithm. 35

4.1 In many cases the stable manifold of a hyperbolic fixed point serves as a boundary between dynamically distinct regions or even separates different basins of attraction. Hence two points straddling the manifold have a completely different fate, which causes a large direct expansion rate. 45

4.2 Choice of test points in a box and computation of the relative dispersion of a pair of test points. 49
4.3 Direct expansion rate (left column) and expansion rate fields (right column) for the Duffing system for different numbers of iterations of the time-1 map. 51
4.4 Absolute difference between direct expansion rate and expansion rate fields. 52
4.5 Invariant manifolds for the Duffing oscillator, approximated using the continuation algorithm. a) Unstable manifold of the hyperbolic fixed point $\bar{x}$, forming the Duffing attractor; b) part of the stable manifold of $\bar{x}$. 54
4.6 Direct expansion rate fields for the Duffing oscillator for different numbers of iterations N of the time-2π map. 55
4.7 Average direct expansion rates for the Duffing oscillator. 56
4.8 Direct expansion rates for the Duffing oscillator, $N = 5$ for finer partitions. a) Box covering on depth 14 (16384 boxes); b) box covering on depth 16 (65536 boxes). 56
4.9 Direct expansion rates ($N = 2$) for the Duffing oscillator in forward and backward time uncovering parts of the stable manifold (green) and the unstable manifold (red) forming the Duffing attractor. 57
4.10 Expansion rates for a covering of part of the basin of attraction of the Hénon attractor (black); a) $N = 12$; b) $N = 16$. 58
4.11 Expansion rates for $N = 20$ for a covering of a neighborhood of the saddle point (black dot) in the Hénon Map (depth 14, 25 grid points per box). Clearly visible is the stable manifold of the saddle as a maximizer of the expansion rate. The expansion rate values for the corresponding boxes are in good agreement with the dominant Lyapunov exponent of the unstable fixed point. 59
4.12 Expansion rates field with respect to a box covering on depth 14 (16384 boxes). In each box 100 grid points are chosen and $N = 10$ iterates of the time-1 map are computed. 62
4.13 Box coverings of λ-expansive sets for the pendulum for different choices of λ. The heteroclinic connection between the two saddles at $(\pm\pi, 0)$ is shown in black. The center points of the covering of $A_{0.7} \cap Q$ after ten subdivision steps are shown in magenta. 63
4.14 Subdivision algorithm. a) Nested coverings of $A_{0.5} \cap Q$ after one to six subdivision steps. b) Same for Black-Box Selection. 64
4.15 a) Nested coverings of $A_{(0.5,5)} \cap Q$ after one to six subdivision steps. b) Box covering of $A_{(0.3,10)} \cap Q$ after ten subdivision steps. 64
4.16 Direct expansion rates for the ABC-flow. The stable manifolds of periodic orbits are characterized by large values (red). Also elliptic regions are clearly visible (dark blue). a) $N = 1$; b) $N = 3$; c) $N = 5$; d) $N = 10$ ($y - z$ plane). 66

4.17 Regions in the ABC flow with high expansion, corresponding to hyperbolic material surfaces. 67
4.18 Approximation of hyperbolic (blue) and elliptic regions (green) in the ABC flow. 67
4.19 Graph based expansion for the Duffing oscillator with respect to a box covering on depth 14 (16384 boxes). The results for different measures for $d = 1$ and $d = 3$ are shown. 71
4.20 A Poincaré section of the flow in the restricted three-body problem. (Graphics taken from [28]). a) The location of the Poincaré surface-of-section (s-o-s). b) The mixed phase space structure of the PCRTBP is shown on this s-o-s. c) The red and yellow areas are an almost invariant decomposition into two sets. The border between the two sets roughly matches the boundary formed by the branches of the stable and unstable manifolds of the fixed point $(-2.029579567343744, 0)$ drawn as a line. . 74
4.21 Transport of asteroids. Analysis of the graph based expansion, where different measures for $d = 3$ for the directed (left column) and undirected graph (right) are used. Parts of the stable and unstable manifold of a hyperbolic fixed point are superimposed (black). 75

5.1 Direct expansion rates for the aperiodically forced Duffing oscillator with respect to different τ-fibers, choosing $T = 10$. For the computation 20 pairs of Monte Carlo points per box of initial distance $\varepsilon \approx 0.00156$ are used (16384 boxes). 86
5.2 Continuation algorithm for the exponentially forced Duffing oscillator. a) Covering of $A_{(0.5,5)}(0)$ using the subdivision algorithm. b) Continuation step: box covering is mapped to past slice at $\tau = -4$. c) Box covering of $A_{(0.5,5)}(-4)$ after selection steps. d) Covering of $A_{(0.5,5)}(-4)$ using the subdivision algorithm. 88
5.3 Double gyre flow for $A = 1$,$\epsilon = 0.25$, $\omega = 2\pi$. a) Velocity field at $t = 0$; b) velocity field at $t = 0.25$. 89
5.4 Direct expansion rates for the double gyre flow for $\epsilon = 0.25$, $\omega = 2\pi$ and $A = 1$ with respect to different τ-fibers and $T > 0$. For the computation 20 pairs of Monte Carlo points per box of initial distance $\varepsilon \approx 0.0008$ are used (16384 boxes). a) $\tau = 0$, $T = 2$; b) $\tau = 0$, $T = 3$; c) $\tau = 0.3$, $T = 2$; d) $\tau = 0.7$, $T = 2$ 90
5.5 Stable (green) and unstable manifolds (red) in the double gyre flow for $\epsilon = 0.25$, $\omega = 2\pi$ and $A = 1$. Direct expansion rates for a box covering on depth 16 (65536 boxes), using 20 pairs of Monte Carlo points per box of initial distance $\varepsilon \approx 0.0004$. The direct expansion rates are computed for $\tau = 0$, $T = 2$ and $T = -2$. 91
5.6 The sets $\underline{R}$and $\overline{R}$ of a region R. The volume of the boundary boxes is one major contributor to the error in computing transport rates. 95

5.7 Crossings of stable (green) and unstable manifold (red) in the Rossby Wave Flow. Direct expansion rates (20 pairs of points) for $\tau = 0$ and $T = 30$ and $T = -30$, respectively. Note in particular the deformation of the unstable manifold as time increases. 101

5.8 Box partition of phase space for the transport problem in the Rossby wave flow on depth 14 (16384 boxes). 102

5.9 Upper and lower bound on transport rates for different final times l. a) Naive approach. b) Estimates computed using the transition matrix $P_{[0,l]_{\mathcal{B}}}$ as well as $\tilde{P}_{[0,l]}$. 103

5.10 a) Adaptive partition of phase space for the transport problem on depth 10/14, choosing $J = 4$ in the adaptive Algorithm 5.3.6 (6206 boxes). b) Transport probabilities with respect to a box covering on depth 10/14 and for different choices of J in Algorithm 5.3.6. For comparison also the results for the original covering on depth 14 (see Figure 5.8) are shown. 104

5.11 The planar Rydberg problem. Sketch of the position space at an energy level allowing ionization. 105

5.12 Adaptive box covering of Poincaré surface in the interior region (see Figure 5.11) using Algorithm 5.3.6 with $J = 10$. Also shown are the first intersections of the stable and unstable tubes with the Poincaré section. 106

5.13 Scattering probabilities for different levels of refinement of the transport boxes. J is the number of steps in the adaptive Algorithm 5.3.6. 107

6.1 The AOSN II field experiment in Monterey Bay involves several ships and dozens of floating, diving, and flying oceanographic instruments operating simultaneously. Their goal is to observe and model water movement, temperature, and other upwelling-related processes in Monterey Bay over a 4-week period during August, 2003. In this image of the Monterey Bay study area, the color of the ocean surface indicates water temperature - cold upwelling water is shown in blue and warmer water in yellow and red. Image credit: David Fierstein © 2003, MBARI [81]. 109

6.2 Comparison of DLE field and the direct expansion rate field using high frequency radar data obtained with the AOSN II field experiment in Monterey Bay in summer 2003 [2]. a) DLE field for July 23, 2003, 6:00, computed over 144 hours [101]; b) direct expansion rate field for the same set-up. 111

6.3 Lagrangian coherent structures serve as barriers to transport. Particles are released on each side of the dominant Lagrangian coherent structure and advected. The Lagrangian coherent structures are approximated using direct expansion rates as described in the text. a) Drifting objects are initialized on July 23, 2003, 6:00 GMT. b) Position of the packages and the coherent structures 18 hours later; c) after 30 hours; d) after 42 hours. 112

6.4 Advection of particles initialized on Lagrangian coherent structures. a) LCS are extracted using the subdivision algorithm (7246 boxes). Here the center points of the respective box covering are superimposed on the direct expansion rate field. b) Advection of the center points over 6 hours, c) 18 hours, d) 42 hours. For clarity only a quarter of the points are shown. 113
6.5 Choice of test points for an alternative approach to obtain coarse grained picture of LCS - only the center points of the boxes serve as initial conditions. 114
6.6 Approximation of Lagrangian coherent structures using direct expansion rates. a) '"Fast" method only using the center points; b) standard direct expansion rate approach. 115
6.7 a) Sets under consideration for transport rates with boxes of large expansion rates for $k = 0$ superimposed. b) Transport probability $p(R(k), S(l))$, where $R(k) = \cup_{i=1,\ldots,4} R_i(k)$, for different k and l, with $l = k + n$. 117
6.8 a) Transport probability $p(R_2(k), S(l))$, for different k and l with $l = k + n$. b) Transport probability $p(R_4(k), S(l))$. 118
6.9 Approximation of Lagrangian coherent structures in Monterey Bay using re-analyzed data from a three-dimensional ocean model (HOPS data). Computation of direct expansion rates with respect to 20 pairs of Monte Carlo points per box (1230264 boxes). 119
6.10 Approximation of Lagrangian coherent structures in Monterey Bay. Computation of direct expansion rates considering only the center points (1230264 boxes) as described in Section 6.2. 119